Coronary atherosclerosis
and wall shear stress
- Towards application of CT angiography -

Alina Gerarda van der Giessen

Coronary atherosclerosis and wall shear stress
- Towards application of CT angiography -

Coronaire aderverkalking en wandschuifspanning
- De (on)mogelijkheden van CT angiografie -

Proefschrift

ter verkrijging van de graad van doctor aan de
Erasmus Universiteit Rotterdam
op gezag van de
Rector Magnificus

Prof. dr. H.G. Schmidt

en volgens besluit van het College voor Promoties.

De openbare verdediging zal plaatsvinden op
vrijdag 25 juni 2010 om 9.30 uur door

Alina Gerarda van der Giessen
geboren te Tiel

ERASMUS UNIVERSITEIT ROTTERDAM

Promotiecommissie

Promotoren: Prof. dr. ir. A.F.W. van der Steen
                     Prof. dr. P.J. de Feyter

Copromotor: Dr. ir. F.J.H. Gijsen

Overige leden: Prof. dr. ir. F.N. van de Vosse
                     Prof. dr. W.J. Niessen
                     Prof. dr. J.W. Jukema

The greatest thing
you'll ever learn
is just to love
and be loved
in return

Nature Boy by eden ahbew, 1947

Samenvatting

De kransslagaderen, ook wel de coronairen genoemd, voorzien het hart van zu-
urstof en voedingsstoffen zodat het hart kan samentrekken. Aderverkalking, oftewel
atherosclerose, is een inflammatoire ziekte van de vaatwand waarbij vetachtige
stoffen zich ophopen in de wand. De wand zal verdikken en in een gevorderd sta-
dium van de aderverkalking het vat afsluiten hetzij doordat de wand niet verder
kan remodelleren of doordat de plaque ruptureert en de vetachtige stoffen in de
bloedbaan terechtkomen waardoor bloedstolsels ontstaan. Wanneer deze situatie
te lang duurt, krijgt het achterliggende hartweefsel een tekort aan zuurstof en kan
afsterven met een hartaanval als gevolg. Dit coronair vaatlijden is nog steeds één
van de primaire doodsoorzaken in de westerse wereld.

Atherosclerotische plaques hebben de voorkeur zich te vormen in de binnenbocht
van gekromde vaten en nabij vertakkingen. Wandschuifspanning (WSS), een kleine
kracht op de vaatwand als gevolg van de stroming van het bloed, is een lokaliserende
factor. Lage WSS stimuleert atherogene processen in de vaatwand, terwijl hoge WSS
juist een beschermende werking heeft. Ook wordt vermoed dat WSS een rol speelt
in de progressie en ruptuur van plaques middels de vermeende invloed van WSS
op de samenstelling van de plaque. WSS is dus een belangrijke parameter om te
bestuderen in relatie tot de atherosclerose, maar bijzonder lastig te meten in de
coronairen. Daarom wordt vaak gebruikt gemaakt de eindige elementen methode
waarbij de bloedstroom door de coronairen gesimuleerd wordt en de WSS berekend
kan worden. Voor deze berekeningen is een drie dimensionale (3D) beschrijving
nodig van het lumen van het te bestuderen coronair vat. Om WSS aan atherosclerose
te relateren is ook informatie over de wand nodig, bijvoorbeeld de dikte van de
wand of de componenten van de aderverkalking in de wand.

De gouden standaard om het lumen en de wand van coronairen in patiënten in beeld te brengen is intravasculaire ultrageluid (IVUS). Echter deze beeldvormende techniek is invasief, waardoor deze beperkt toepasbaar is. Bovendien is IVUS een twee dimensionale afbeeldingstechniek waardoor het op zichzelf niet geschikt is om een 3D lumen te genereren voor de WSS berekeningen. Computer tomografie angiografie (CT) van de coronairen is een relatief jonge techniek die de afgelopen jaren grote ontwikkelingen heeft doorgemaakt, waardoor CT nu in termen van resolutie de beste techniek is om niet-invasief de coronairen in 3D in beeld te brengen. In dit proefschrift is onderzocht of CT angiografie kan worden toegepast om de relatie te leggen tussen WSS en aderverkalking in de coronairen.

Met CT angiografie kunnen zowel het lumen als de wand in beeld worden gebracht. In hoofdstuk 2 is op kwalitatieve wijze de relatie gelegd tussen WSS en aderverkalking in coronaire bifurcaties met CT. In deze studie kon met CT worden bevestigd dat aderverkalking vaker voorkomt in regio's met lage WSS dan in regio's met hoge WSS. Daarbij werd tevens gezien dat aderverkalking pas in de hoge WSS locaties voorkwam als ook de lage WSS regio's waren aangedaan. Daardoor kon worden afgeleid dat aderverkalking ontstaat in de regio's met lage WSS en vervolgens groeit in de richting van gebieden waar een hoger WSS is.

Hoewel het kwalitatief relateren van WSS en aderverkalking dus mogelijk is, is uit studies waarbij wand en lumen grootte op CT werd vergeleken met IVUS gebleken dat deze maten nog teveel afwijken om kwantitatief deze relatie te leggen. Daarom is een reconstructietechniek ontwikkeld waarmee 3D patiëntspecifieke geometrieën van de coronairen gegenereerd kunnen worden door de nauwkeurige 2D data van IVUS te combineren met de 3D data uit CT. Op basis van anatomische kenmerken die in beide afbeeldingstechnieken nauwkeurig konden worden geïdentificeerd konden lumen- en wandcontouren van IVUS op de 3D middenlijn van het lumen geplaatst worden die in CT wordt bepaald. Dit resulteert in een 3D lumen geometrie die voldoende nauwkeurig is om WSS in te berekenen. Deze reconstructie techniek is gepresenteerd in hoofdstuk 3 en biedt de mogelijkheid om WSS en aderverkalking kwantitatief met elkaar te relateren. Omdat de locatie van IVUS beelden door middel van de reconstructietechniek bekend is in relatie tot de CT beelden, biedt de reconstructietechniek tevens de mogelijkheid om CT beelden en IVUS beelden naast elkaar te leggen en zo lumen en wand informatie in CT beelden te valideren tegen de gouden standaard IVUS.

Deze laatste toepassing van de reconstructietechniek is gebruikt in hoofdstuk 4 en 5. In hoofdstuk 4 is bepaald met welke nauwkeurigheid plaques gedetecteerd kunnen worden met CT. Meerdere personen hebben de CT beelden geïnterpreteerd en aangegeven op welke locaties ze aderverkalking zagen en wat voor een type aderverkalking het was (zonder calcificatie, gedeeltelijk gecalcificeerd of geheel gecalcificeerd). Vergelijking van hun interpretaties onderling en met de IVUS beelden maakte duidelijk dat het detecteren en typeren van aderverkalking nog niet zo gemakkelijk is. De interpretaties verschilden veel tussen de personen; de vergrootte afbeelding van calcificaties op CT belemmerde het zicht op niet gecalcificeerde gedeelte van de plaque; en plaques zonder calcificaties konden alleen betrouwbaar gezien worden als de plaque een dikte had van meer dan 1 mm. Dat ook het detecteren van calcificaties in de wand niet zonder meer goed gaat met CT, blijkt uit de studie in hoofdstuk 5. Alleen grote calcificaties in de wand kunnen betrouwbaar gedetecteerd worden op de CT beelden, terwijl de kleine calcificaties worden gemist. Het detecteren van plaque en het benoemen van plaque type op uitsluitend op basis CT beelden blijft voorlopig lastig en onvoldoende accuraat voor het leggen van een kwantitatieve relatie tussen WSS en aderverkalking.

De reconstructietechniek is in hoofdstuk 6 toegepast om kwantitatief een relatie te leggen tussen WSS en aderverkalking. IVUS en CT beelden van patiënten met een plaque ruptuur werden gebruikt om 3D patiëntspecifieke reconstructies te maken van het lumen, de wand en de locatie van de ruptuur. In de resulterende 3D geometrie werd de WSS berekend, waardoor kon worden aangetoond dat rupturen niet alleen vaker stroomafwaarts dan stroomopwaarts op de plaque voorkomen, maar ook dat de WSS op de locatie van de ruptuur gemiddeld hoger is dan de WSS op de plaque. In hoofdstuk 7 wordt de reconstructietechniek toegepast om CT te combineren met IVUS data en infrarode spectroscopische beelden om zo vetophopingen in de vaatwand zichtbaar te maken. Door deze toepassing kan de WSS ook gerelateerd worden aan de componenten in de vaatwand die een belangrijke rol spelen in het proces van aderverkalking. Er zijn dus volop mogelijkheden om door middel van de reconstructietechniek verschillende aspecten van aderverkalking in relatie met WSS te onderzoeken.

Omdat CT een 3D beeldvormende techniek is, heeft het als bijkomend voordeel ten opzichte van IVUS dat ook de zijtakken van de coronairen in beeld kunnen worden gebracht. Wanneer de zijtakken worden meegenomen in de WSS berekeningen kan ook de WSS dicht bij de vertakking worden berekenend, wat interessant is omdat dit een locatie is waar aderverkalking bij voorkeur ontstaat. Echter om WSS te berekenen

in geometriën met zijtakken zijn er aannames nodig om de verdeling van het bloed over de verschillende zijtakken in te kunnen voeren in de berekeningen. In hoofdstuk 8 zijn twee methoden gepresenteerd om een schatting te doen van de verdeling van het bloed over de zijtakken: een gebaseerd op een energiebeschouwing, en de ander gebaseerd op metingen uit de literatuur. De keuze van model had effect op de absolute waarden van de berekende WSS; echter wanneer de WSS relatief werd berekend ten opzichte van de locale WSS, dan was er met name in de stukken tussen de zijtakken weinig verschil in de WSS resultaten van beide modellen. Indien men geïnteresseerd is in absolute WSS waarden vlakbij de zijtakken dan lijkt het verstandig om het model te grbuiken dat gebaseerd is op metingen uit de literatuur.

Door de nauwkeurigheid van IVUS te combineren met de 3D informatie van CT is het dus mogelijk om WSS en aderverkalking patiëntspecifiek en kwantitatief aan elkaar te relateren. Echter de noodzaak voor het gebruik van invasief verkregen IVUS beelden beperkt de toepassing van deze techniek in grote patiëntengroepen en de toepassing van meerdere metingen over de tijd in dezelfde patiënt. Op dit moment is CT angiografie veelbelovend om op grotere schaal WSS te onderzoeken in relatie tot aderverkalking, echter de resolutie van CT zal moeten verbeteren voor kwantitatieve analyses op basis van CT beelden alleen mogelijk zijn. Ontwikkelingen op het gebied van CT, automatische segmentatie algoritmen, en voortschrijdend inzicht op het gebied van WSS, ontwikkeling, behandeling, en preventie van aderverkalking zullen richting moeten geven aan vervolgonderzoek zoals is bediscussieerd in hoofdstuk 9.

INHOUD

Contents

Introduction

This chapter gives an introduction to coronary atherosclerosis, wall shear stress and computed tomography (CT) angiography. It starts with a description of the pathology of coronary artery disease, one of the most important causes of death worldwide. It continues with background information on the development and progression of atherosclerosis, an inflammatory disease found in large arteries. Wall shear stress (WSS) is introduced and a summary is given about the known and hypothesized roles of wall shear stress in atherosclerosis development. Existing methods and necessary imaging modalities to study WSS in relation to atherosclerosis are summarized. CT angiography is an upcoming imaging modality that might aid WSS research and therefore also introduced. This chapter concludes with the scope and outline of this thesis.

1.1 CORONARY ARTERY DISEASE

Cardiovascular diseases are still considered the world's leading cause of death. In 2004, 12.9 million people (21.9%) died from either coronary heart disease (12.2%) or stroke and other cerebrovascular diseases (9.7%) [WHO-03]. Cardiovascular disease is known as a disease of the developed countries. However, in absolute numbers almost three times as many people die from it in the developing countries [Mackay-04]. In the Netherlands in 2007 for the first time cancer instead of cardiovascular disease was the leading cause of death (34.2% versus 29.8%) [Poos-08]. The decrease in cardiovascular deaths is mainly due to adequate treatment since the prevalence of the disease is constant after an severe increase in the seventies and eighties [Feskens-06]. And although cancer now predominates the causes of death, coronary artery disease costs still more lives than lung cancer, the number one cancer.
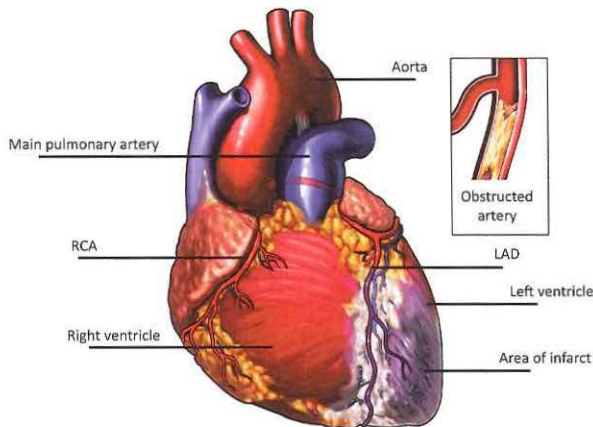
FIGURE 1-1: External view of the anterior side of the heart with the large arteries and coronary arteries depicted. Two coronary branches originate at the aortic root, just above the aortic valve. The right coronary artery (RCA) springs from the right aortic sinus, and runs over the epicardial side of the right ventricle branching into smaller arteries that penetrate into the muscle. Similarly, the left main (LM) artery originates from the left sinus. This artery branches within the first centimeters into two large arteries; the left anterior descending artery (LAD), supplying blood to the front side of the left ventricle, and the left circumflex artery (LCX), which supplies the backside of the left ventricle. In this image atherosclerosis buildup obstructs the LAD and deprives the myocardium downstream from blood. (©1997-2010 Nucleus Medical Art, Inc. All rights reserved).

The coronary arteries are the vessels that supply the heart muscle (the myocardium) with blood. They deliver oxygen and nutrients that the heart requires to contract (Figure 1-1). In case of coronary artery disease the coronary circulation fails to supply the myocardium with adequate amount of blood, and thus depriving it from oxygen. This can cause part of the myocardium to die with heart failure, arrhythmias or death as possible consequences. The main cause of coronary artery disease is the build up of atherosclerotic plaque in the wall of the coronary artery. This build up is very gradual and over a long time. The development of a plaque goes unnoticed since the coronary wall has the capacity to remodel. The remodeling of the artery wall prevents that the plaque grows into the lumen despite the wall thickening. Discomfort or events due to oxygen deprivation happen when at a certain moment either the maximum remodeling capacity of the wall is reached and the atherosclerotic plaque becomes flow limiting or because the atherosclerotic plaque bursts open and the contact of its contents with the blood causes thrombus formation, which can (partially) close the lumen.

Once the coronary artery disease is revealed, the severity of the disease is graded by imaging and/or functional measurements to decide upon treatment. In the most severe cases immediate revascularization of the coronary artery is necessary by open heart by-pass surgery or by stent placement during percutaneous catheterization. Medication, such as lipid-lowering drugs, is prescribed to prevent new events. Whether treatment is by a combination of revascularization and medication or medication alone, it will always be accompanied by an advice in lifestyle changes to minimize the modifiable risk factors. The most important modifiable risk factors include high blood pressure, tobacco use, high cholesterol, alcohol, obesity, physical inactivity, and low fruit and vegetable intake. Unfortunately no remedy is available to decrease the non-modifiable risk factors for coronary atherosclerosis as advancing age, gender, ethnicity, and heredity [WHO-03, Mackay-04].

1.2   ATHEROSCLEROSIS

Atherosclerosis is a progressive inflammatory disease in the wall of large arteries. It is characterized by accumulation of lipids and fibrous tissue in the wall. Already at an early age, adaptive intimal thickening is observed [Stary-87] at sites that are predisposed to lesion formation [Stary-92]. These regions include the branch points of arteries, which experience disturbed flow. This earliest appearance of atherosclerosis, the fatty streak, is formed by lipid particles accumulating in the intimal part of the

arterial wall [Stary-94, Stary-00]. Here these particles undergo chemical alterations (oxidation) which stimulate the endothelial cells to display adhesion molecules to catch monocytes from the blood [Libby-02]. These inflammatory cells are then lured into the arterial wall where they become macrophages. These macrophages ingest the modified lipids, filling themselves with lipid droplets and become 'foam cells'. Gradually these foam cells migrate deeper into the intima and heterogenous droplets of lipid are formed [Stary-00, Libby-02].

Once these lipid droplets become separate pools of lipid, lipid cores, the fatty streak has become an atheroma. Inflammatory molecules promote further growth of the plaque and formation of a fibrous cap over the lipid core. Smooth muscle cells are induced to migrate to the top of the intima, multiply and produce a fibrous matrix over the lipid contents, the fibrous cap, which separates the lipid content from the blood [Libby-02]. This process increases the size of the plaque, but outward remodeling prevents severe lumen narrowing [Glagov-87].

Inflammatory molecules secreted by the foam cells can weaken the cap by digesting matrix macromolecules and by damaging smooth muscle cells. These changes can thin the fibrous cap and render it susceptible to rupture. These rupture prone plaques are also called vulnerable plaques. These vulnerable plaques have retrospectively been characterized as having a lipid-rich core, a thin fibrous cap with macrophage accumulation together with decreased smooth muscle content and eccentric expansive remodeling [Falk-95, Virmani-00, Schaar-04]. When such plaque ruptures, blood will coagulate as a consequence and the thrombus might occlude the artery. The thrombus may eventually resorb and wound healing starts. This event activates new responses among which, smooth muscle cell multiplication, migration, and matrix synthesis [Libby-02]. The fibrous cap thickens again, but will now protrude into the lumen. This process can repeat itself. The resulting plaque includes haematoma, haemorrhage and thrombus deposits. It has to be noted that not all atheromas will evolve into a vulnerable plaque type. Some develop into lesions in which calcification predominates, in others an abundance of fibrous tissue is formed [Stary-00, Libby-02].

The different stages of atherosclerotic disease are hard to distinguish. Different classifications have been proposed [Stary-95, Virmani-00] depending on the presence of macrophages and lipid, disorganization and degradation of the cell layers in the wall, the organization of extracellular lipid, the degree of remodeling, the presence and size of fibrous tissue covering the plaque, the presence of a haematoma, haemor-

rhage and thrombotic deposits, the presence of neovasculature [Virmani-05], and the amount of calcifications. Since atherosclerosis is very hard to study in humans during their lives, many issues upon the development, progression and differentiation to plaque types are still under investigation.

1.3 WALL SHEAR STRESS

1.3.1 SHEAR STRESS IN VASCULAR BIOLOGY

Wall shear stress (WSS) is the (tangential) drag force induced by the blood flow acting on the inside of the vascular wall. Normal WSS values differ per species, vessel type, location and age [Samijo-98]. In healthy human carotid arteries for example values of 1.5 Pa are found, whereas in the brachial arteries WSS's of 0.48 Pa [Dammers-03] and in coronary arteries of 0.68 Pa [Doriot-00] are reported. Although the magnitude of the WSS is very small in comparison to the blood pressure, it can be sensed by the endothelial cells [Bhullar-98]. The level of WSS is actively maintained in the vascular system. Changes in WSS due to a change in flow result into immediate adaptation of the vascular tone and subsequently by structural remodeling, with adjustments in vascular diameter as a consequence [Furchgott-80]. The success of this shear stress stabilizing process dependents on the condition of the endothelium and is diminished when the mono-layer of endothelial cells is damaged.

1.3.2 SHEAR STRESS AND LOCALIZATION OF ATHEROSCLEROSIS

Atherosclerotic plaques are not uniformly distributed in the arterial system. Typical predilection sites of the coronary plaques are at the inner curve of the artery and near side-branches [Friedman-93]. Thus despite the systemic risk factors, localizing factors are involved in the origination of atherosclerosis. The localization of atherosclerotic plaques is related to local haemodynamics and in particular to the local WSS distribution [Caro-71, Zarins-83, Motomiya-84, Asakura-90].

The response of endothelial cells in the presence of low WSS largely explains the local susceptibility to atherosclerosis. Low WSS enhances the oxidation and accumulation of lipids in the vessel wall [Murase-98]. The oxidative stress in the wall is increased because the production of nitric oxide (NO) is diminished. NO scavenges the oxygen radicals, prevents proliferation of smooth muscle cell, is anti thrombotic and

anti atherogenic [Malek-99]. Furthermore, growth factors in the vessel wall stimulate the migration and proliferation of the smooth muscle cells. Also the inflammatory process of atherosclerosis is WSS regulated, since low WSS enhances the expression of adhesion molecules that recruit monocytes and leukocytes into the vessel wall [Mohan-99]. In contrast, normal or high WSS protects the endothelium from inflammatory activity, stimulates proliferation and diminishes apoptosis of the endothelial cells and increases the expression of anti oxidative enzymes [Malek-99].

1.3.3   SHEAR STRESS AND GENERATION OF THE VULNERABLE PLAQUE

Since the lumen diameter is preserved by WSS regulation, the original WSS distribution will be maintained for a long period of time including the unfavourable, atherogenic low WSS. This might explain why atheromas develop into eccentric lipid-loaden plaques. At a certain moment lumen preservation is not possible anymore and the plaque starts to encroach into the lumen and to cause lumen narrowing. As a consequence the local WSS will increase at the upstream side of the plaque. Since plaque ruptures or ulcers are frequently observed at the upstream side of a plaque [Fujii-03, Lovett-03, de Weert-09], it is hypothesized that the change in WSS biologically influences the underlying plaque composition and possibly plaque vulnerability [Slager-05].

Increased shear stress at the midcap, upstream of the stenosis might increase the local NO production, which induces tissue regression due to apoptosis of the smooth muscle cells [Slager-05]. The local high WSS might also be responsible for weakening of the fibrous cap because of high WSS induced excretion of plasmins by the endothelium. Therefore, it is hypothesized that high WSS is involved in plaque destabilization, which is now investigated in several studies [Krams-06, Gijsen-08, Groen-08].

Wall shears stress has thus proven to be an important factor in the localization of early atherosclerotic lesions. However still a lot is unknown about the progression of atherosclerotic plaques into the different plaque types and what factors determine plaque composition. Wall shear stress might be an important factor to study in these processes.

1.4 ASSESSMENT OF SHEAR STRESS AND CORONARY ATHEROSCLEROSIS

1.4.1 SHEAR STRESS MEASUREMENTS

To study the influence of WSS on atherosclerotic plaque development and destabilization, simultaneous assessment of WSS and vessel wall characteristics is necessary. Local WSS can be obtained if a good description of the local velocity profile is available. Then WSS can be calculated by the multiplication of the local viscosity of the blood and the change in velocity at the boundary layer of fluid at the vessel's wall. The number of techniques that can measure a velocity profile in human coronary arteries and in combination are able to give an accurate description of the geometry of the coronary wall, is limited [Wentzel-01]. Velocity profiles obtained by intravascular (Doppler) ultrasound [van der Steen-00] lack accuracy because the velocity profile is disturbed by the catheter [Krams-99]. Coronary magnetic resonance imaging (MRI) has the ability to measure a flow profile [Schiemann-06], but spatial and temporal resolution are at this moment still too limited to acquire the geometry of the lumen and the wall.

1.4.2 SHEAR STRESS CALCULATIONS

To overcome the requisite to obtain both the velocity profile and the wall characteristics simultaneously, the local WSS is often obtained by computational fluid dynamics (CFD). CFD is a numerical technique to solve and analyse problems in the fluid domain. The technique involves discretization of the spatial domain to form a volume mesh and then apply a suitable algorithm to solve the equations of motions (the Navier-Stokes equations in case of simulating blood flow in the coronary arteries). To simulate WSS by solving a CFD problem, a description of the 3D geometry of the coronary lumen is needed. In addition material models have to be chosen for the vessel wall and the blood. Also boundary conditions have to be prescribed that define the behaviour of the materials at the boundaries of the problem. In case of the coronary arteries, boundary conditions such as flow and/or pressure have to be prescribed at the in,- and outflow parts of the coronary geometry. With the aid of dedicated CFD software the defined problem can numerically and iteratively be solved resulting in

a description of the velocity and pressure at every point in discretisized geometry. With post-processing the WSS can be calculated from the simulated velocity profile. The great advantage of this technique over WSS measurements is that WSS can be calculated at any position in the geometry and limited flow information is needed.

1.4.3   CORONARY WALL IMAGING: INTRAVASCULAR ULTRASOUND

In addition to the WSS, also vessel wall characteristics are needed to study WSS in relation to atherosclerosis. Intravascular ultrasound (IVUS) is considered as the gold standard for in-vivo coronary lumen and wall assessment [Mintz-01]. It is a catheter-based imaging technique that provides real-time, high resolution, 2D, tomographic grey-scale images of both coronary lumen and wall. A catheter is promoted into the coronary artery with at its tip a transducer that sends and receives high-frequency (20-40 MHz) ultrasound. The reflections of the ultrasound waves at the different tissue types are recorded and converted to cross-sectional images as the catheter is pulled back from the distal part of the artery towards the ostium. The dimensions of the coronary wall and lumen, and some morphology of the coronary plaque, such as the presence of calcifications, can be assessed by IVUS. Except for grayscale images, new analysis techniques of the IVUS data have been developed which add information about the composition of the artery wall [Nair-02, Schaar-05].

1.4.4   CORONARY IMAGING FOR SHEAR STRESS CALCULATIONS

The application of CFD for WSS calculation has proven its benefits in atherosclerosis research. As mentioned before, the application of CFD requires a 3D description of the geometry of the artery under study. For the larger arteries, non-invasive imaging modalities are emerging that allow segmentation of the 3D lumen information. MRI, ultrasound and computed tomography (CT) are often used for that purpose in the carotid arteries, femoral arteries and the aorta. The small size and movement of the coronary arteries hinder non-invasive 3D imaging: Biplane angiography gives no information about the wall, IVUS is a 2D technique and thus lacks information about the curvature of the artery, and the resolution of MRI is too limited.

To overcome the 2D aspect of IVUS, a technique was developed in 1995 based on the combination of biplane angiography and IVUS (ANGUS) [von Birgelen-95, Slager-00]. IVUS provides the lumen and wall contours while angiography is used for the reconstruction of the 3D curvature of the artery. Although no flow information is present

for the CFD simulations with this technique, it provides valuable information about relative WSS values. To obtain absolute WSS distribution the technique can be extended with flow measurements obtained during the same catheterization procedure. The technique is now applied by several research groups and has proven to be a valuable tool to study WSS in relation to atherosclerosis in the coronary arteries [Krams-97, Gijsen-03, Stone-03, Wentzel-03, Bourantas-05, Wahle-06].

Unfortunately, the ANGUS technique has some drawbacks. The technique requires invasive imaging and simultaneous acquisition of IVUS and biplane angiography, which is not possible in many catheterization rooms. In addition, the reconstruction technique is very time-consuming and lacks easy incorporation of the side-branches into the geometry because the IVUS acquisition is only performed in the main branch [Gijsen-07].

1.5 CORONARY CT ANGIOGRAPHY

To overcome the limitations of the ANGUS technique, a 3D non-invasive imaging technique is necessary with enough spatial and temporal resolution to image the lumen and wall with high accuracy and ideally this technique also provides the flow through the coronary arteries. Such imaging technique does not yet exist. However due to the fast technical developments in spatial and temporal resolution of computed tomography over the last decade, this is the now the 3D non-invasive imaging technique with the highest resolution and most potential to image the coronary arteries non-invasively for WSS analysis.

Computed tomography (CT) is a medical imaging technique that uses the attenuation of X-ray beams by the human body to image the internal structures of the body. The X-ray tube that transmits the beam, is positioned opposing of the detectors in the gantry, which rotates around the patient. While the patients is continuously advanced through the gantry, a collimated roentgen beam passes through the patient and the attenuated radiation is collected with the detectors. The placement of several parallel detector rows instead of one detector in 1998 was the herald for cardiac CT since this innovation accelerated the scanning procedure, which is necessary to image the rapid moving heart. Whereas the technology started with 4-slice CT (4 detectors in row), recently the 128-row, 256-row and 320-row CT's [Rybicki-08] have been introduced, which the latter allows imaging of the heart within one heart-

beat. Parallel to the increase of detector rows the dual source CT was developed and introduced in 2006. This scanner consists of two x-ray tubes and two detectors mounted perpendicularly in the same gantry [Flohr-06]. This technique halves the temporal resolution but also allows for dual energy acquisition [Ruzsics-08].

Coronary CT angiography uses intravenous contrast injection to highlight the arteries. With the aid of electrocardiographic (ECG) synchronization an image of the heart and the coronary arteries can be reconstructed in a 3D isotropic voxel space during one of the cardiac phases. The technique has proven to be very accurate in detection of significant coronary artery stenosis in comparison with traditional angiography [Bastarrika-09], although stenosis grading [Husmann-09] and lumen dimension assessment is still challenging [Caussin-06].

In addition to the lumen, also the coronary wall can be studied. The amount of calcium in the coronary wall is already since the use of electron beam CT applied for risk stratification, but since it has been demonstrated that CT angiography can depict calcified and non-calcified plaque components [Becker-00], risk stratification and risk management based on CT angiography has gained interest. The rationale is that different clinical manifestations of coronary artery disease, come with different plaque composition [Burke-97, Leber-03, Ehara-04].

Ex-vivo plaque characterization based on the attenuation of the components of the coronary plaque has been shown to correlate reasonably with histological findings [Becker-03]. In-vivo plaque characterization based on attenuation is more difficult because of volume averaging effects, the influence of the contrast in the lumen [Cademartiri-05] and the overlap in grayscale values (Hounsfield Units) between plaque types [Schroeder-04]. Volumetric measurements of the plaque are used to estimate the plaque burden, but manual annotation has high inter-observer variability and the volumes of non-calcified and mixed plaques are underestimated, while calcified plaque volumes are overestimated. Fortunately, newer software applications reduce the inter-observer variability [Blackmon-09] and show promising results in volumetric lumen and wall assessment as compared to IVUS [Boskamp-04, Sun-08, Schepis-09]. Together with the trend of decreasing radiation exposure during acquisition, coronary CT angiography might even aim at serial imaging of high-risk patients.

1.6   SCOPE AND OUTLINE

In the previous paragraphs the importance of research to coronary atherosclerosis is stressed, since it is still is one of the most important causes of death. In the presence of systemic risk-factors, WSS is the localizing factor of atherosclerosis. In addition, the biological response of the endothelium on WSS is hypothesized to be an important factor in the progression and destabilization of plaques and thus an important parameter for atherosclerosis research. WSS in relation with atherosclerosis can be studied in-vivo with the aid of computational fluid dynamics. This technique requires a 3D description of the coronary artery under study, which can be obtained by a reconstruction technique based on biplane angiography an IVUS. The limitations of this technique might be resolved by a non-invasive 3D imaging technique with enough resolution to obtain and the 3D geometry of the coronary lumen and to obtain geometrical and morphological information of the coronary wall. Coronary CT angiography is at this moment the best non-invasive imaging technique arteries in terms of resolution to image coronary arteries.

In this thesis we investigated how coronary CT angiography can be applied to study the relation between WSS and atherosclerosis as stand-alone non-invasive imaging technique or in combination with invasive imaging techniques.

The quality of WSS and wall information that can be obtained by CT angiography will determine the extent of its application as stand-alone imaging technique in atherosclerosis research. An exploratory study described in *Chapter 2,* shows that with coronary CT angiography it is possible to relate the presence of plaque presence and WSS in a qualitative way near bifurcations. However, this study also indicated that CT angiography as a stand-alone modality was not yet suitable to study these relations in a quantitative way. Automatic segmentation a is still a challenging research task, thus obtaining an accurate and reproducible 3D description of the lumen is hard. In addition, not a lot is known about the quality of the detection and classification of the different plaque types.

Since coronary CT angiography cannot be used as stand-alone technique for WSS calculations and more extensive validation is still needed, a reconstruction technique based on placing IVUS images into 3D on the lumen centerline of CT is described in *Chapter 3*. This technique allows for side-by-side comparison of CT and IVUS, but also results in a 3D reconstruction of the IVUS lumen and wall contours which is suitable for WSS analysis.

In the next two chapters this reconstruction technique is used to compare IVUS and CT side-by-side, such that the plaque detection on CT could be validated against IVUS. In *Chapter 4* ex-vivo human coronary arteries are imaged to determine the minimal size of a non-calcified plaque that can be detected by CT angiography. With the same technique, but now in patients, the detection of coronary calcifications by CT angiography was validated against IVUS in *Chapter 5*.

These validation studies showed the potential of CT angiography but also demonstrated that IVUS is still needed to obtain accurate wall and lumen geometry to study WSS in relation to atherosclerosis. In *Chapter 6*, the reconstruction technique described in Chapter 3, is used for the first time to study WSS as WSS patterns are related to coronary plaque rupture.

In *Chapter 7* a case report is presented that demonstrates that the reconstruction technique is not limited to IVUS alone, but also information from IVUS-derived imaging techniques, or information of techniques added to an IVUS catheter such as in this case near-infrared spectroscopy (NIR-IVUS), can be placed into 3D. In this report the chance of lipid presence in the artery wall is added as wall information, which now can also be related to WSS.

One of the advantages of the CT derived coronary geometry is that it is not limited to the main branch as is IVUS, but that also the side-branches can be incorporated into the WSS analyses. However incorporating side-branches goes with applying extra boundary conditions for the CFD, since the flow division over the side-branches has to be known. Volumetric flow cannot be measured thus a good estimation has to be made based on the geometry under study. In *Chapter 8* the influence of different models to prescribe the outflow boundary conditions on the WSS distribution is investigated.

Chapter 9 accomplishes this thesis with a summary of the studies, and a discussion about the role of CT angiography in clinic practice and in studies relating WSS and atherosclerosis.

Plaque and shear stress distribution in human coronary bifurcations

In this chapter the plaque distribution and morphology near coronary bifurcations is non-invasively assessed with 64-slice computed tomography and related to the wall shears stress (WSS) distribution. We demonstrated that plaque is mostly present in low WSS regions. In case of a plaque in a high WSS regions, this plaque is accompanied by plaque in an adjacent low WSS regions. It is therefore plausible that plaque grows from the outer wall (low WSS) of the bifurcation towards the flow divider (high WSS).

2.1 Introduction

The formation of atherosclerosis in coronary arteries is localized [VanderLaan-04, Slager-05]. A key player in the localization of atherosclerosis is low wall shear stress (WSS) [Malek-95, Cunningham-05]. In the presence of systemic risk factors, a vessel wall that is exposed to low WSS is more prone to develop atherosclerotic plaques [Giddens-93, Malek-99].

The WSS to which a vessel wall is exposed, is mainly determined by arterial geometry. In bifurcating arteries, the outer wall is exposed to low WSS compared to the flowdivider wall [Asakura-90, Tadjfar-04]. In curved arteries, low WSS regions are present at the inner bend, while the outer bend is exposed to high WSS [Kirpalani-99]. Intravascular ultrasound studies show that plaques are predominantly found in low WSS regions [Krams-97, Iwami-98, Tsutsui-98, Jeremias-00].

However, in clinical practice it is common to observe plaques that cause lumen narrowing not only at low WSS regions but also at the high WSS sensing flowdivider of coronary bifurcations. Even in the classifications schemes used for typing bifurcation lesions on coronary angiography, most of the bifurcation types have luminal narrowing in the flowdivider region of the side-branches [Lefèvre-00, Sianos-05]. Plaques incorporating the flowdivider are found more frequently in symptomatic patients, and thus may represent a more advanced stage of atherosclerosis. Apparently in this stage of the disease plaques are not limited to low WSS regions.

Angiography is only one of several imaging modalities to visualize the presence of atherosclerosis in the coronary arteries [Bhatia-03]. Recently several studies have shown the ability of multi-slice computed tomography (MSCT) angiography to detect coronary plaques non-invasively [Mollet-05]. In contrast to conventional angiography, MSCT angiography gives 3D information about the coronary geometry and not only the lumen is visible, but also the vessel wall harbouring the atherosclerotic plaque [Leber-03, van Mieghem-06] . This enables MSCT coronary angiography to detect atherosclerosis also in remodeled arteries without severe lumen narrowing [Achenbach-04, Leber-05].

In this study we imaged non-invasively with MSCT angiography the 3D geometry of the lumen and vessel wall of coronary artery bifurcations in patients. On the basis of geometry, we labeled regions in bifurcations according to the expected WSS in each region and related the WSS to the plaque frequency, distribution and morphology.

2.2 MATERIALS AND METHODS

2.2.1 STUDY POPULATION

We retrospectively studied 28 (18 male, mean age 59.9 ± 6.6 years) consecutive symptomatic patients, suspected of coronary artery disease who underwent MSCT coronary angiography. Patient demographics are given in Table 2-1. The patients had sinus heart rhythm, were able to hold breath for 15 seconds and had no contra-indications to iodinated contrast material. We only included patients who had not previously undergone percutaneous intervention or coronary bypass surgery, and had a heart rate lower than 65 beats per minute during scanning. Our institutional review board approved the study protocol, and all patients gave informed consent.

TABLE 2-1: Patient characteristics

Male	18 (64%)
Age, years (± stdev)	59.9 (6.6)
Symptoms	
Atypical chest pain	1 (4%)
Stable angina pectoris	11 (39%)
Unstable angina pectoris	4 (14%)
Non-ST-segment elevation myocardial infarction	10 (36%)
Asymptomatic	2 (7%)
Risk factors	
Hypertension	21 (75%)
Hypercholesterolemia	21 (75%)
Smoking	8 (29%)
Family history of acute coronary syndrome	7 (25%)
Diabetes mellitus	6 (21%)
Obese (body mass index ≥30 kg/m²	5 (18%)

N=28. Values are n (%) unless otherwise indicated

2.2.2   SCAN PROTOCOL AND IMAGE RECONSTRUCTION

The patient preparation, scan protocol, and image reconstruction procedure have previously been described [Mollet-05]. Briefly, patients with heart rates above 70 beats per minute received heart-rate-lowering drugs before scanning. Scanning was performed on a 64-slice MSCT scanner (Sensation64®, Siemens, Germany) according to a standardized optimized contrast (Iomeron 400®, Bracco, Italy) enhanced scanning protocol. A bolus tracking technique was used to synchronize the arrival of contrast in the coronary arteries with the initiation of the scan. Images were reconstructed with ECG-gating, initially during the mid- to end-diastolic phase (350 ms before the next R wave) with a temporal window of 165 ms. If image quality was poor, more reconstructions at different phases of the cardiac cycle were generated to improve it. The dataset with the best image quality was chosen for further processing. The in-plane resolution was approximately 0.3 mm and the slice thickness was 0.4 mm.

2.2.3   MSCT IMAGE PROCESSING

We investigated the plaque distribution in two bifurcations; 1) the LM-bifurcation, which is the branching of the left main (LM) coronary artery into the left anterior descending artery (LAD) and the left circumflex artery (LCX), and 2) the LAD-bifurcation, which is the bifurcation of the first diagonal artery (D_1) from the distal LAD (LAD_{dist}). To study these bifurcations the reconstructed MSCT datasets were exported from the scanner to MeVisLab (MeVis, Bremen, Germany), a software environment for image processing and visualization.

The two bifurcations were analysed separately. We defined a plane through each bifurcation, such that both the main branch and the side-branches were visible in this plane and that the angle between the side-branches was maximal (Figure 2-1A and B). Perpendicular to this plane and the vessel axis, one cross-section of each of the side-branches was obtained 1 mm distal to the flowdivider (see Figure 2-1C)

We excluded trifurcations from the analysis (n=21). Cross-sections were excluded when the diameter of the artery was < 1 mm (n=2), or when the plaque was too heavily calcified to clearly distinguish the lumen from the plaque (n=3), see also Figure 2-2. In total we analysed 65 cross-sections for this study.
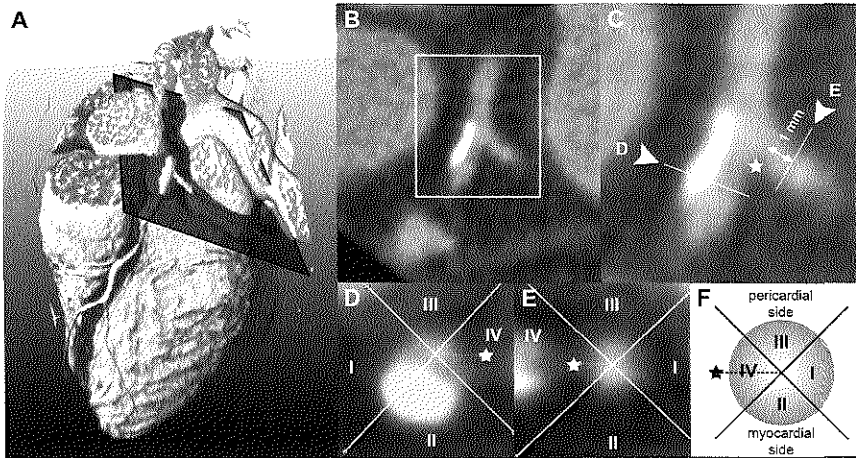
FIGURE 2-1: Selection of cross-sections from the bifurcation of interest. Panel A shows a volume rendered MSCT dataset with a plane through the mother and side branches of the bifurcation of interest. The Hounsfield Unit distribution in this plane is shown in B and a magnification in C. In C, the star indicates the flowdivider and the arrows indicate the position of the cross-sections shown in D and E. The sketch in F illustrates the division into parts and also the numbering according to the expected shear stress levels, which is also applied in D and E.

2.2.4   SHEAR STRESS

To relate the plaque location to WSS, we divided the cross-sections into four parts from the center of the lumen. The cross-section was divided is such way that the flowdivider was in the middle of one of the parts. We labelled the part covering the outer wall of the bifurcation I, the part facing the myocardial side of the heart II, the part facing the pericardium III, and the part containing the flowdivider IV (Figure 2-1D and E).

The bifurcation affects the WSS pattern primarily. High WSS is assumed in part IV due to the flow-division at the flowdivider, while in part I, the outer, non-flowdivider wall, low WSS is expected. Besides the effect of the bifurcation, the curvature of the artery over the myocardium also influences WSS [He-96]. In comparison to part III, the WSS is assumed to be lower in part II, because the inner wall of a curved vessel is subjected to lower WSS than the outer wall. Thus, the numbering of the parts is according to the expected WSS: in part I the lowest and in part IV the highest WSS (Figure 2-1F).
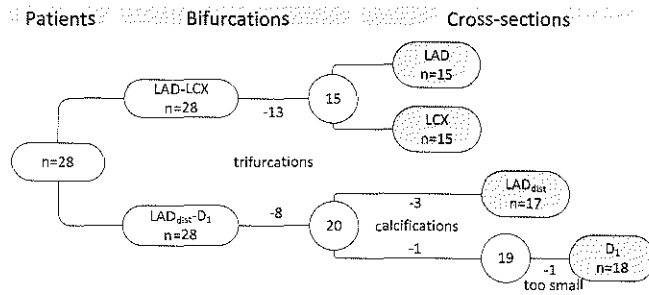
FIGURE 2-2: Exclusion numbers of bifurcations and cross-section because of trifurcations, calcifi-cations and artery size. Abbreviations: LAD – Left anterior descending coronary artery, LCX – Left circumflex coronary artery, LAD_{dist} – distal left anterior descending coronary artery (distal to first diagonal), D_1 – first diagonal coronary artery.

2.2.5 PLAQUE IDENTIFICATION

In each cross-section, all parts were inspected for the presence of plaque. Plaque was defined as any discernable structure with 1) a lower attenuation than the con-trast enhanced lumen and higher attenuation than the surrounding epicardial fat or 2) an attenuation ≥ 140 HU that could be separately visualized from the lumen (cal-cified part). The plaque had to be present at the cross-section of interest and at at least one cross-section adjacent (0.5 mm distance) to the cross-section of interest. When a cross-section had calcified parts, we also denoted the part that contained the densest structure, thus with the highest Hounsfield Unit.

The cross-sections with plaque present in only 1 part, we called minimally inflict-ed. When in 2, 3 or 4 parts plaques were observed we called these cross-sections respectively mildly, moderately and severely inflicted.

2.2.6 STATISTICAL ANALYSIS

To test whether plaque occurs in a preferential part of a cross-section, we used the numerical values assigned to each part. For each cross-section we computed the mean of the numbers of the parts that contain plaque. This mean value we call the mean shear stress index (MSSI). For instance, when plaque is present in the low WSS regions, thus in part I and II, than the MSSI of that cross-section is $(1+2)/2 = 1.5$.

When plaques are randomly distributed over the numbered parts, and thus have no preferential location, the averaged MSSI is by definition 2.5. We denote this reference value as RMSSI. If the MSSI is lower than 2.5, plaque is located mainly in the low WSS parts of a cross-section, and if it is higher, plaque is mainly present in the high WSS parts of a cross-section.

We calculated the average MSSI over all cross-sections, and separately over the minimally, mildly, moderately and severely inflicted cross-sections and reported the values as mean±std. With a student-t-test we tested whether the averaged MSSI was significantly different ($p<0.05$) from the RMSSI of 2.5.

2.3 RESULTS

2.3.1 GENERAL

Most patients (96%) had plaque in one or more of the studied cross-sections. Of the 65 cross-sections 88% contained plaque. In the D_1 branch, which is generally smaller than the other inspected branches, atherosclerosis was observed less often than in the other branches. Only 75% of the D_1 cross-sections contained plaque versus 93%, 86% and 94% of the LAD, LCX and LAD_{dist} branches.

Calcified plaques were found in 62% of the patients, and in 29% of the cross-sections. Of the LAD_{prox} and LAD_{dist} 37% and 42% of the cross-sections were affected, whereas only 5% and 16 % of the LCX and D_1.

2.3.2 PLAQUE DISTRIBUTION

Plaques were found in low WSS parts I and II in 72% and 62 % of the cross-sections. The high WSS parts III, and IV were less often affected than parts I and II, only in 38% and 31% of the cross-sections (Figure 2-3).

The distribution of the plaque configurations is in more detail given in Figure 2-4. From the top to the bottom the rows show the possible plaque configurations for minimally, mildly, moderately and severely inflicted cross-sections. For each configuration the number of observations is given as well as the corresponding MSSI value.
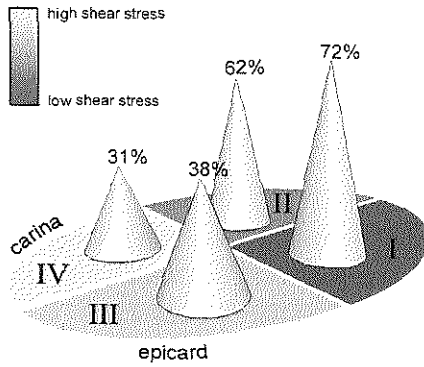
FIGURE 2-3: Plaque distribution. The figure gives the percentage of occurrence of plaque in each part, i.e. 72% of all low WSS parts I were inflicted with plaque.
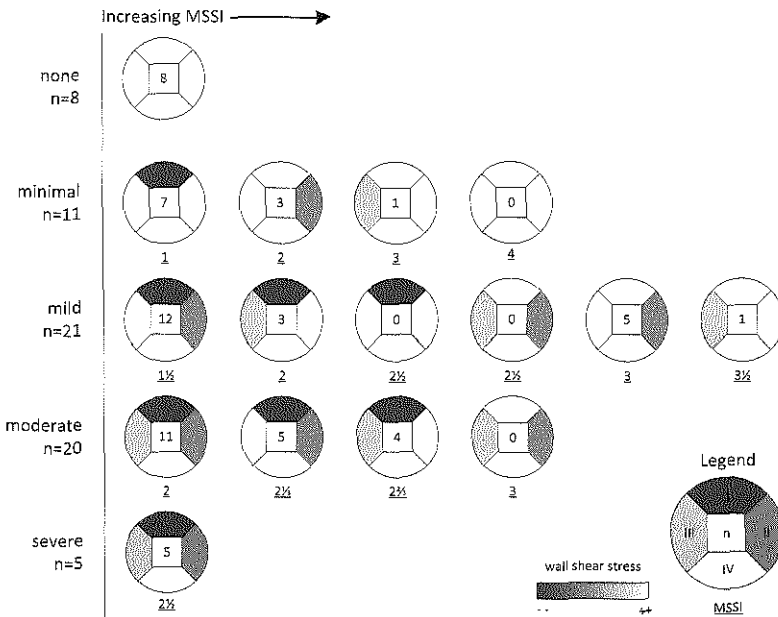
FIGURE 2-4: Plaque configurations. All possible plaque configurations are shown, sorted from top to bottom on the basis of the number of affected parts and from left to right according to increasing mean shear stress index (MSSI). Each configuration depicts both the number of times (N) that it is observed and its MSSI (underlined). The parts are colored according to the expected wall shear stress level (see legend).

We found 8 cross-sections without plaque. In 10 of the 11 minimally inflicted cross-sections plaque was present in the low WSS parts I or II. The high WSS part IV was not affected once. In the 21 mildly inflicted cross-sections (2 parts inflicted per cross-section) we did not find configurations in which plaques are opposite to each other. Again, as in minimally inflicted cross-sections, the low WSS parts contained plaque most often. In the 20 moderately inflicted cross-sections (3 parts inflicted) plaque was always at least present in the lowest WSS part I. We found 5 severely inflicted cross-sections.

Plaque at the flowdivider was found in 20 out of the 65 analysed cross-sections. The flowdivider was never affected in minimally inflicted cross-sections, while 6 out of 21 of the mildly inflicted cross-sections, 9 out of 20 of the moderately inflicted cross-sections, and 5 out of 5 of the severely inflicted cross-sections were affected in the flowdivider. In 19 out of the 20 cross-sections, plaque in the flowdivider was accompanied by plaque in low WSS regions I or II.

Figure 2-3 also shows that the plaque configurations with the lowest MSSI's are the configurations that we observed most frequently. Figure 2-5 shows the averaged MSSI for all, the minimally, mild, moderately and severely inflicted cross-sections. If the plaques are located preferentially at specific regions, the MSSI will be significantly different from the reference value, the RMSSI, which is 2.5. The averaged MSSI over all cross-sections was with 2.02 ± 0.62 lower than the RMSSI ($p<0.05$). When we divided the cross-sections according to the severity of infliction, the averaged MSSI's are also lower than the RMSSI with the exception of the severely inflicted cross-sections, which by definition equals the RMSSI. The MSSI increases with the severity of infliction because high WSS parts get involved.

2.3.3 CALCIUM DISTRIBUTION

Similar to the plaque, the densest calcium spot was mostly found in the low WSS parts I and II. Both part I and part II were inflicted in 17% of the cross-sections while parts III and IV were only inflicted in 6% and 3% of the cross-sections.

Figure 2-6 shows all 19 cross-sections with calcium according to the severity of plaque inflictions from top to bottom. From left to right the configurations are ordered according to the part with the densest spot, which is indicated with a black dot in the cross-sections.
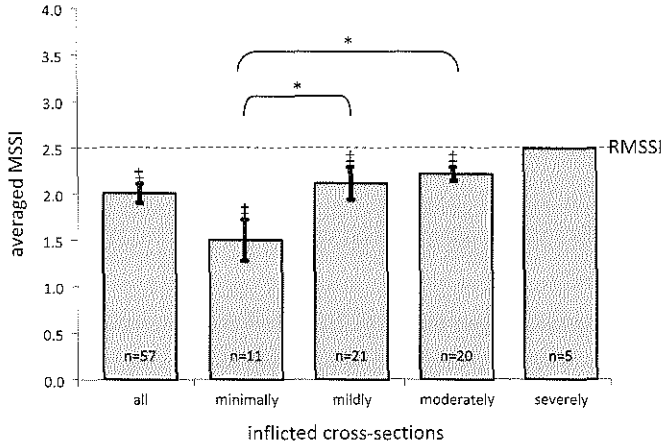
FIGURE 2-5: Mean shear stress indices (MSSI) of plaques. The averaged MSSI ± variance is shown of the plaque parts over all, the minimally, mildly, moderately and severely inflicted cross-sections. The reference MSSI (RMSSI) is indicated at 2.5. The number of cross-sections is indicated with n. *, significant difference ($p<0.05$) between the MSSIs. ‡, MSSIs lower ($p<0.05$) than the RMSSI.
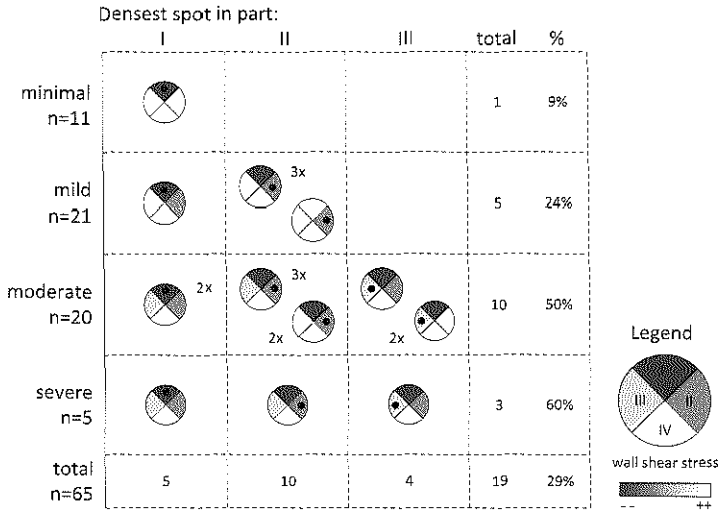
FIGURE 2-6: Plaque configurations with calcium are shown and sorted from left to right according to part with the calcium spot. From top to bottom, the cross-sections are sorted by the severity of plaque infliction. The • indicates the position of the densest calcium spot.

Of the 11 minimally inflicted cross-sections, only 1 (9%) was calcified. The percentage of cross-sections with calcium increased with the severity of infliction up to 60% for the severely inflicted cross-sections. The densest spot of the calcification was never found in high WSS part IV. Most of the calcified cross-sections (n=10) have the densest calcium spot in part II. Part I has the spot in 5 cross-sections and part III in 4 cross-sections. The plaques with the densest spot in part III always were in moderately or severely inflicted cross-sections.

2.4   DISCUSSION

We reported on the plaque distribution in human coronary arteries assessed by MSCT in relation to expected shear stress patterns. We demonstrated that plaques in coronary artery bifurcations are most often located in the low WSS regions and that plaques at the flowdivider, which is exposed to high WSS, are always accompanied by plaques in a low WSS region, from where plaques are supposed to originate.

To compare our findings with histological reports in literature on the different phases of atherosclerosis we distinguish three phases in our study. A minimally inflicted cross-section can be considered as early atherosclerosis, mildly and moderately inflicted cross-sections as more advanced atherosclerosis, and severely inflicted cross-sections as severe atherosclerosis. In early atherosclerosis we observed that plaque distal to a bifurcation was found mainly at the wall opposite the flowdivider. This is in agreement with histological findings of early atherosclerosis in the LM bifurcation of young adults [Svindland-83]. In an older population, Grøttum et al. studied the deposition of atherosclerosis also in the LM bifurcation [Grøttum-83]. Most plaques distal to the bifurcation were observed opposite to the flowdivider and slightly directed to the myocardium. In our study we observe plaque in similar regions. These are the regions where we expect low WSS.

Our results are not only supported by histological findings, but also by intravascular ultrasound studies on plaque distribution near coronary bifurcations. These studies often include patient groups who have lumen narrowing on angiography and who may thus have advanced to severe atherosclerosis. Shimada et al. demonstrated that the plaque area was larger at the opposite wall of the flowdivider than at the flowdivider itself [Shimada-06]. The influence of the curvature of the arteries near bifurcations was investigated by Iwami et al. [Iwami-98] using a combination of intravascular ultrasound and angiographic data. The percentage of plaque in the to-

tal cross-sectional plaque area was highest at the inner curve of the bifurcation and this was most pronounced in the most curved arteries. Badak et al. incorporated the position of the myocardium in their analysis. They found that when a side-branch was perpendicular to the artery the maximum plaque thickness was found at 190°± 70°, thus opposite the side branch, slightly in direction of the myocardium [Badak-03]. To compare our findings we calculated the average angle in a similar way in the mild and moderately diseased cross-sections and found that it was very close to that found by Badak, that is 205°± 68°. Thus, on the basis of the plaque distribution observed in our study and in other studies, we show that not only the bifurcation contributes to the low WSS region and initiates plaque formation, but also the curvature of the arteries over the myocardium.

Other studies lack detailed information on the distribution of calcifications with respect to the position of the bifurcation and myocardium. It is known that most calcium is found near bifurcations and that it initially occurs in the necrotic core of the plaque partly due to apoptosis of vascular smooth muscle cells or macrophages [Vattikuti-04]. In our data the calcium spot was found more often at the myocardial side (part II) of the coronary artery than at the outer wall of the flowdivider (part I), which is what one would expect on the basis of the plaque distribution. We observed calcium once in a cross-section that was mildly inflicted and thus was by our definition, an early from of atherosclerosis. Due to expansive remodeling, it is possible that an advanced plaque only occupies one part of the cross-section instead of growing into the high WSS parts. This might explain the presence of calcium in a cross-section with only one inflicted part.

Although we did not follow patients over time, several observations indicate that plaques grow circumferentially from a low WSS region into the high WSS flowdivider. The first observation that supports this, is that the flowdivider was never diseased in early atherosclerosis. Secondly, low WSS regions were in all stages of the disease most often affected. Thirdly, if there is plaque at the flowdivider, the low WSS regions are also diseased. The fourth observation, that plaques are always found adjacently in low and high WSS regions indicate that growth is indeed circumferential. We already mentioned that low WSS regions are predilection sites of early atherosclerosis. As the plaque matures, fissuring at the shoulders of the plaque can cause the plaque to grow from the low WSS region along the circumference of the lumen [Burke-01].

Many studies on plaque distribution in human coronary arteries use IVUS as imaging modality. With its high resolution, it is the gold standard for determining lumen and plaque size. However, IVUS is invasive and as 3D information is lost, it is hard to identify the pericardial and myocardial side of a bifurcation. The influence of the curvature of the artery over the myocardium on plaque localization can therefore not be taken into account. Currently, MSCT angiography is the only non-invasive imaging modality that can provide both 3D lumen and plaque distribution. High sensitivities and specificities are achieved in scoring significant lesions on 64-slice MSCT angiography images [Schmermund-05] and the first comparisons with IVUS on plaque measurements are promising [Leber-05].

However, due to limitations of the MSCT angiography technique, measuring the exact size and position of the atherosclerotic plaque remains a challenge. In the first place, partial voluming effects caused by the high intensity calcium and contrast agent can obscure the vessel wall. Secondly, the resolution of MSCT angiography images cannot compete with those of IVUS: MSCT angiography cannot visualize small branches and intimal thickening. Because of these limitations we decided to exclude the heavily calcified bifurcations and very small arteries from our analysis. In the analysis we chose to introduce a scoring system to assign the presence of plaque in predefined parts instead of measuring wall thickness. For calcified plaques, we determined only the densest part of the calcium.

A second limitation is that we included only two types of bifurcations in our study and only of the left coronary tree. We inspected two relatively large bifurcations, which could be easily identified in the MSCT datasets and which are often treated by catheterization. Although we excluded inspection of the complete right coronary artery tree, we do not expect WSS to influence plaque distribution here in a different way [VanDerLaan-04]. Despite the limited resolution of MSCT, we observed a large number (more than one third) of bifurcations that appeared to be trifurcations in our dataset. We excluded these trifurcations because WSS is hard to predict in these geometries. This reduced the number of bifurcations inspected.

A third limitation is that we defined the WSS patterns on the basis of general geometrical features of coronary arteries, being the bifurcation and curvature. Local and patient specific varieties in geometry and/or flow may cause the actual WSS to deviate from the expected WSS distribution. This might explain the single observation of a plaque localized in an expected high WSS region.

We assessed plaque frequency, distribution and morphology near coronary bifurcations with MSCT. Our results are in good agreement with previous findings in IVUS and confirm that in early atherosclerosis, plaques are limited to the low WSS regions and that the plaque distribution is not only influenced by the bifurcation but also by the curvature of the arteries. A new observation is that we showed that the calcified spots in more advanced plaques are mostly located in the low WSS regions. Besides this we presented that circumferential growth of the plaque from the low WSS region into the high WSS regions is a plausible explanation for the presence of plaque in the high WSS sensing flowdivider.

3D fusion of IVUS and CT for in-vivo wall shear stress analysis -a feasibility study-
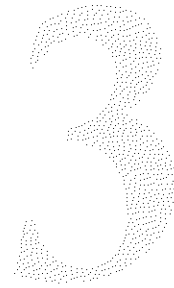
In this chapter a reconstruction technique is presented to obtain 3D patient specific geometries of coronary arteries, that are suitable for wall shear stress (WSS) computations, by the fusion of intravascular ultrasound (IVUS) and coronary computed tomography angiography (CT). From the data of 35 arteries, 31 geometries could be reconstructed. In two reconstructed arteries we showed that despite perturbations in the fusion process the relation between WSS and plaque is maintained. This new framework can therefore successfully be applied for shear stress analysis in human coronary arteries, but also allows side-by-side comparison between IVUS and CT images and contours.

3.1   INTRODUCTION

Although the wall shear stress (WSS), the force per area acting on the lumen wall due to the blood flow, is small compared to the pressure, it is an important biomechanical parameter in the localization and progression of atherosclerosis [Malek-95, VanderLaan-04]. WSS induces processes on cellular and molecular level that influence the atherogenicity of the vessel wall [Slager-05]. It has also been demonstrated that WSS is an important factor in the generation of the vulnerable plaque [Chatzizisis-08] and it has been hypothesized that it plays a role in plaque destabilization [Slager-05]. WSS is thus an important parameter to study in relation to atherosclerosis. Since WSS is hard to measure accurately in the coronary arteries, the WSS is assessed by computational fluid dynamics [Krams-97]. These computations need the 3D geometry of the coronary lumen. To relate the WSS to the atherosclerotic plaque size, also the 3D geometry of the coronary wall is necessary.

Coronary CT angiography is a very promising 3D imaging modality to visualize the coronary arteries, detect significant stenosis [Mollet-05, Mowatt-08] and rule out coronary disease [de Feyter-08]. Some studies already showed that WSS calculations are possible in CT derived geometries [Frauenfelder-07, Suo-08, Rybicki-09]. However, accurate delineation (manually or automatically) of the lumen is still challenging and good discrimination of the vessel wall is even harder[Achenbach-04, Leber-05a, Leber-05b, Pohle-07]. Thus, CT is yet not a suitable stand-alone imaging modality for studying the relation between WSS and atherosclerosis.

The gold standard for coronary lumen and wall information is intravascular ultrasound (IVUS) [Mintz-01]. However, IVUS is a 2D technique that does not provide the 3D information that is required to generate a geometry of the lumen to compute WSS. In this paper we present a framework to fuse the accurate lumen and wall information from IVUS and the 3D information from CT to obtain the 3D geometry of the coronary lumen and wall that can be used as input for the WSS calculations. The fusion of IVUS and CT is validated by comparing the length of IVUS and CT. In addition we demonstrate the robustness of the framework by introducing variations in the fusion procedure and discussing the effect of these variations on the WSS analysis.

3.2 MATERIALS AND METHODS

3.2.1 PATIENTS

We retrospectively included 23 patients who were treated for coronary artery disease in our institution. Patients were included if an IVUS pullback was performed in one or more of the coronary arteries and underwent coronary CT angiography shortly before or after the interventional procedure. Exclusion criteria to perform coronary CT angiography were renal failure, contrast allergy, irregular heart rate, contra-indications to β-blockade and the inability to hold breath for 15 seconds. A single oral dose of 100 mg metoprolol was administered 45 minutes prior to scanning to patients with a heart rate higher than 70 beats per minutes to improve CT image quality [Dewey-07, Ropers-07]. Patients were excluded from this study if they had prior bypass surgery. Arteries that were treated were excluded. All patients gave informed consent and the institutional review board approved the study protocols.

3.2.2 CT ACQUISITION

Scanning was performed on a 64-slice CT scanner (Sensation64®, Siemens, Germany). A detailed description of the patient preparation, scan protocol and image reconstruction has previously been described [Mollet-05]. Briefly, a contrast enhanced scan (Iomeron 400®, Braco, Italy) was performed according to a standardized optimized contrast-enhanced scanning protocol. The initiation of the scan was synchronized to the arrival of contrast in the coronary arteries by a bolus-tracking technique. The images were reconstructed initially during the mid-to-end diastolic phase (350ms prior to the R-wave) with a temporal window of 165 ms. Whenever the image quality was poor, more reconstructions were made at different phases of the cardiac cycle, and the best reconstruction was selected.

3.2.3 IVUS ACQUISITION AND ANALYSIS

During the interventional procedure one or more of the main coronary arteries of the patients were imaged with IVUS. Patients received ≥200 µg of intracoronary nitroglycerine before acquisition. A motorized pullback was performed at 0.5 mm/s with a commercial available 40 MHz IVUS catheter (Atlantis SR Pro, Boston Scientific, Boston, Massachusetts). The pullback was started > 10 mm distal of the segment of interest and ended at the aorta-ostial junction. The images acquired just before systole were extracted from the complete pullback based on an ECG gating method [De Winter-04]. The distance between the extracted images depended on the heart rate of the patient during the pullback and was approximately 0.5 mm. The lumen and external elastic membrane (EEM) contours were semi-automatically delineated on the IVUS images with a validated software package (QIVUS, Medis, Leiden, The Netherlands) according to international standardized guidelines [Mintz-01]. This software package provides a initial segmentation of the lumen and the EEM and allows manual corrections afterwards. The center of the lumen was determined for each cross-section by calculating the center of mass C_i of each lumen contour.

3.2.4 FUSION IVUS AND CT

The goal of the fusion of IVUS and CT was to reconstruct the 3D position and orientation of the IVUS-derived lumen and media contours. We used MeVisLab (Mevis, Bremen, Germany) to build a software tool for the fusion of IVUS and CT and for the visualization.

An IVUS stack encompasses a set of n 2D images $I_{(i \in [1:n])}$. We used the CTA data and corresponding 3D central lumen line to semi-manually determine for each of these 2D images I_i the 3D center of mass of the lumen C_i, the normal of the 3D plane N_i, and a vector pointing in the positive y-direction of the 2D IVUS image U_i. The different steps of the fusion process are explained in detail below.

1. ANNOTATION OF THE CENTRAL LUMEN LINE:

We manually annotated the central lumen line by placing points approximately every 1-2 mm in the center of the artery as determined by the 3 orthogonal views of the CT dataset. The annotation started at the ostium and ended as distally as possible. A curved multi-planar reformat (MPR) image is generated along the centerline to judge the quality of the centerline and, if necessary, to improve it. The centerline markers were smoothed en resampled for each 0.2 mm.
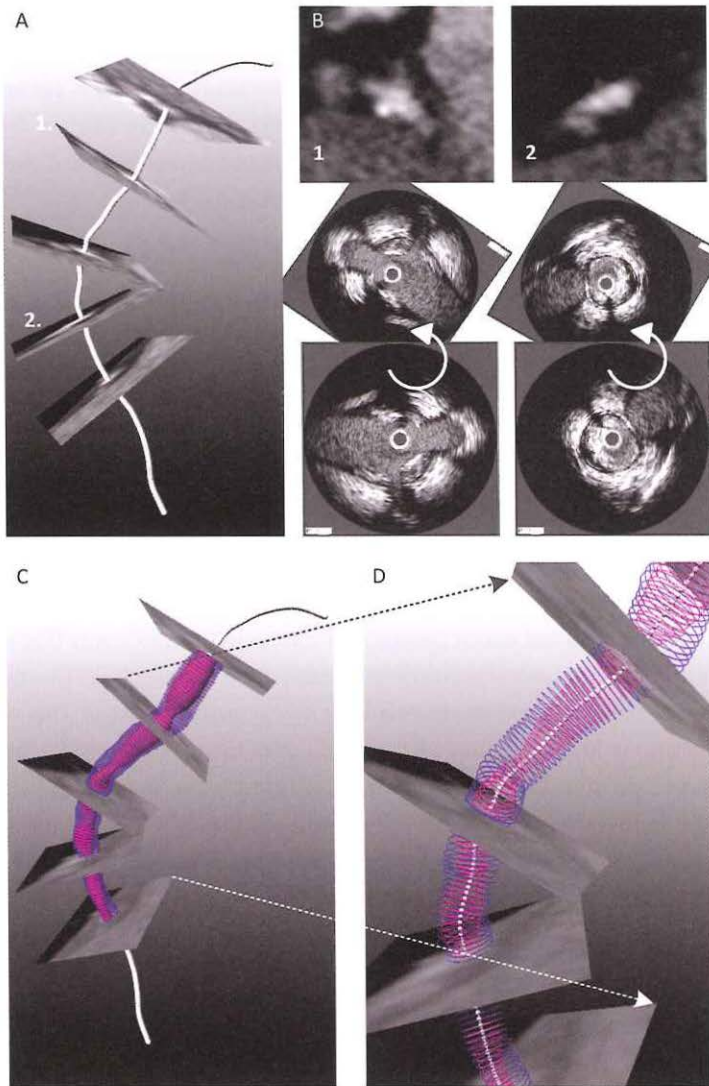
FIGURE 3-1: Panel A shows the centerline of the very diseased artery. Perpendicular to this centerline every 0.2 mm cross-sectional images were generated. In these images we searched for the landmarks that we found on IVUS. The CT images that were matched to the five landmarks found on IVUS are shown in 3 dimensions. In panel B two of the five matched landmarks are depicted: at the top the landmarks in CT and at the bottom the landmarks on IVUS. Rotation is applied to the IVUS images to obtain the correct orientation (middle panel). Panel C shows the IVUS contours placed on the CT derived centerline together with the CT landmarks. A magnification of the 3D contours is shown in panel D.

The smoothed centerline is used in the fusion as follows; the IVUS center of mass C_i is positioned somewhere on the centerline, N_i corresponds to the tangent of the centerline at this respective position, and the orientation vector U_i is perpendicular to N_i. The manual interaction is used to determine the two remaining degrees of freedom for each IVUS image; the 1D centerline position (resulting in C_i and N_i) and the angle of rotation around the centerline (resulting in U_i).

2. MATCHING OF LANDMARKS ON IVUS AND CT

The 1D centerline positions of $C \triangleq \{C_1,..,C_n\}$ were determined in a two-step approach. First we manually defined the positions for a set of landmark IVUS images I_i. As landmarks the bifurcations seen on both IVUS and CT were used. Guided by the distance between the bifurcations in the IVUS image stack and their appearance, we searched in a stack of cross-sectional MPR CT images (Figure 3-1A) for the same bifurcations as were identified on IVUS images. This stack of MPR CT images consists of images generated at every 0.2 mm of and perpendicular to the central lumen line. For each matched bifurcation that was found we selected the image from the IVUS stack which showed the carina of the bifurcation of interest. The image from the MPR CT stack was selected which showed the carina in the same way (Figure 3-1B). The 1D position on the central lumen line of each the matching MPR CT images was assigned to its matched IVUS image resulting in the positions for C_i. This was done for all bifurcations found both in IVUS and CT and for at least 2 bifurcations per artery. The second step is determining the position of the remaining IVUS images between the landmark IVUS images. These were achieved by linear interpolation of the 1D positions of the landmark images. Thus the position of C and the normals $N \triangleq \{N_1,..,N_n\}$ of the IVUS images are now known.

3. DETERMINING ROTATION ANGLE

Using the semi-manually determined positions of C and normals $N \triangleq \{N_1,..,N_n\}$ the software tool reformatted a set of MPR CT images, with each MPR CT image corresponding to one IVUS image.

For each matched bifurcation we then rotated the selected IVUS image around the center of the lumen in such way that the bifurcation had the same orientation as the bifurcation on CT (see Figure 3-1B), resulting in an orientation vector U_i for each landmark image I_i. The orientations of intermediate IVUS images were determined

by spherical linear interpolation (http://portal.acm.org/citation.cfm?doid=325334.325242).The resulting set of 3D IVUS image poses and the associated contours are subsequently used to create the 3D lumen and vessel wall geometry of the coronary artery (see Figure 3-1C-D).

3.2.5   LENGTH VALIDATION

To validate the fusion procedure we compared the length of each fused artery for IVUS and CT. On IVUS the length was calculated by multiplying the number of fused images by the averaged distance in between the images as was calculated during the ECG based extraction of the images. In the CT data, the length of the centerline between the first and last CT landmark was computed.

3.2.6   WALL SHEAR STRESS ANALYSIS

For two coronary arteries we calculated the WSS in the 3D geometries derived from the fusion procedure and related the WSS to the plaque thickness. We selected two extremes from the database; one very diseased artery with significant stenotic areas and calcifications in the artery wall and one mildly diseased artery with only minimal diffused wall thickening without calcifications. From the 3D IVUS contours a lumen and wall surface was generated and smoothed (Laplacian 0.2 smoothing factor, 10 smoothing passes, with boundary and border preservation). The lumen volume was meshed with approximately 800 thousand linear tetrahedral elements with an edge-size of 0.1 mm on the wall (Gambit 2.4.6, Fluent Inc. Products, ANSYS, Inc., USA). The WSS was calculated by simulating a 3D incompressible and laminar flow (FI-DAP 8.7.4, Fluent Inc. Products, ANSYS,Inc. USA). We assumed the blood to be non-Newtonian (Carreau model with time constant = 25 s, power law index = 0.25, zero-viscosity = 0.25 kg/m-s and infinity-viscosity=0.0035 kg/m-s [Seo-05]) with a density of 1050 kg/m^3. We estimated the inlet flow by assuming a WSS of 0.6 Pa [Doriot-00] at the walls and calculated the corresponding inlet flow by Poiseuille's Law. This flow was prescribed at the inlet by a parabolic flow profile. WSS was calculated in a post-processing step using FieldView (FieldView 10F, Intelligent Light, Lyndhurst, USA). For more details on the computational methods we refer to Krams et al. [Krams-97].

The plaque thickness is calculated by determining the shortest distance from the lumen surface to the wall surface (Vascular Modeling Toolbox [www.vmtk.org]). Subsequently the lumen surface is opened along the length of the lumen, and the WSS and plaque thickness values are mapped onto a 2D surface as is shown in Figure 3-5. Each pixel represents 0.5 mm of the arteries length and 10° angle and all values within this pixels are averaged. To obtain the relation between the WSS and the plaque thickness, both the WSS and the plaque thickness are averaged over the length of the artery as was described by Krams et al. [Krams-97] (Matlab 7.1, The MathWorks, Inc., Natick, MA, USA). The WSS-plaque-thickness linear relation can now be determined by regression analysis [Wentzel-05] and is described as:

$$\overline{PT(\phi)} = a \cdot \overline{WSS(\phi)} + b \qquad \text{EQUATION 3-1}$$

, with $\overline{WSS}$, the WSS averaged over the length (Pa), $\overline{PT}$, the plaque thickness averaged over the length (mm), ϕ the radial position and [a] (mm/Pa) and [b] (mm) the regression parameters.

3.2.7 EFFECT OF LANDMARK SELECTION

The 3D reconstruction of the lumen and vessel wall can be influenced by observer dependent choices in the fusion procedure, especially for the selection and rotation of the landmarks; a CT image more proximal or distal can be appointed as match to the landmark IVUS image and also the rotation applied to orient the IVUS images can be user dependent. For both the very diseased and the mildly diseased artery, we varied the matching of the IVUS landmarks to the CT images and the rotation as depicted in Figure 3-2 and we looked into the influence on the WSS and PT analysis.

First we varied the selection of the CT image that is matched to the IVUS image containing the landmark, thus introducing a longitudinal variation. Instead of the original matched CT image, we selected for the second landmark a CT image 2 slices (0.4 mm) more proximal and for the third landmark we selected a CT image, 2 slices more distal to the original matched CT image. Secondly, we varied the rotation angle for the second landmark and third landmark by changing the rotation angle 5° in opposite direction for the second and third landmark. Finally the previous variations in longitudinal and angular direction were combined as a worst case scenario for mismatching. Similarly to the original fusion, for these 3 variations the IVUS contours were placed into 3D, WSS and plaque thickness were calculated

and the WSS-plaque-thickness relation was determined. Subsequently the WSS and plaque thickness of these variations were compared to the original matching on a pixel-to-pixel basis. By Blant-Altman analysis we determined the 95% confidence interval (CI) of the differences between the original and each of the varied fusions. We also identified the location of the maximum plaque thickness and showed how the location of the maximum PT and the WSS at this point is influenced by the variations in matching. The regression parameters of the WSS-plaque-thickness relation were calculated also for the variations and compared to the regression parameters of the original matching.
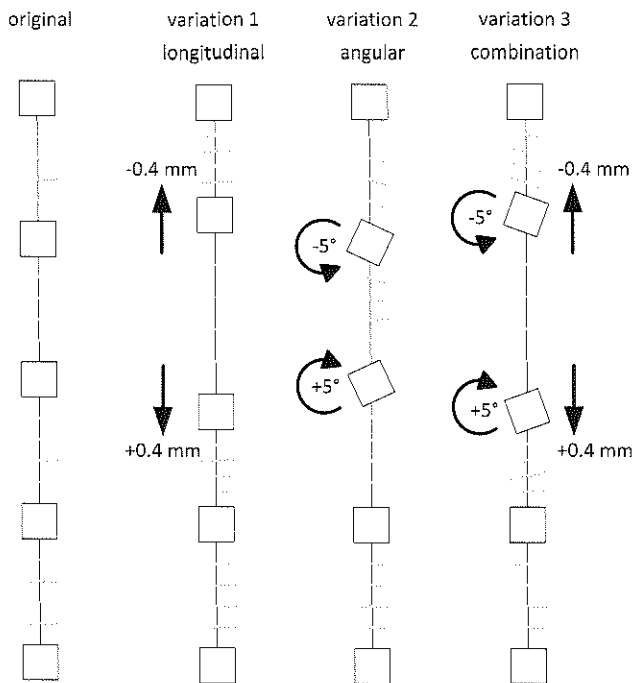
FIGURE 3-2: The squares depict the IVUS landmarks that are matched to the CT landmarks. On the left, the original landmarks for the fusion of IVUS and CT are depicted. We applied 3 variations on the fusion. For the longitudinal variation 1, IVUS landmark 2 is positioned 0.4 mm (2 slices) more proximal on the CT centerline and landmark 3 is positioned 0.4 mm (2 slices) more distal. For angular variation 2, we changed the rotation of the matched IVUS landmark image around the CT centerline. Landmark 2 was rotated 5° counter clockwise and landmark 3 was rotated 5° clockwise. Variation 3 is the combination of the previous two variations. Note how these variations influence the distribution of the IVUS contours between the landmarks.

3.3 RESULTS

3.3.1 FUSION

We included 35 arteries (12 LAD, 13 LCX, 10 RCA) from 23 patients in our study. We were not able to fuse IVUS and MSCT for 4 arteries (3 LCX and 1 RCA) because not enough matching landmarks were found on both IVUS and CT. On average IVUS and CT were fused over a length of 36.4 ± 15.7 mm by 3.7 (2-7) landmarks per artery. The number of landmarks and fusion length was not different for the 3 main coronary arteries (Kruskal-Wallis test, p>0.05).

3.3.2 LENGTH VALIDATION

Regression analysis showed a good linear relationship between the IVUS and CT length with R^2=0.98 (see Figure 3-3A). The averaged length of the fused part was 5.1% longer on CT than on IVUS (36.4 ± 15.7 mm versus 38.2 ± 16.4 mm, paired t-test, p<0.05) with a 95% confidence interval from 17.5% to -7.4% (0.95 mm- 2.66 mm) (see Figure 3-3B). The relative difference in length was not larger for the LCX (9.0%) than for the LAD (3.5%) and RCA (2.8%) (Kruskal-Wallis, p>0.05) (see Figure 3-3C).

3.3.3 WALL SHEAR STRESS ANALYSIS

The fusion of the very diseased artery, an LAD, is visualized in Figure 3-1. This artery was fused with 5 landmarks over a length 54.5 mm with 111 IVUS images. Besides the validation in length also visual inspection of matched IVUS and cross-sectional CT images and the delineation of the IVUS contours on CT as depicted in Figure 3-4 indicate a successful fusion process. Calculations of flow through this diseased artery showed WSS values ranging from 0.3 to 6.0 Pa (mean 1.1 ± 1.0 Pa), see Figure 3-5. The plaque thickness varied over the artery from 0.2 mm to 2.5 mm (mean: 0.9 ± 0.4 mm). WSS peaks were observed at the stenotic sites and coincide with the sites with the largest plaque thickness. The WSS and plaque thickness were positively correlated (R^2=0.77, a=1.5 Pa/mm and b= -0.8 Pa).
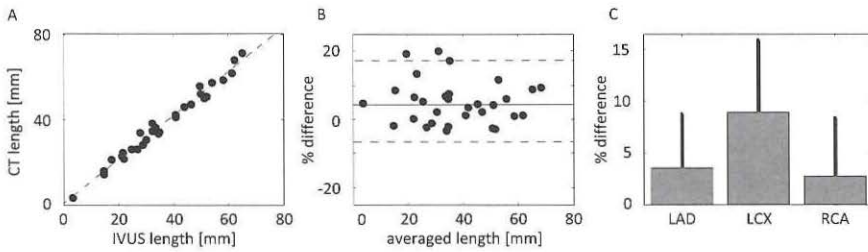
FIGURE 3-3: Panel A. Regression plot; Panel B. Bland-Altman plot; C. Difference per artery. Error bars indicate the standard deviation.
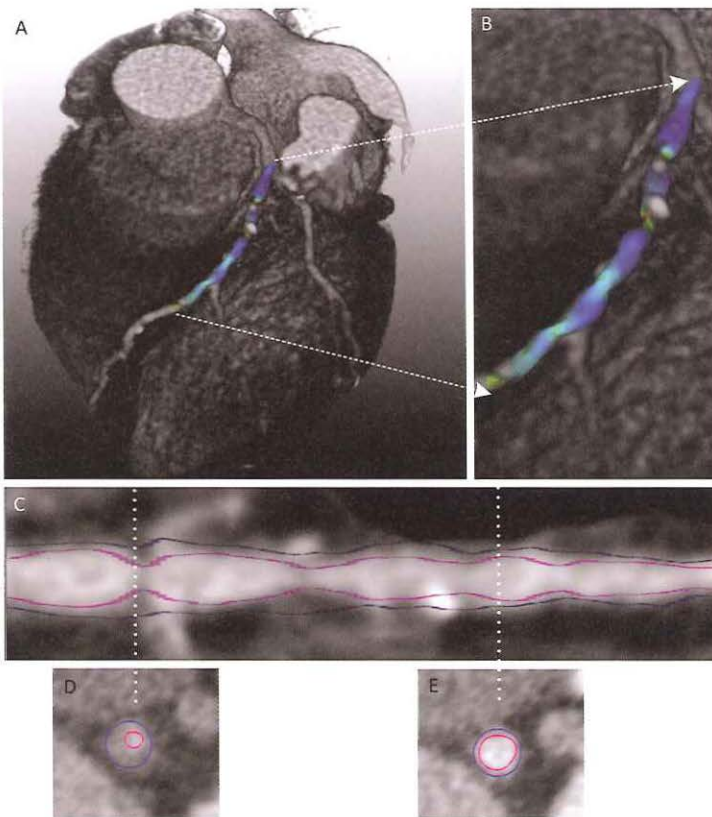
FIGURE 3-4: A: 3D CT dataset of the heart fused with the IVUS derived geometry of the lumen on which the calculated WSS values are depicted. B: Magnification of panel A. C: CT curved multi-planar reformatted image along the centreline of the diseased artery with the fused lumen (pink) and wall (blue) IVUS contours. D and E: Cross-sectional CT images at the indicated locations with the fused lumen (pink) and wall (blue) IVUS contours.
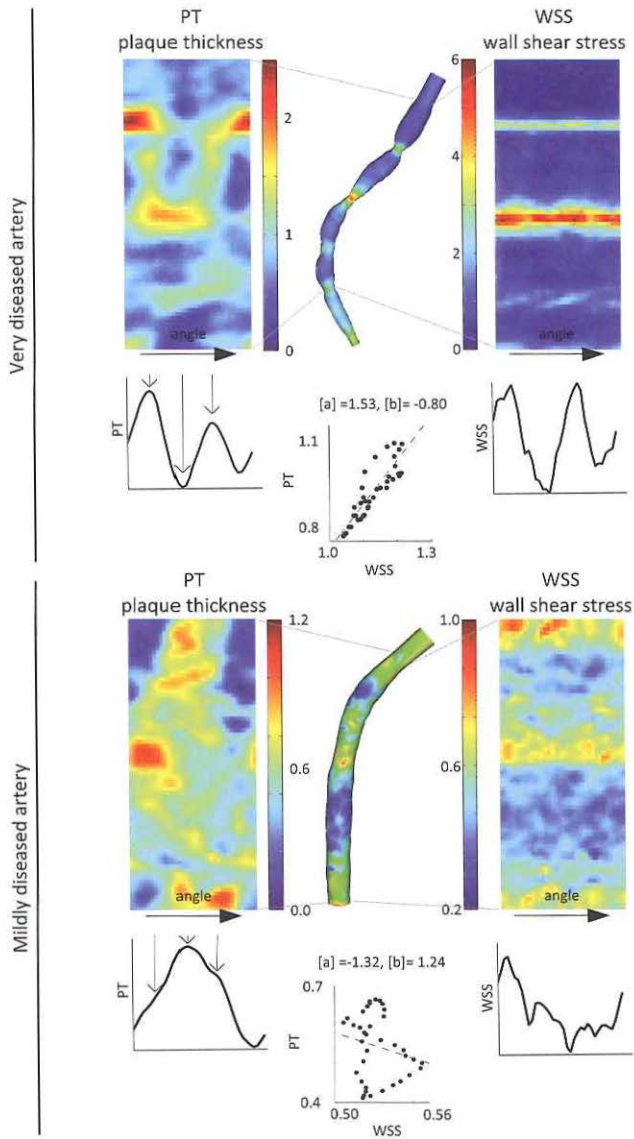
FIGURE 3-5: The wall shear stress (WSS) of the very diseased artery and mildly diseased artery are depicted at the 3D lumen wall in the center. The WSS [Pa] (right image) and plaque thickness (PT) [mm] (left image) can be displayed as a 2D image by virtually cutting open and unfolding the artery along its length. To obtain the WSS-PT-relation, both are averaged over the length of the artery, as can be seen in the left and right panels below the WSS and PT map. These longitudinally averaged values are plotted and by regression analysis the relationship between WSS and PT can be determined, [a] indicates the slope and [b] the off-set.

The mildly diseased RCA was fused over a length of 40.6 mm with 4 landmarks. The plaque thickness ranged from 0.5 ± 0.2 mm (0.1-1.1 mm), which is clearly smaller than for the very diseased artery. The WSS pattern showed no peak values due to stenotic sites as in the diseased artery. The WSS varied between 0.3 Pa and 0.9 Pa (mean 0.5 ± 0.1 Pa). The WSS-plaque-thickness showed no linear relation (R^2 = 0.04, a=-1.3 Pa/mm and b= 1.2 Pa) (see Figure 3-5). All these parameters confirm that this artery is indeed without extensive atherosclerotic disease.

3.3.4   EFFECT OF LANDMARK SELECTION

The WSS patterns for the variations are very similar. The averaged WSS value, as well as the minimum and maximum WSS values do not change due to the variation in landmark selection. The strictest way to evaluate the impact of the variations is comparing the differences on a pixel-to-pixel basis as is depicted for the diseased artery in Figure 3-6. At pixel level we found that 95% of the WSS differences were between -0.45 Pa to +0.40 Pa for the longitudinal variation, between -0.12 Pa to +0.10 Pa for the angular variation and between -0.45 Pa to +0.40 Pa for the combined variation (see also Table 3-1) The Bland-Altman plot to compare the original fusion with the combined variation is depicted in Figure 3-7. The angular variation had no additional influence over the longitudinal variation.

TABLE 3-1: Agreement of WSS and PT of the original fusion versus the varied fusions

	Variation 1		Variation 2		Variation 3	
	R^2	95 % CI	R^2	95 % CI	R^2	95 % CI
Diseased						
Plaque thickness	0.97	-0.13 - 0.12	0.99	-0.05 - 0.06	0.95	-0.14 - 0.14
		-13.2% - 12.7%		-5.8% - 6.0%		-15.6% - 15.5%
Wall shear stress	0.96	-0.45 - 0.40	1.0	-0.12 - 0.10	0.96	-0.45 - 0.40
		-28.0% - 25.0%				-29% - 26.0%
Mildy diseased						
Plaque thickness	0.97	-0.06 - 0.06	0.99	-0.03 - 0.04	0.97	-0.06 - 0.06
		-16.3% - 15.5%		-6.1% - 3.6%		-14.7% - 14.3%
Wall shear stress	0.94	-0.05 - 0.05	0.98	-0.02 - 0.03	0.95	-0.04 - 0.05
		-8.6% - 9.4%		-4.4% - 4.7%		-8.0% - 8.8%

As for the WSS patterns also the plaque thickness patterns look very similar. Also the averaged PT over the complete artery was similar for the original and varied fusions, but, as seen for the WSS, locally the difference can be large, especially near
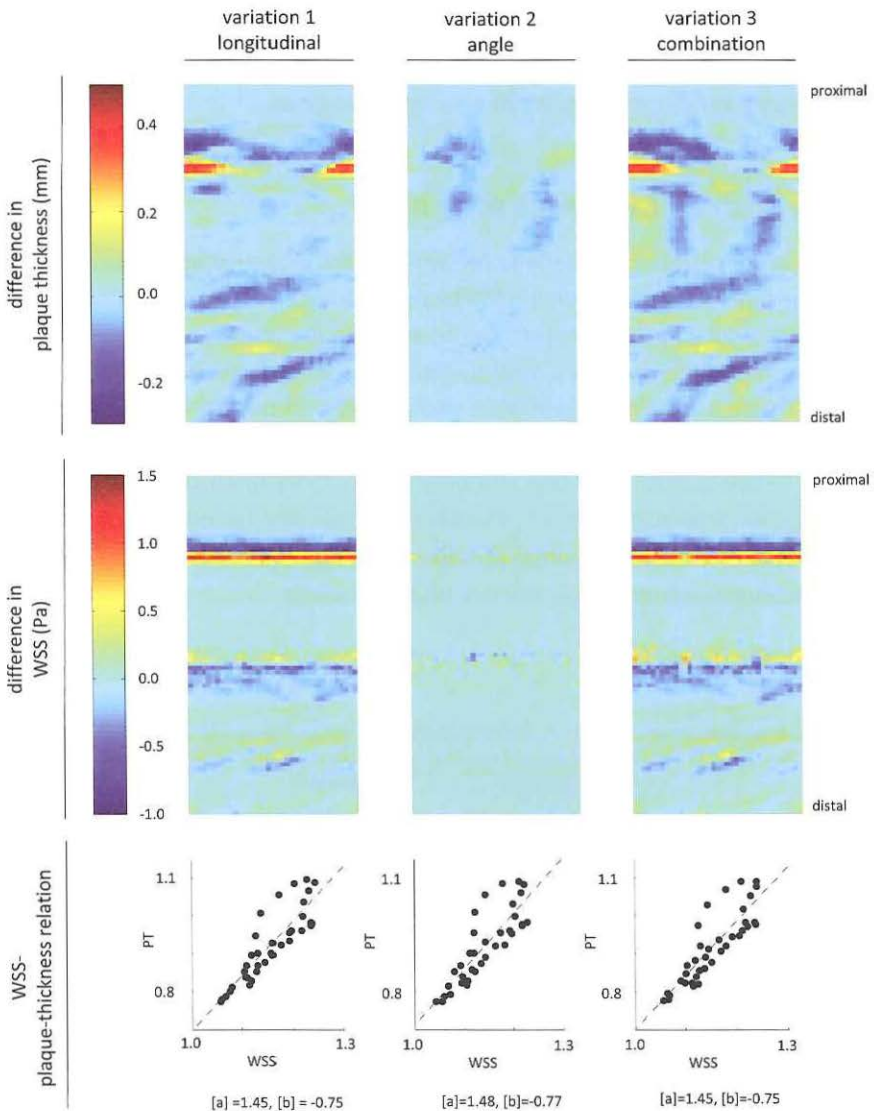
FIGURE 3-6: For the diseased artery the absolute difference for the 3 variations are depicted for the plaque thickness and WSS. Despite some high local differences, the WSS-plaque-thickness-relation is not changed as result of the variations in fusion.

the stenotic sites (Figure 3-6). The plaque thickness differed on a pixel-to-pixel basis between -0.13 to + 0.12 mm (95% CI) due to longitudinal variation, between -0.05 to +0.06 (95% CI) due to the angular variations and between -0.14 to 0.14 mm (95% CI) for the variations combined (see also the Bland-Altman plot in Figure 3-7). Table 3-2 shows that due to the variations, the location of the maximum PT did hardly change, however the WSS was 0.4 Pa or 18%, less for variation 3 at this site.

The WSS-plaque-thickness-relation is hardly influenced by applying variations in the fusion (see Figure 3-6); R^2 was 0.74, 0.71 and 0.76, [a] was 1.4, 1.5 and 1.5 and [b] was -0.7, -0.8 and -0.8 for the longitudinal, angular and combined variations.

In the mildly diseased artery the averaged WSS and plaque thickness patterns were very similar for the original fusion and the variations. Also the averaged WSS and PT values did not change due to any of the variations. The WSS and plaque thickness did change locally, but with lower absolute difference than for the very diseased artery (Figure 3-8). As for the diseased artery the influence of the angular variation was less for both the WSS and plaque thickness. For the combined, most severe variation the WSS differed -0.04 to +0.05 Pa (95% CI). For the plaque thickness the differences were between the -0.06 to + 0.06 mm (95% CI) (see also the Bland-Altman plots in Figure 3-7). Because the WSS and plaque thickness was on average low in the healthy artery the relative changes are large (Table 3-1). However, Table 3-2 shows that the variations have no influence on the location of the

TABLE 3-2: Effect of landmark selection on PT and WSS at maximum PT location

	Maximum PT	Location		WSS
	mm	mm	angle	Pa
Diseased				
Original	2.5	9.0	15	2.2
Variation 1	2.5	8.5	20	1.9
Variation 2	2.5	9.0	20	2.3
Variation3	2.5	8.5	30	1.8
Mildy diseased				
Original	1.1	36.0	265	0.7
Variation 1	1.1	36.0	255	0.7
Variation 2	1.1	36.0	265	0.7
Variation 3	1.1	36.5	255	0.7

PT: plaque thickness, WSS: wall shear stress

maximum PT and the WSS at the maximum PT location. Also for this mildly diseased artery the WSS-plaque-thickness relation did hardly change (R^2 was 0.04, 0.05 and 0.04, [a] was -1.2, -1.6 and -1.3 and [b] was 1.2, 1.4 and 1.2 for the longitudinal, angular and combined variations.

3.4 DISCUSSION AND CONCLUSIONS

In this manuscript a framework to generate 3D coronary lumen and wall geometries by fusion of CT and IVUS data of human coronary arteries is presented for the first time. The results of the current study show that this new accurate and robust method is suitable to study the relationship between WSS and atherosclerosis in clinical studies.
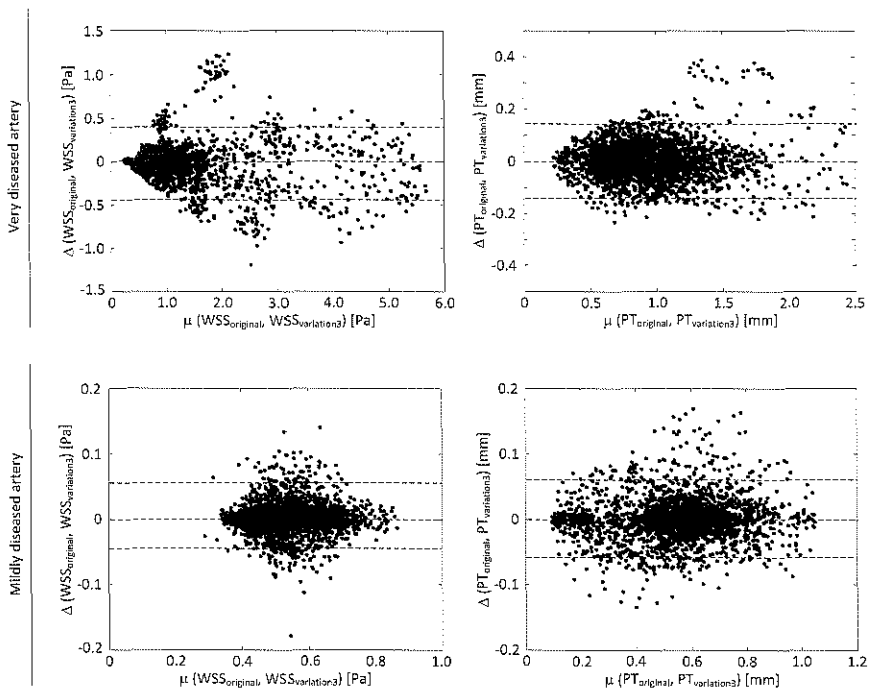
FIGURE 3-7: Bland-Altman analysis of the wall shear stress (WSS) (left column) and plaque thickness (PT) (right column) for the comparison of the combined variation 3 and the original fusion. At the top row the plots are depicted for the very diseased artery, at the bottom row for the mildly diseased artery.

We evaluated the fusion approach by comparing an independent measure: the length of the two matched data sets. The results of this study show an excellent correlation between the two. Furthermore, variation in the selection of landmarks did not influence the patterns or spatially averaged values of WSS and plaque thickness. The method is more sensitive for landmark selection if we compare the results on a pixel-to-pixel basis, especially in severely stenosed arterial segments.

In many clinical studies, the influence of WSS on atherosclerosis was evaluated after applying spatially averaging of the parameters. In these studies, the relationship between WSS and plaque localization [Krams-97], plaque progression [Wentzel-03, Chatzizisis-07], in stent restenosis [Wentzel-01, Stone-03, Wentzel-03]) and plaque composition [Gijsen-08] was established. The results of this paper show that fusion of CT and IVUS is a suitable imaging alternative for these kind of studies. Absolute WSS values should however be regarded with caution since some assumptions, such as discarding the side-branches and the estimation of the inlet flow, could influence them.

The influence of WSS on the vulnerable plaque is less well established, although several reviews were published in which possible mechanisms are presented [Slager-05a, Slager-05b, Chatzizisis-07, Chatzizisis-08]. These mechanisms often involve local phenomena, and application of the current method in these kind of studies might occasionally lead to inaccuracies in WSS determination.
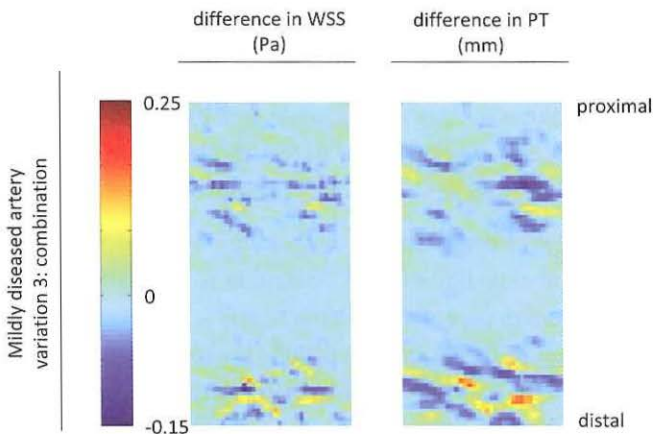
FIGURE 3-8: Effect of variation on wall shear stress (WSS) analysis for the mildly diseased artery. The absolute difference of the combined longitudinal and angular variation is shown for the wall shear stress and the plaque thickness. The color bar is for both the WSS and the plaque thickness.

The other imaging procedure to generate a reliable 3D lumen and vessel wall re-construction relies on the combination of biplane angiography and IVUS. This imaging technique, dubbed ANGUS [Krams-97, Wentzel-01], was validated and used in many clinical investigations relating WSS to plaque thickness. Although the accuracy of the two methods are comparable (centerline reconstruction error in ANGUS approximately 4%, in the current method 5%), there are also some differences. The main advantage of the ANGUS procedure is that the centerline and IVUS imaging are virtually simultaneous, and that the procedure does not rely on the selection and matching of anatomical landmarks. Furthermore, ANGUS does not require an additional (MSCT) imaging procedure. The main disadvantage of the ANGUS is that it requires biplane angiography, which is not readily available, thus limiting the number of patients that can be investigated. Furthermore, it requires a sheath-based IVUS catheter which is not a necessity for the new procedure discussed in this paper. Finally, the current fusion method can be combined with lumen segmentation in the MSCT images, which opens up the possibility to include side branches –and thus coronary bifurcations- in future studies. Since atherosclerosis is often located near the bifurcations [VanDerLaan-04], accurate WSS values at these locations may provide valuable information.

Apart from application of WSS analyses, the current framework opens avenues for many other applications. Since the 3D position and orientation of the IVUS images are known, CT cross-sectional images can be generated at the same location. This allows for slice-by-slice comparison of the IVUS and CT-cross-sectional images in which plaque characteristics can be compared. It is also possible to position the IVUS contours into the CT dataset (Figure 3-4) and by this comparison we might be able to establish guidelines for quantifying lumen and plaque in CT. Once CT derived contours are available, either manually or automatically, the fusion also allows detailed comparison to the IVUS lumen and wall contours.

The current framework could benefit from automation of the several observer dependent steps. At this moment the centerline is manually drawn, but it has been shown that automated centerline extraction is a reliable alternative [Metz-07, Schaap-09]. The selection of the landmarks is done on cross-sectional views and this will be hard to automate. A different approach to match the landmarks for the fusion is proposed by Marquering et al. [Marquering-08]. Instead of matching in a cross-sectional view, they used maximum intensity plots in the longitudinal direction for both IVUS and MSCT and assessed the landmarks in these longitudinal views. Which approach results in the most accurate fusion, is most easy to apply, and most easy to

automate, needs to be investigated. Since the semi-automatic segmentation of the lumen and EEM is the most time consuming part of this technique, it would benefit from validated segmentation algorithms, which to our knowledge are not yet available. Automation of various steps in the procedure has the additional benefit that processing time will reduced considerably.

A second improvement concerns the length of the fused segments. The fused segments are relatively short, on average 36 mm. An IVUS pullback is for safety reasons also limited to a relative small part of the coronary tree. Since small side-branches are often not visible on CT, we rely on the large side-branches but at least 2 landmarks are necessary for the fusion procedure. Short IVUS segments therefore hinder the fusion over long parts. A third improvement concerns the extraction of the IVUS images from the complete pull-back. Ideally the images would be extracted in the same time-frame of the heart beat as the reconstruction of the CT images. In our method the IVUS images are extracted at end-diastole, while the CT is reconstructed during mid-diastole. However the influence on the reconstruction is expected to be small, since the movement of the arteries during this cardiac phase are small. The short fused segments, in combination with the invasive nature of IVUS and the accompanying high costs, limit the wide assessment of the WSS influence on the atherosclerosis. Overall, it would be a step forward if CT could be used stand-alone to obtain lumen and wall information for WSS analysis. Since the resolution of CT is still improving and automated segmentation algorithms are under development and under validation, WSS analysis in relation to risk prediction might be possible by using solely CT as imaging modality.

In conclusion, the presented framework in which human coronary IVUS and CT are fused, can be used to derive 3D lumen and wall geometries in which the relationship between WSS and atherosclerosis can be investigated. Moreover the framework opens avenues for validation of coronary CT segmentation algorithms.

Accuracy of coronary plaque detection by CT angiography: ex-vivo comparison to IVUS

In this chapter the fusion technique, as presented in the previous chapter, is used to co-register cross-sectional intravascular ultrasound (IVUS) and computed tomography (CT) angiography images from 10 ex-vivo human coronary arteries. Atherosclerosis presence and composition were determined by independent readers to assess the reader agreement and the diagnostic accuracy of CT. Quantitative measures on IVUS were used to determine predictors for the detection of non-calcified plaques. In total 1002 cross-sectional images were scored. The reader agreement and accuracy for plaque detection varied with plaque composition. The plaque thickness was an independent predictor for the detection of non-calcified plaques. Only non-calcified plaques with a plaque thickness larger than 1 mm could reliably be detected.

4.1   INTRODUCTION

Computed tomography angiography (CTA) of the coronary arteries has excellent sensitivity and good specificity for the detection of coronary artery stenosis when compared to invasive coronary angiography [Mollet-05, Hoffmann-06, Meijboom-06, Pugliese-06, Leber-07, Mowatt-08]. In addition, coronary CTA provides noninvasive characterization of coronary atherosclerotic plaque, which may be helpful to improve risk stratification [Leber-05]. While CTA is highly accurate for the detection of calcified plaque [Schmermund-97, Knez-02] various studies have demonstrated the feasibility to detect non-calcified plaque [Leber-03]. These limitations are linked to the difficulty to establish the outer boundary of non-calcified plaques as their density is close to that of the surrounding myocardial or pericardial tissue and the blooming effect of contrast enhanced blood. Overall, more reliable detection appears to be limited to larger non-calcified plaques within the proximal coronary arteries [Leber-05, Iriart-07, Motoyama-07, Pohle-07].

The purpose of this ex-vivo study was to define the accuracy of CTA in atherosclerotic plaque detection and to determine predictors for CTA plaque detection using IVUS plaque quantification as the gold standard.

4.2   MATERIALS AND METHODS

4.2.1   EX-VIVO CORONARY ARTERIES

Six ex-vivo human hearts were studied (International Institute for Advancement of Medicine, Phoenix, AZ, USA). Selection criteria included subjects with traditional risk factors for coronary artery disease aged between 50 and 70 years that had died from a non-cardiac cause. Subjects with known coronary artery disease, prior coronary artery revascularization or cardiac death were excluded. The three major coronary arteries together with the surrounding pericardial and myocardial tissue were excised and flushed with saline to remove superficial thrombus. Luer tapers made of radiation stable polycarbonate material were inserted into the proximal and distal lumen of each artery to enable a leak-free infusion of contrast agent. The side-branches were ligatured. Typically, the proximal 50 mm of each coronary was salvaged. The arteries were placed in a custom tailored plastic vessel box for stability (Modern Plastics Inc, Bridgeport, Connecticut, USA). The proximal luer was then

connected to a circuit which facilitated the infusion of phosphate buffered saline or iodinated contrast at a constant pressure (150 mmHg). The vessels were shipped fresh and all imaging experiments were completed within 72 hours of the vessel harvest. The study was approved by the Massachusetts General Hospital institutional review board.

4.2.2 IMAGE ACQUISITION

DUAL SOURCE COMPUTED TOMOGRAPHY

CT imaging of each coronary artery was performed on a 64-slice dual source system (CT, Somatom Definition, Siemens Medical Solutions, Forcheim, Germany). In preparation for imaging, the vessel box was connected to a cardiac motion simulator that recreates the oscillation and velocity of the coronary arteries at pre specified heart beats. This technique has previously been described [Achenbach-00, Reimann-07]. The motion simulator was synchronized to an electrocardiographic signal generator which facilitated electrocardiographic gating of the CT data. The heart rate frequency selected for this study was 70 beats per minute. The vessel box was then positioned in the center of a semi-anthropomorphic thorax phantom (QRM, Moehrendorf, Germany), such that movement was along the z-direction of the CT scanner. The apparatus was finally placed in a specially constructed plastic tank which contained pH optimized phosphate-buffered saline.

Data were acquired using a standardized cardiac spiral imaging protocol with a tube voltage of 120 kV, exposure of 360 mAs, slice collimation of 0.6 mm, and a rotation time of 330 ms). Images were reconstructed at a 17 cm field of view, at 0.4 mm increments, and a soft cardiac kernel (B26f) during the best diastolic phase as chosen by the software. This results in voxel size of 0.33 mm in-plane and 0.4 mm in z-direction. The coronary arteries were flushed with a mixture of saline solution (0.9% w/v sodium chloride) containing 3% v/v contrast agent (Contrast Isovue 370, Bracco Diagnostics Inc, Princeton, New York, USA), which provided an intraluminal contrast attenuation of 250 HU [Nikolaou-04].

INTRAVASCULAR ULTRASOUND

Intravascular ultrasound was performed in a pressure-perfusion system filled with phosphate-buffered saline using a 40 MHz IVUS catheter (Galaxy, Boston Scientific, Boston, Massachusetts, USA) and motorized pullback (0.5 mm/s, 30 frames/s, from distal to proximal). The resulting image rate was retrospectively reduced to one image every 0.2 mm. This image rate was used for further analysis. Images were digitized and stored for analysis on an offline workstation.

4.2.3 CROSS-REGISTRATION BETWEEN CT AND IVUS

We used in-house developed software (based on the visualization and imaging software MeVisLab, Mevis, Bremen, Germany) to manually register and analyse IVUS and CT datasets at every 0.4 mm along the artery.

The registration process was performed as follows: The IVUS image stack was post-processed and reduced so that only images separated by an axial distance of 0.2 mm were selected for analysis (Figure 4-1a). In this IVUS stack landmarks such as the proximal and distal luers, bifurcations and side branches were identified to facilitate cross-registration with the CT data set (Figure 4-1b and c). Cross sectional CT images were precisely registered with the IVUS stack by the generation of axial images every 0.2 mm from a curved multiplanar image format (Figure 4-1d). Due to the artificial elongation of the vessel by the IVUS guide wire a further CT image stack was generated h that precisely aligned the CT images and the IVUS images between the reference landmarks (Figure 4-1e). At least two landmarks had to be identified on both imaging modalities. As a result we obtained a corresponding CT image for each IVUS image between the most proximal and most distal landmark with a longitudinal spacing of 0.2 mm. This enabled an exact comparison between the data sets. For this analysis every second image from both data sets was used (0.4 mm spatial separation).

| a. IVUS stack | b. IVUS landmarks | c. CT landmarks | d. CT centerline |

a. IVUS stack   e. CT resampled stack
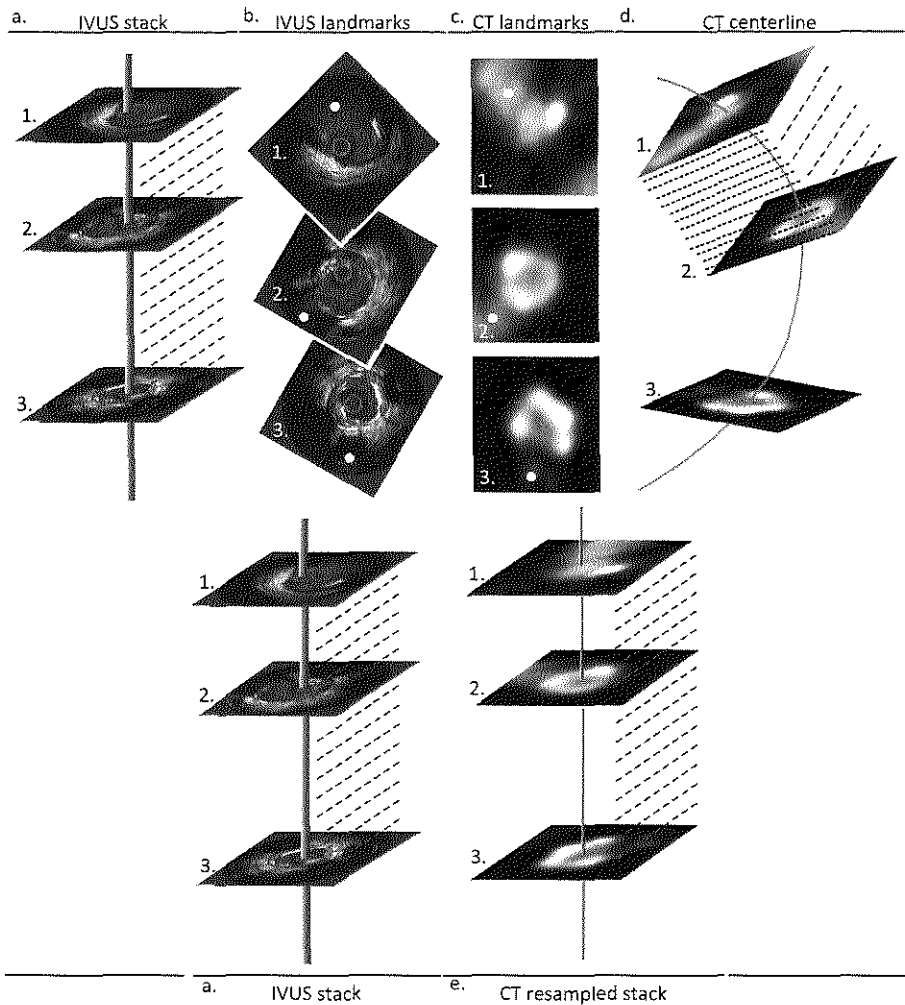
FIGURE 4-1: In the IVUS stack (a) 3 bifurcations (1 to 3) serve as landmarks (indicated by the dots in (b)) for the registration. In the MSCT scan the centerline is tracked through the artery and cross-sectional images are reconstructed (black dotted lines). The three bifurcations in the IVUS stack are identified in the MSCT cross-sections (c). The MSCT data is resampled between the landmarks such that the number of images between landmarks is equal to the number of images in the IVUS stack (e).

4.2.4   IMAGE ANALYSIS

DUAL-SOURCE COMPUTED TOMOGRAPHY

Guided by a longitudinal view of the artery, each cross sectional image was assessed for the presence of any plaque and non-calcified, mixed or calcified plaque using a fixed window setting (500 HU width, 200 HU level) [Ferencik-06]. Non-calcified plaque was defined as any clearly discernible structure that could be assigned to the coronary artery wall in at least two independent image planes and had a CT density less than 130 HU but greater than the surrounding connective tissue. Calcified atherosclerotic plaque was defined as any structure within the coronary artery wall with a density of 130 HU or more that could be separated from the contrast-enhanced coronary lumen. Mixed coronary atherosclerotic plaque was defined as the presence of non-calcified and calcified constituents within a plaque. This approach has previously been validated [Leber-03, Achenbach-04, Hoffmann-06].

Analyses were independently performed by two observers. In case of disagreement on plaque presence or composition a third observer performed an independent adjudication reading, which was used for further analysis. In addition one observer analysed the data a second time one week after the first readings to obtain intra-observer variability. All observers were blinded to the IVUS images and results.

INTRAVASCULAR ULTRASOUND

Lumen and external elastic membrane (EEM) contours were manually drawn [Mintz-01] for each cross-section by one observer. These contours were exported to Matlab (version 7.1, The MathWorks, Inc., Natick, MA, USA) and lumen area, vessel area, plaque area, maximum and mean intimal thickness and eccentricity were determined. Plaque area was defined as vessel area (inside the EEM) minus the lumen area. Eccentricity was defined as the maximum plaque thickness divided by the minimum plaque thickness.

We classified on IVUS four types of cross-sections, those without plaque, with non-calcified plaque, with mixed plaque and with calcified plaque. A cross-section was considered without plaque when the intimal thickness was less than 0.5 mm [Clarijs-97, Tuzcu-01] for at least 90% of the lumen contour. Cross-sections with plaque were classified as calcified when the arc of calcification subtended greater than 90° of the cross-section as measured from the center of the lumen. A mixed plaque

was defined as an arc of calcium less than 90°. Cross-sections with plaque, but without calcifications were classified as non-calcified. Presence, composition and quantitative plaque characteristics as determined by IVUS were considered the gold standard.

4.2.5 STATISTICS

To determine the agreement between the observers on the detection of different kind of plaques on CT, we reported the inter- and intra-observer variability by means of the non weighted Cohen's Kappa statistic. The CT adjudications reading and IVUS readings were used to compose a 4x4 contingency table of the cross-sectional classifications. From this table the contingency coefficient was calculated as a measure of the association between IVUS and CT (0 for no association and 1 for complete agreement). From the 4x4 table, 2x2 tables were extracted to determine the sensitivity (Sens), specificity (Spec), negative predictive value (NPV), positive predictive value (PPV), prevalence (Prev) and accuracy (Acc) for the detection of any plaque and for the different plaque types.

Next we performed a more detailed analysis for the subgroup of non-calcified plaque. We determined differences for quantitative IVUS characteristics such as lumen area, EEM area, plaque area, mean intimal thickness, maximum intimal thickness and eccentricity between non-calcified plaque detected and not detected in CT using the non-parametric Mann-Whitney test. We then performed univariate logistic regression to determine the odds for detecting non-calcified plaques in CT with change in IVUS based plaque characteristics. A multivariate logistic regression model with conditional forward selection was used to determine independent predictors for the detection of non-calcified plaques on CT. Lastly, we constructed Receiver Operating Characteristics (ROC) curves for plaque measures as a function of the diagnostic accuracy to determine the ability to discriminate between true positive and false negative findings.

Cohen's Kappa, sensitivities, specificities, NPV, PPV, prevalence, and contingency coefficient are reported by their means with 95% percentile intervals as calculated by bootstrapping the data (10 000 times). The IVUS measures are reported with bootstrapped mean and standard deviation. For the univariate and multivariate regression the Odds ratios (OR) with 95% confidence (CI) and p-values are reported. The ROC analysis is reported by the area under the curve (AUC) values with 95% CI.

We performed the statistical analysis with SPPS 16.01 (SPSS Inc., Chicago, Illinois) and the Statistics Toolbox of Matlab (version 7.1, The MathWorks, Inc., Natick, MA, USA) and p-values <0.05 were considered statistically significant.

4.3   RESULTS

Ten coronary arteries (5 LAD's, 1 LCX and 4 RCA's) were harvested from 6 patients (5 female and 1 male). Eight arteries could not be prepared for imaging because they were too small (1 LAD, 5 LCX, 2 RCA). The patients had at least 2 or more risk factors for coronary artery disease. The patient characteristics are depicted in Table 4-1. In total, 1002 IVUS and CT cross-sectional images were registered, equal to 40 mm per artery.

4.3.1   INTER- AND INTRA-OBSERVER VARIABILITY

The intra-observer variability for the detection of any type of plaque was good (K=0.76, 95% CI: 0.73-0.79) and the inter-observer variability was moderate (K=0.52, 95% CI: 0.47-0.56). Adjudication was necessary for 298 cross-sections (30%). Intra and inter-observer variability were strongly associated with presence and composition of plaque as detected by IVUS. Inter- and intra-observer variability was low

TABLE 4-1: Subject characteristics

Subjects						
	1	2	3	4	5	6
Gender	Female	Female	Female	Female	Male	Female
Age (years)	61	61	64	59	57	69
Cause of death	SAH	SAH	ICH	RA	RA	RA
Obesity	x	x		x	x	x
Diabetes				x		x
Hypertension		x	x	x	x	
Smoker		x	x		x	
Hyperlipidemia	x			x		x
Known VD					x	

VD: Vascular disease, SAH: subarachnoid hemorrhage, ICH: intracranial hemorrhage, RA: respiratory arrest. Hypertension is defined as >140 mmHg, obesity is defined as BMI >30 kg/m².

(K=0.23 and K=0.50) for cross-sections without plaque on IVUS (n=223), excellent (K=1.00) for cross-sections with calcified plaque, and intermediate for those cross-section with non-calcified (K=0.48 and K=0.76) and mixed plaque (K=0.42 and K=0.56) (see Table 4-2).

TABLE 4-2: Inter- and intra observer variability for the detection of plaque by CT

	n	Inter-observer Kappa (95% CI)	Intra-observer Kappa (95% CI)
Overall	1002	0.52 (0.47-0.56)	0.76 (0.73-0.79)
Stratified by presence of plaque as determined by IVUS			
Plaque	779	0.53 (0.48-0.58)	0.78 (0.74-0.81)
No plaque	223	0.23 (0.14-0.32)	0.50 (0.386-0.61)
Stratified by plaque composition as determined by IVUS			
Non-calcified	585	0.48 (0.42-0.53)	0.76 (0.71-0.80)
Mixed	162	0.42 (0.21-0.61)	0.56 (0.38-0.72)
Calcified	32	1.00 (-)	1.00 (-)

n = number of cross-sections; CI =confidence interval; IVUS = intravascular ultrasound
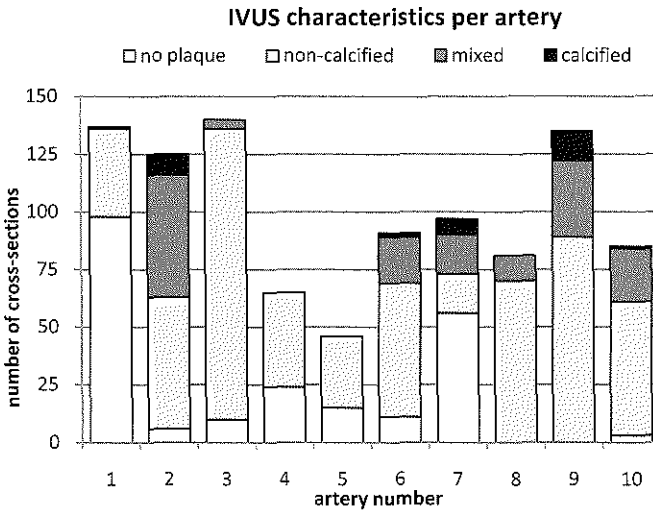
FIGURE 4-2: The presence and composition of the atherosclerotic plaque of each coronary artery as defined by IVUS expressed as the number of cross-sections included in the analysis.

4.3.2 THE ACCURACY TO DETECT AND CLASSIFY PLAQUE ON CT

INTRAVASCULAR ULTRASOUND

Coronary atherosclerotic plaque (intimal thickness $\geq$ 0.5 mm) was detected by IVUS on 779 (78%) of the 1002 cross-sections. Non-calcified plaque (59%, 585 cross-sections) was more frequently found than mixed plaque (16%, 162 cross-sections) or calcified plaque (3%, 32 cross-sections) ($p < 0.001$). Figure 4-2 demonstrates the prevalence and plaque composition across the analysed vessels. The prevalence varies from 28-100% and consistently non-calcified plaque was most frequently detected followed by mixed and calcified plaque.

DUAL SOURCE COMPUTED TOMOGRAPHY

Any plaque: Of the 779 cross sections in which plaque was detected by IVUS, CT demonstrated plaque in 592 cross sections (sensitivity: 76% (73%-78%) sensitivity). Of the 223 cross-sections without plaque on IVUS only 19 (9%) cross-sections were thought to contain plaque on CT resulting in an excellent specificity of 91% (88%-95%). Similarly the PPV was excellent with 97% while the NPV was poor with 52% as 187 cross sections contained plaque by IVUS but not by CT. Figure 4-3 shows 4 examples of matched cross-sections in whom CT accurately identified the absence of plaque, and the presence of non-calcified plaque, mixed plaque or calcified plaque.
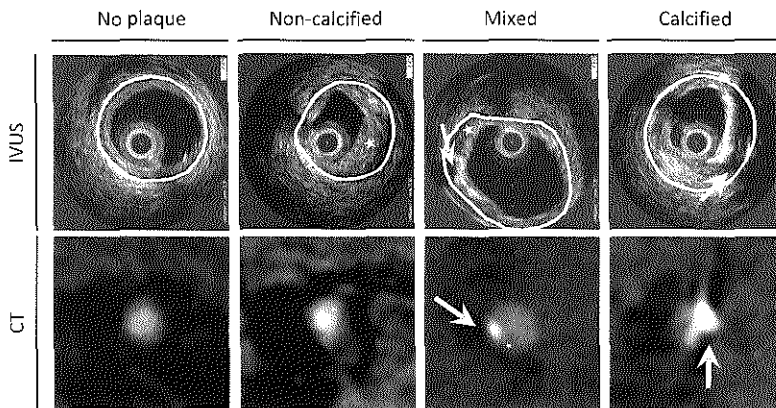
FIGURE 4-3: Example of co-registered Intravascular Ultrasound (IVUS) and Dual-Source Computed Tomography (CT) images for absence of plaque, and for presence of non-calcified, mixed and calcified plaque. The arrows indicate calcium and the stars (*) are placed in the non-calcified part of the plaque

Plaque composition: Table 4-3 demonstrates that misclassification by CT occurred most often in plaques classified as mixed or non-calcified by IVUS (67.9% and 42.6%; respectively). The contingency coefficient was 0.63 (95% CI: 0.61-0.66). Misclassification was rare in cross sections containing no or calcified plaque but frequent in smaller non-calcified plaques (no detection- poor sensitivity), non-calcified cross-sections adjacent to calcified cross-sections (blooming of calcification - misclassification of non-calcified as mixed plaques and of mixed plaques as calcified). Figure 4-4 demonstrates these misclassifications.

TABLE 4-3: Classification of plaque presence and composition on CT compared to IVUS

		IVUS Characteristics				
		No plaque	Non calcified	Mixed	Calcified	Total
CT Characteristics	No plaque	**204**	181	6	0	391
	Non calcified	10	**336**	54	1	401
	Mixed	7	51	**52**	13	123
	Calcified	2	17	50	**18**	87
	Total	223	585	162	32	1002

Numbers of cross-sections are given. IVUS=Intravascular ultrasound; CT=Computed tomography

The sensitivity of CT for correct plaque recognition was dependent on plaque composition (Table 4-4). The sensitivity to detect non-calcified plaque was 57% (54%-61%). The sensitivity to classify mixed plaque was very low with 32% (26%-38%) but the sensitivity to detect any calcification was 69% (63%-74%) (including both mixed and calcified plaque). In contrast, the specificity was high for all plaque types: 84%

TABLE 4-4: Diagnostic accuracy of CT to detect and classify plaque

	Plaque Type			
	Any	Non-calcified	Mixed	Calcified
Sensitivity	76% (73-78)	57% (54-61)	32% (26-38)	56% (41-71)
Specificity	91% (88-95)	84% (81-87)	92% (90-93)	93% (92-94)
Negative predictive value	52% (48-56)	58% (55-62)	87% (86-89)	98% (98-99)
Positive predictive value	97% (96-98)	84% (81-87)	42% (35-50)	21% (14-28)
Accuracy	79% (77-82)	69% (66-72)	82% (80-84)	92% (90-93)
Prevalance	78% (76-80)	58% (56-61)	16% (14-18)	3% (2-4)

In between the brackets the 95% confidence interval is given
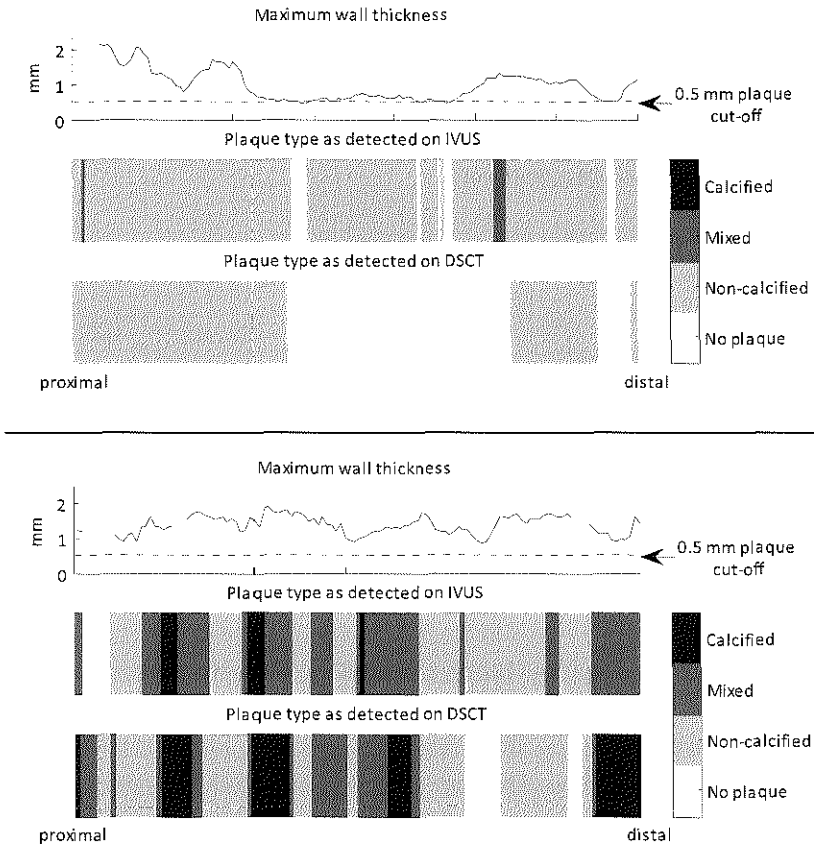
FIGURE 4-4: Maximum intimal thickness and plaque composition by IVUS and CT. We demonstrate maximum intimal thickness as measured by Intravascular Ultrasound (IVUS), and co-registered presence and plaque type as detected on IVUS and Dual-Source Computed Tomography (CT). The dotted line in the upper graph indicates 0.5 mm intimal thickness, above which it is considered atherosclerotic plaque. The upper panel illustrates one artery in which we demonstrate the association of intimal thickness with the ability of CT to detect non-calcified plaque. While proximal and distal cross sections with a maximum intimal thickness that largely extends the 0.5 mm are detected by CT, plaque in the mid section of the artery may be missed by CT because the maximum intimal thickness barely exceeds 0.5 mm. The bottom panel illustrates a second aretry in which the calcified plaque is overestimated by CT leading to misclassification of mixed plaque (as detected by IVUS) as calcified plaque.

(81%-87%), 92% (90%-93%) and 93% (92%-94%) for non-calcified, mixed, and calci-
fied plaques. The accuracy to classify plaque correctly increased from non-calcified
(69%, 66%-72%) to mixed (82%, 80%-84%) to calcified plaque (92%, 90%-93%).

4.3.3 PREDICTION OF NON-CALCIFIED PLAQUE DETECTION BY DCST

Table 4-5 provides the IVUS based plaque characteristics (lumen area, vessel area,
plaque area, mean intimal thickness, maximal intimal thickness, and plaque eccen-
tricity) within two groups: cross sections that were identified as non-calcified plaque
on both IVUS and CT (True positive CT finding: N=336) and cross sections that were
identified as non-calcified plaque on IVUS but as normal on CT (False negative CT
finding: N=181). IVUS cross-sections with plaque missed by CT had significantly larg-
er lumen area and smaller vessel area, plaque area, mean intimal thickness, maxi-
mal intimal thickness and lower eccentricity than cross-sections with true positive
CT findings ($p<0.05$ for all) (Table 4-6). For example, the odds of detecting non-calci-
fied plaque in CT increased by 226% with every 0.1 mm increase in intimal thickness
as measured by IVUS. The ROC analysis demonstrates that AUC for prediction of
detecting non-calcified plaque on CT was largest for the maximum intimal thickness
(0.86, 95% CI: 0.83-0.90) and smallest for the wall area (0.55, 95% CI: 0.50-0.61).

In multivariate analysis, lumen area (OR=0.88 per mm, 95% CI: 0.82-0.95 , p=0.001)
and maximum intimal thickness (OR=1.56 per 0.1 mm, 95% CI: 1.47-1.77, p<0.001)
were the only independent predictors (see Table 4-6) and the odds of detecting

TABLE 4-5: Comparison of IVUS measures for non-calcified plaques detected and missed

	True positives	False negatives	p-value
Plaque type by IVUS	Non-calcified	Non-calcified	
Plaque type by CT	Non-calcified	No plaque	
N	336	181	
Lumen area (mm²)	8.3±4.0	9.4±3.7	<0.001
Vessel area (mm²)	17.6±7.9	15.2±5.1	0.045
Plaque area (mm²)	9.3±4.7	5.8±1.8	<0.001
Mean intimal thickness (mm)	0.73±0.25	0.47±0.11	<0.001
Maximum intimal thickness (mm)	1.36±0.50	0.78±0.21	<0.001
Eccentricity	4.4±2.1	3.1±1.6	<0.001

Means and standard deviation are given

TABLE 4-6: Results of binary logistic regressions

Predictor	Unit	Uni-variate analysis		Multi-variate analysis	
		OR /unit	p-value	OR/unit	p-value
Lumen area	mm²	0.93 (0.87-0.98)	0.003	0.88 (0.82-0.95)	0.001
Vessel area	mm²	1.05 (1.02-1.09)	< 0.001		0.104
Plaque area	mm²	1.43 (1.30-1.57)	< 0.001		0.104
Mean intimal thickness	0.1 mm	2.26 (1.91-2.68)	< 0.001		0.292
Maximum intimal thickness	0.1 mm	1.61 (1.47-1.77)	< 0.001	1.56 (1.47-1.77)	< 0.001
Eccentricity		1.54 (1.35-1.77)	< 0.001		0.216

In between the brackets the 95% confidence interval is given

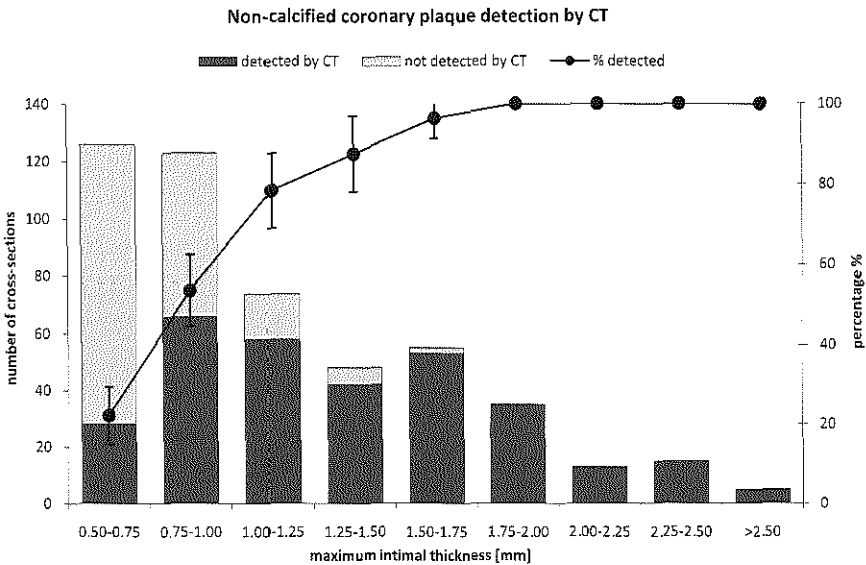**Non-calcified coronary plaque detection by CT**

FIGURE 4-5: Relation between maximal intimal thickness and detection of non-calcified plaque. The sensitivity of Dual-Source Computed Tomography (CT) to detect non-calcified plaque increases with the intimal thickness. Notably, sensitivity reaches 80% or more at a maximal intimal thickness of 1 mm.

non-calcified plaque in CT increased by 56% (95% CI: 47%-77%) with every 0.1 mm increase in maximum intimal thickness as measured by IVUS.

4.3.4 ACCURACY OF NON-CALCIFIED PLAQUE DETECTION BY DCST

Figure 4-5 demonstrates the increase in detection rate with strata of increasing intimal thickness, i.e. 80% sensitivity corresponds to 0.78 mm intimal thickness. Non-calcified plaques with a small intimal thickness (>0.50 mm ≤ 0.75 mm) were frequent present (26%), but had a low detection rate (22%), while as the intimal thickness increased also the detection rate increased to 54% for >0.75 ≤1.00 mm, 78% for >1.00 ≤1.25 mm, 89% for >1.25 ≤1.50 mm, 96% for >1.50 ≤1.75 mm, and 100% for >0.75 mm. Because 50% of the non-calcified plaques (n=249/494) had an intimal thickness ≤ 1.00 mm, a considerable amount of the non-calcified plaques was missed by CT (n=179/494, 36%). However, the detection rate for plaques >1 mm thickness was excellent (n=221/245, 90%).

4.4 DISCUSSION

This ex-vivo study demonstrates a good overall intra- and interobserver variability and accuracy of CT for the detection and classification of coronary atherosclerotic plaque as compared to IVUS using a rigorous and novel methodology for the cross-registration of IVUS and CTA image stacks. We also demonstrate that the ability of CT to detect plaque significantly varies with plaque composition and that significant misclassification of mixed plaque as calcified plaque and of non-calcified plaque as mixed plaque occurs.

We further demonstrate that plaque thickness and lumen area as measured by IVUS are independent predictors of the accuracy of CT to detect non-calcified plaque. Moreover, we demonstrate that detection rates increase from 36% for non-calcified plaques <1 mm intimal thickness to 90% for plaques with >1 mm thickness. Overall, these data provide detailed knowledge on the association of CT assessment of plaque in relation to the clinical gold standard IVUS and establish 1 mm as an excellent detection threshold.

Compared to the assessment of stenosis, relatively few studies have assessed the feasibility of CTA to detect and characterize coronary atherosclerotic plaque. Normal intima of the coronary arteries (intimal thickness: 0.15 ± 0.07 mm in healthy adults <50 years of age, intimal thickening by IVUS defined as <0.5 mm [Nissen-01]) cannot be assessed due to limited spatial CT resolution by CT. However, the reported characteristics of high risk plaques such as proximal coronary artery location, thin fibrous cap atheroma with a necrotic core: 2-17 mm in length, median 8 mm [Virmani-06], with lipid pools and core of 1-5 mm^2 and >1.0 mm^2, respectively ([Virmani-02, Virmani-06]), make cardiac CT a potential candidate for noninvasive detection and characterization of such plaques.

Presently available clinical data suggest a high overall accuracy of CTA to detect coronary atherosclerotic plaque in comparison to IVUS (sensitivity and specificity >90% on a per-lesion basis) [Leber-06, Achenbach-04, Leber-04, Sun-08] but the ability to detect non-calcified plaque, which is thought be a key constituent in high risk plaques and unique to contrast enhanced CTA, is limited to a sensitivity of 58% with an intraobserver variability as high as 37% [Leber-05].

Our data confirm these observations as we demonstrate good sensitivity (76%, 95% CI: 73-78%) and excellent specificity (91%, 95% CI: 88-95%) for the detection of any plaque but significantly lower accuracy for the detection of non-calcified plaque (sensitivity: 57%, 95% CI: 54-61%; specificity: 83%, 95% CI: 81-87%). One explanation for the moderate results in comparison to in-vivo studies is the notable difference in the analytic approach. We assessed the diagnostic accuracy of CTA on a cross-sectional basis while clinical studies report test characteristics on a per lesion basis. Because plaque thickness for an individual plaque varies within cross-sections, smaller parts of a plaque that will be detected on a per lesion basis may not be detected on cross-sections. However, the cross-sectional approach permits a more detailed insight into how specific plaque characteristics are related to diagnostic accuracy. This approach permitted us to identify predictors of the ability of CT to detect and classify plaque.

Significant misclassification by CT occurs by mislabelling mixed plaque as calcified plaque and non-calcified plaque as mixed plaque (67.9% and 42.6% for mixed or non-calcified by IVUS; respectively). Figure 4-4 illustrate how blooming artefacts lead to overestimation of calcified plaque by CT so that the non-calcified part of mixed plaques detected on IVUS cannot be detected in CT. Similarly, blooming of adjacent calcified plaque into cross sections that contain only non-calcified plaque

by IVUS leads to mislabelling them as mixed plaques in CT. These results are not surprising given the large overestimation of the volumes of calcified that have been demonstrated in previous studies [Hoffmann-03, Sarwar-08]. The difficulty to distinguish plaque composition is also reflected in the low inter and intra-observer agreement for mixed and non-calcified plaque (K=0.42 and K=0.56; K=0.48 and K=0.76; respectively). Overall, we found a close association between inter-observer agreement and accuracy of CT assessment of plaque.

Moreover, we found that on a cross-sectional basis only 3% of IVUS cross-sections contain exclusively calcified plaque, while the majority of cross-sections contained non-calcified or mixed plaque. These data suggest that a classification of plaque composition as mixed and calcified may be artificial as most of the plaques that are classified as calcified by CT are indeed heterogeneous in histologic and IVUS analysis.

We demonstrate that maximum intimal thickness and lumen area are independent predictors for the diagnostic accuracy of CT to detect non-calcified plaque. For example, the odds of detecting non-calcified plaque in CT increased by 226% with every 0.1 mm increase in intimal thickness as measured by IVUS. The odds of detecting non-calcified plaque in CT increased by 56% (95% CI: 47-77%) with every 0.1 mm increase in maximum intimal thickness as measured by IVUS. This data also demonstrates only 36% of plaque with an intimal thickness of less than 1 mm are detected by CT, while CTA achieves a sensitivity of 100% for plaque intimal thickness >1.75 mm. Given the distribution of plaque size, 1 mm intimal thickness appears to be a reasonable threshold for sensitivity and detection rate (90%), data that verify initial in vivo observations by Leber et al. [Leber-04] . Because the effect calcium has on the point spread function for resolution, the more calcium in a voxel, the lower the height of the full width half maximum (FWHM) of the point spread function will be and the lower the resolution will be. The lower height of FWHM from a widened point spread function predicts the exact level of measurement uncertainty that we described, which is effectively 1 mm.

This study uniquely defines the limitations of CTA plaque detection and determines predictors of accuracy. If CTA can reliably detect >1 mm thick coronary atherosclerotic plaque it is likely to impact on future risk prediction models. Probably most importantly, these data will enable us to explore the usefulness of coronary CTA as a surrogate marker of treatment success or failure.

LIMITATIONS

Our study has several limitations. It is an ex-vivo study on a small number of super-selected coronary arteries. Despite this the LMS, LAD and RCA were most often assessed. These are the in-vivo sites that are most commonly associated with plaque deposition, stenosis and rupture. The inclusion criteria maximized the yield of non-calcified plaques. This was intentional as CT has long been established as one of the most sensitive tests for the detection of coronary artery calcification and non-calcified plaques appear to be associated with acute coronary syndromes

Ex-vivo plaque constituents may not be representative of their in-vivo equivalents. However every effort was made to ensure that our specimens were prepared and examined on the shortest possible time from harvest. At all times the vessels were maintained at a physiologic pH and temperature to avoid shrinkage. In-vivo validation of our results would be necessary.

CT and IVUS images were acquired in a carefully controlled and optimized environment. The IVUS and CTA images were not degraded by artefact and noise which is commonly encountered in an in-vivo setting. We attempted to reproduce cardiac and coronary artery motion with a motion simulator but it cannot fully replicate the complexity and velocities of in-vivo coronary arteries that demonstrate beat-to-beat variability. Although we applied a stringent and novel approach for co-registration of IVUS and CT cross-sections, minimal co-registration errors could not be completely eliminated.

We did not use the second tube, that allows for dual energy scanning, for calcium subtraction or iodine specific scans but simply as a second tube decreasing the scan rotation time. Using the dual energy option potentially may have helped the problem of calcium blooming and improved plaque detection.

Lastly, the analysis of consecutive cross-sections inherently presents a clustered analysis of data and readings of individual cross-sections are not independent. However, we addressed this issue by reporting the 95% confidence intervals of the data after bootstrapping. Our results suggest a limited effect of data clustering because the bootstrapped confidence intervals did not significantly differ from normal 95% interval analysis. Although random presentation of the cross-sectional images to the readers is an alternative approach to prevent data clustering, such an approach may lead to unrealistically low diagnostic accuracy when compared to an in-vivo per plaque analysis.

CONCLUSION

The diagnostic accuracy and reader agreement of CT technology for the detection of coronary plaque is dependent on plaque composition. This ex-vivo study defines the limits of CT plaque detection as misclassification of non-calcified as mixed plaque and mixed plaque as calcified plaque and a reduced sensitivity to detect non-calcified plaque with <1 mm maximal plaque thickness. These data are crucial to assess whether this technique can be utilized as a surrogate marker of treatment success or failure.

Small coronary calcifications are not detectable by 64-slice computed tomography

In the previous chapter the accuracy to detect and classify plaque was established in ex-vivo coronary arteries. In this chapter coronary arteries were imaged in-vivo in patients with intravascular ultrasound (IVUS) and computed tomography (CT) angiography. Again these images are registered by the method presented in Chapter 3. Calcification were scored on both modalities and in IVUS the length and maximum arc were measured. In the registered images we identified calcification. In 31 arteries we detected 99 calcifications on IVUS, of which only 47 were seen on CT. Calcifications that were detectable on CT were in 80% of the cases larger than 2.0 mm in length and/or larger than 36° in angle. Thus the assessment of small calcifications with CT is restricted.

5.1   INTRODUCTION

It is increasingly recognized that composition and geometry of individual atherosclerotic plaques are important determinants for plaque rupture [Schaar-04]. Detection, characterization and quantification of coronary plaques is therefore important to predict the risk of a cardiac event. One important plaque component is calcium. The calcium score, or so called Agatston Score, is a measure for the extent of calcifications in the coronary tree and can be accurately assessed by e.g. electron-beam computed tomography [Schmermund-97]. The calcium score is a direct measure for the extent of coronary artery disease and has been shown to be associated with cardiac events [Sangiorgi-98]. Not only is the total amount of calcium is indicative for risk of cardiac events, but its local appearance is also related to plaque rupture. It has been demonstrated that large calcifications are more frequently found in stable patients, while small and spotty calcifications have been associated with unstable patients [Ehara-04, Motoyama-07] and thus unstable plaques. Micro-calcifications in the fibrous cap are proposed as a destabilizing factor [Vengrenyuk-06]. Hence the assessment of the amount, pattern and locations of calcium is important to discern vulnerable patients and vulnerable plaques.

Intravascular ultrasound (IVUS) [Kostamaa-99, Hagenaars-00, Scott-00, Kopp-01, Mintz-01] is the most accurate technique to assess coronary calcifications in vivo. However, IVUS is an invasive imaging modality and therefore not suitable for screening applications and risk stratification. Multi-slice computed (MSCT) is a non-invasive imaging technique that provides 3D high quality images of the coronary arteries [de Feyter-04]. Non contrast-enhanced MSCT is currently successfully applied to measure the calcium score [Agatston-90, Sangiorgi-98, Greenland-07]. The accuracy with which contrast-enhanced MSCT can detect local calcifications is largely unknown. Earlier comparisons of MSCT with the gold standard IVUS for the presence of calcifications were done per vessel [Leber-04] or per segment [Schoenhagen-03, Sun-08] and high accuracies were reported. However, these studies did not report on the accuracy of MSCT to detect individual calcifications. In this study we register IVUS and MSCT images such that cross-sectional images can be compared one-to-one and we report for the first time on the ability of contrast-enhanced MSCT to detect individual calcifications.

5.2 METHODS

5.2.1 PATIENTS

We randomly selected 23 patients (18 male, mean age 54 ± 11 year) who were treated in our institution for acute myocardial infarction or unstable angina. Patients were only included in our study if an IVUS pullback was performed in one or more of their coronary arteries, if they underwent MSCT coronary angiography shortly before or after (on average 2.0 days after) the interventional procedure, if they had a heart rate lower than 70 bpm during the MSCT acquisition and had no prior coronary bypass surgery. Exclusion criteria to perform the MSCT were renal failure, contrast allergy, irregular heart rate, contra-indication to β-blockade.

Based on a power calculations in a pilot study, we aimed for 100 calcifications on IVUS, which we reached by inclusion of 23 patients. Of these patients we only included arteries that were not stented. Patient demographics are given in Table 5-1. Our institutional review board approved the initial study protocols, and all patients gave informed consent.

TABLE 5-1: Patient characteristics

Male	18 (78%)
Age, year (± stdev)	54.2 ± 11.5 years
Mean heart rate during CT (± stdev)	62 ± 10.5 beats/min
Symptoms	
Unstable angina pectoris	7 (30%)
Acute myocardial infarction	16 (70%)
Risk factors	
Hypertension	6 (26%)
Hypercholesterolemia	3 (13%)
Smoking	14 (61%)
Family history of acute coronary syndrome	14 (61%)
Diabetes mellitus	2 (9%)
Obese (body mass index ≥30 kg/m2	7 (30%)

N=23. Values are n (%) unless otherwise indicated

5.2.2 IVUS ACQUISITION

Patients received ≥ 200 µg of intracoronary nitroglycerin before acquisition. One or more of the coronary arteries of these patients were imaged by IVUS with commercially available 40 MHz (Atlantis SR Pro, Boston Scientific, Boston, Massachusetts) ultrasound catheters. A motorized pullback was performed at 0.5 mm/s, starting > 10 mm distal to the segment analysed and ending at the aorta-ostial junction. Images were recorded on DVD and off-line analysis with an image-based ECG-gating method [De Winter-04] was performed such that images shortly before systole were extracted from the complete pullback. This provided us with a stack of gated IVUS images with an axial spacing of approximately 0.5 mm (see Figure 5-1a).

5.2.3 MSCT ACQUISITION

The patient preparation, scan protocol, and image reconstruction procedure have been previously described [Mollet-05]. Briefly, MSCT was only performed in patients who had a sinus rhythm, who had no contra-indications to the administration of contrast agents and who were able to hold their breath for 15 s. Patients with heart rates above 70 beats per minute were administered a single oral dose of 100 mg metoprolol 45 minutes before scanning. Scanning was performed on a 64-slice MSCT scanner (Sensation64®, Siemens, Germany). A non-contrast-enhanced scan for calcium scoring was followed by a contrast-enhanced scan (Iomeron 400®, Bracco, Italy) according to a standardized optimized contrast-enhanced scanning protocol. A bolus tracking technique was used to synchronize the arrival of contrast in the coronary arteries with the initiation of the scan. Images were reconstructed with ECG-gating, initially during the mid- to end-diastolic phase (350 ms before the R-wave) with a temporal window of 165 ms. If image quality was poor, more reconstructions at different phases of the cardiac cycle were generated, sometimes combined with a different temporal window; the reconstruction with the best image quality was chosen for further processing. The in-plane voxel size was approximately 0.3 mm and the slice thickness 0.4 mm.
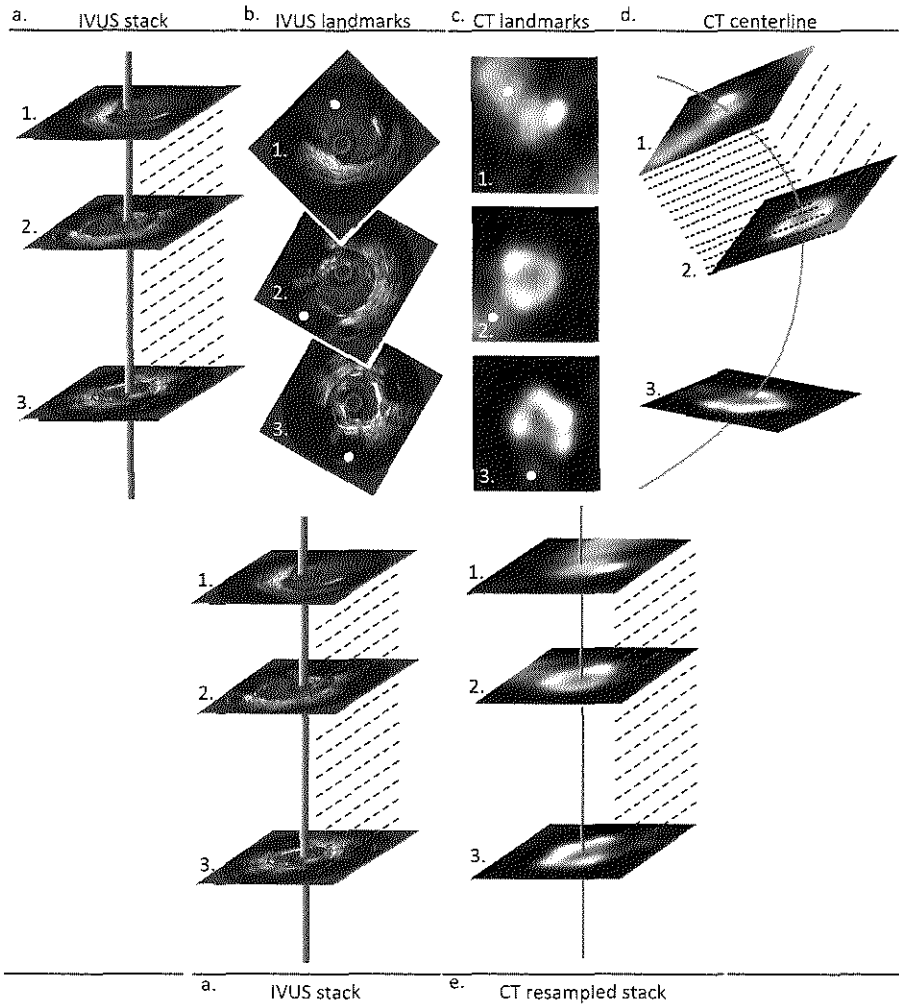
FIGURE 5-1: In the IVUS stack (a) 3 bifurcations (1 to 3) serve as landmarks (indicated by the dots in (b)) for the registration. In the MSCT scan the centerline is tracked through the artery and cross-sectional images are reconstructed (black dotted line). The three bifurcations in the IVUS stack are identified in the MSCT cross-sections (c). The MSCT data is resampled between the landmarks such that the number of images between landmarks is equal to the number of images in the IVUS stack (e).

5.2.4   IVUS AND MSCT REGISTRATION

We used in-house developed software (based on MeVisLab, Mevis, Bremen, Germany) to manually register and analyse IVUS and MSCT datasets. Goal of the registration process was to reconstruct cross-sectional MSCT images of the coronary artery at the same axial position where the IVUS images were obtained. The registration process was carried out by two observers independently and final registrations were made in consensus.

The registration process was performed as follows: After ECG-gating the IVUS images had an axial distance of approximately 0.5 mm (Figure 5-1a). In this IVUS stack we identified bifurcations, which were used as landmarks (Figure 5-1b). To register the MSCT to the IVUS images a centerline of the vessel of interest was manually drawn in the MSCT dataset starting from the ostium. Perpendicular to the centerline, cross-sectional images of the vessel were equidistantly generated at every 0.2 mm (see Figure 5-1d). In this MSCT image set we searched for the IVUS-derived landmarks (see Figure 5-1c). Sampling the MSCT data set with a higher axial resolution compared to the IVUS images (0.2 mm axial distance versus 0.5 mm) enabled us to register the bifurcations in the two data sets more accurately. After manually registration of the side-branches, cross-sectional MSCT images perpendicular to the centerline were generated again, but now such that the number of MSCT images between the landmarks was equal to the number of IVUS images between the landmarks (Figure 5-1e). As registration is only possible between landmarks, at least two bifurcations had to be identified on both imaging modalities. The result of this registration procedure is a corresponding MSCT image for each IVUS image between the most proximal and most distal landmark, thus enabling a one-to-one comparison between these images.

5.2.5   IVUS ANALYSIS

The IVUS images were inspected for the presence of calcium in the wall. Calcium was identified by its specific echogenic appearance, accompanied by an acoustic shadow [Mintz-01]. Calcifications can extend over multiple IVUS images. For each calcification we determined the length and the maximum circumferential angle. The length of a calcification was calculated by multiplying the number of slices the calcium extends over by the mean distance between the images. The angle of a calcification was

determined by drawing two vectors on each cross-section from the center of the vessel to the corners of the acoustic shadowing (see Figure 5-2a). For each calcification the largest angle was determined. The IVUS images were analysed blinded to the MSCT images.

5.2.6 MSCT ANALYSIS

We identified calcifications in MSCT cross-sectional images as any structure with a density of 130 HU or more that could be visualized separately from the contrast-enhanced coronary lumen (because its density was above the contrast-enhanced lumen) and that could be assigned to the coronary artery wall. Also structures with an intensity <130 HU, but clearly embedded in or adjacent to the surrounding non-calcified plaque with a lower intensity were defined as calcifications.

Identification of the calcifications was supported by gradient images. Gradient images are derived from the normal images and they that represent the local change in image intensity Figure 5-2b and Figure 5-2c). The transition from high intensity lumen to the low intensity epicardial tissue is depicted as a white ring in the gradient image. The transition from the high intensity lumen to a calcified plaque results in a second ring adjacent to the ring of the lumen. All the MSCT cross-sections were checked for calcifications blinded from the IVUS images.

5.2.7 ANALYSIS

For each calcification detected in the IVUS images we determined whether it was also present in the corresponding MSCT image, and vice versa. Based upon these analyses we identified three groups: 1) calcifications identified on both modalities; 2) calcifications identified on IVUS only and 3) calcifications identified on MSCT only.

Continuous variables were described by their means and standard deviation (mean ± SD). To evaluate the difference in length and angle between the calcifications seen on both modalities versus those missed on MSCT, a non-parametric two-sample test (Mann-Whitney U) was performed. A receiver-operating characteristic (ROC) curve was created and the area under the curve was determined as well as a cut-off value for calcification length and angle to determine at which values a calcification is detected or not on MSCT. For this cut-off value the sensitivity was reported.
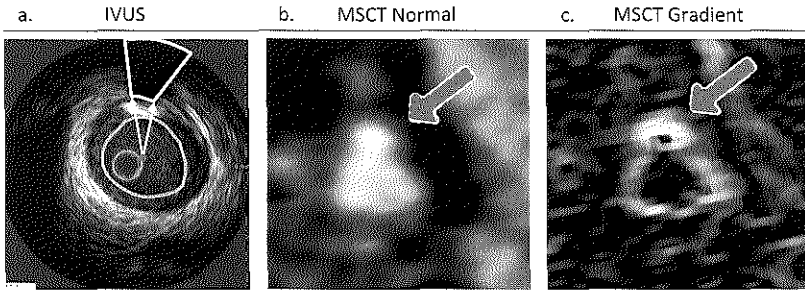
FIGURE 5-2: a) The calcium angle on IVUS is determined by the two vectors from the center of the lumen to the corners of the acoustic shadow. b) Cross-section of coronary arteries imaged with MSCT, with at the arrows a calcification. c) Corresponding gradient image with again the arrow near the calcification. Note the double ring, one from the lumen and one from the calcification.

One-way Anova with post-hoc Tukey HSD analysis was performed to compare length and angle between the groups for the LAD, LCX and RCA. We performed the statistical analysis with SPSS 16.01 (SPSS Inc., Chicago, Illinois) and p-values <0.05 were considered statistically significant.

5.3   RESULTS

5.3.1   CALCIFICATION IDENTIFICATION

We registered 2435 IVUS cross-sectional images with MSCT, with a total length of 1138 mm (446, 329 and 363 mm of the LAD, LCX and RCA respectively). These cross-sections were obtained from 31 coronary arteries (12 LAD's, 9 LCX's, 10 RCA's) of the 23 patients included in our study. Registration of the IVUS and MSCT images was not possible for 4 arteries (3 LCX and 1 RCA), because we were not able to identify at least 2 landmarks.

A total of 107 calcifications were identified on either IVUS or MSCT. We identified 47 calcifications on both IVUS and MSCT, 52 calcifications were identified on IVUS only and 8 were identified on MSCT only (see Table 5-2). From the 99 calcifications identified on IVUS, 52 were missed on the MSCT images. This implies that 53% ± 10% (95% confidence interval) of the calcifications on the IVUS images were not identified on the MSCT images. Less calcifications tended to be missed on the MSCT images in the LAD than in the LCX and RCA (42% versus 61% and 55%, p=0.07).

TABLE 5-2: 2-by-2 contingency table

calcium detected on

IVUS

		yes	no	total
calcium detected on CT	yes	47	8	55
	no	52	-	52
	total	99	8	107

TABLE 5-3: Calcification detection

	n	Length [mm]	Angle [°]
Overall	99	2.5 ±1.99	42 ± 29
Not detected on MSCT*	52	1.4 ± 0.8†	27 ± 16†
Detected on MSCT*	47	3.7 ± 2.2	59 ± 31
LAD	34	2.6 ± 2.2	43 ± 35
Not detected on MSCT	14	1.0 ± 0.6†‡	22 ± 17†
Detected on MSCT	20	3.7 ± 2.3	58 ± 37
LCX	36	2.2 ± 1.3	39 ± 20
Not detected on MSCT	22	1.7 ± 0.8†‡	31 ± 17†
Detected on MSCT	14	3.1 ± 1.6	52 ± 17
RCA	29	2.8 ± 2.3	45 ± 31
Not detected on MSCT	16	1.5 ± 0.8†	26 ± 12†
Detected on MSCT	13	1.5 ± 0.8†	68 ± 31

* Calcifications can be detected on IVUS only, hence not on MSCT or can be detected on both IVUS and MSCT. † Both length and angle are significantly (p<0.05) smaller for the calcifications missed on the MSCT images. ‡ Trend (p=0.053) difference for the length of the calcifications missed on MSCT of the LAD versus the LCX.

We identified 8 calcifications on the MSCT images, which were not seen on the IVUS images. One calcification on the MSCT images turned out to be false-positive since it could be identified as a side branch on the IVUS image. The other calcifications on the MSCT images are presumably the result of local differences in contrast enhancement, and/or imaging artefacts.

5.3.2 CALCIFICATION LENGTH AND ANGLE

In the IVUS images we measured the length and angle of each calcification (Table 5-3 and Figure 5-3 and Figure 5-4). The total length of calcium found was 251 mm (88, 80 and 83 mm for the LAD, LCX and RCA, respectively), which amounts to 22% of the total inspected length. The mean calcification length was 2.5±2.0 mm and the mean angle was 42°±29°.

The calcifications that were not detected on the MSCT images were significantly smaller than those seen on both MSCT and IVUS both with respect to calcification length (1.5±0.8 vs. 3.7±2.2 mm) and calcification angle (27°±16° vs. 59°±31°). The total length of the calcifications missed on MSCT was 75 mm, 30% of the total calcium length.

The mean length and angle of the calcifications was not significantly different when comparing the three coronary arteries. For the LAD, LCX and RCA separately we found that the calcifications missed on the MSCT images were smaller in length and angle. The calcifications missed on the MSCT images in the LAD tend to be shorter (p=0.053) than those missed in the LCX (1.0±0.6 vs. 1.7±0.8 mm).

5.3.3 RECEIVER OPERATING CHARACTERISTICS ANALYSIS

Figure 5-5 shows the ROC-curve for both the length and the angle of the calcification. The area under the curve was 0.88 for the length and 0.86 for the angle. By the ROC analysis we found that calcifications larger than 2.1 mm in length could be seen on MSCT in 85% (sensitivity) of the cases, while those calcifications smaller than 2.1 mm were missed by MSCT in 83% of the cases (specificity). For the angle we found a sensitivity of 81% to detect calcifications with an angle larger than 36° and a specificity of 79%.

Calcification length

not detected on MSCT   ▥ detected on MSCT
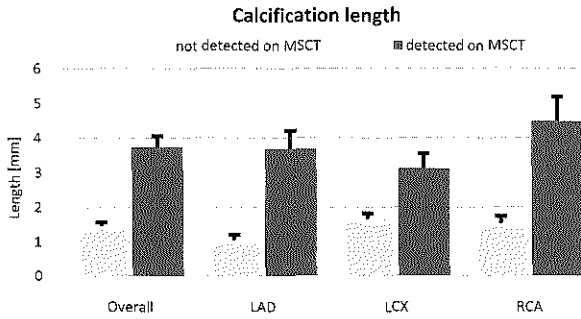
FIGURE 5-3: Average calcification length per vessel. The averages are shown for the calcifications that were seen on IVUS, but missed on MSCT (light bars) and the calcifications seen on both MSCT and IVUS (dark bars). The error bars present the standard error of the mean.

Calcification angle

not detected on MSCT   ▥ detected on MSCT
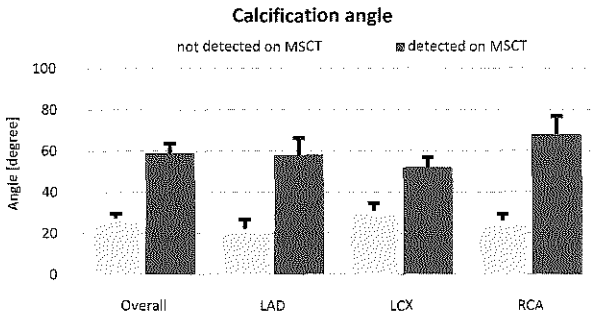
FIGURE 5-4: Average calcification angle per vessel. The averages are shown for the calcifications that were seen on IVUS, but missed on MSCT (light bars) and the calcifications seen on both MSCT and IVUS (dark bars). The error bars present the standard error of the mean.

5.4 DISCUSSION

This is the first study that compares the ability to detect coronary calcifications in 64-slice MSCT and IVUS on a cross-sectional basis. We showed that in patients with acute coronary syndromes 53% of the calcifications seen on IVUS are not detected on contrast-enhanced MSCT. The calcifications missed on the MSCT images are smaller in length and angle than those seen on both the IVUS and MSCT images. We showed that calcifications smaller than 2.1 mm in length or 36° in angle are likely to be missed on MSCT.
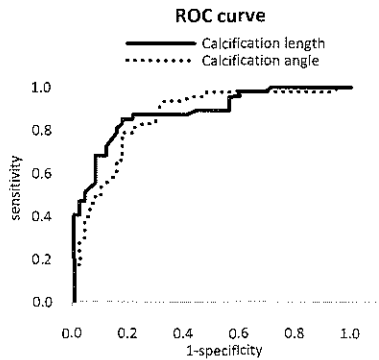
FIGURE 5-5: ROC-curve for the calcium length and calcium angle. Area under the curve is 0.88 for the length and 0.86 for the angle.

Other studies found very good correlation between detection of calcifications on IVUS and MSCT images. Leber et al. [Leber-04] reported a sensitivity of 95% to detect calcium on MSCT per vessel compared to IVUS. Looking at segment level Schoenhagen et al. [Schoenhagen-03] were able to detect calcification with 90% accuracy. Sun et al. [Sun-08] reported on the detection of calcifications on contrast enhanced MSCT scans in even smaller parts of 10 mm. They only missed 2 out of the 27 calcifications on MSCT. The discrepancy of our findings with the studies mentioned above can be explained by the fact that in these studies the presence of calcifications was examined on a vessel or segmental basis, and not on a cross-sectional basis. Assume that a segment contains two calcifications, and that both calcifications are detected by IVUS and only one calcification is detected by MSCT. If we analyse this on a segmental basis, the segment will be positive both on IVUS and MSCT, although one calcification is not detected by MSCT. Following the approach on a cross-sectional basis, we would classify one calcification as detected and the other one as missed on MSCT.

The different physics behind the image modalities results in a far better spatial and temporal resolution for IVUS than for MSCT. The low spatial resolution of MSCT is the main cause of missing the small calcifications, but also the movement during imaging and the reconstruction algorithm influences the visibility of small calcifications. Due to the low temporal resolution of MSCT it is expected that smaller calcifications disappear in their surroundings due to the 'smearing effect' of the moving calcification.

We showed that MSCT can detect calcifications in the LAD better than in the other vessels; we missed less calcifications in the LAD and the calcifications that were missed were also smaller in size than in the other arteries. It is likely that the small calcifications are better distinguished in the LAD because the LAD has the least movement of the arteries during the reconstruction phase of the MSCT images [Achenbach-00], thus reducing the 'smearing effect'.

For this study we choose to use the contrast enhanced MSCT data. To ensure that we did not miss calcifications primarily due to the overshadowing of the contrast agent in the contrast enhanced scan we checked whether missed calcifications on the contrast enhanced scan were visible on the non-contrast enhanced scan. We first located the coronary segment on which we saw the calcification on IVUS on the contrast enhanced scan. We searched for the same segment in the non-contrast enhanced scan. Since accurate matching of the 2 MSCT scans is a real challenge, we were only able to approximately locate 24 of the missed calcifications on the non-contrast scan. On these positions we only found two times a calcification with an intensity just above the threshold of 130 HU. The size and intensity of these 2 spots was comparable to the noisy spots in the ventricle that reach also 130 HU. This implies that the calcifications are missed because of their size and not due to the blooming effect of the contrast agent.

If we would have used a non-contrast enhanced scan in the first place we would not have to check for the presence of calcification on the non-contrast enhanced scan afterwards. However the non-contrast enhanced scan is not a good alternative for our purpose. This scan has a z-spacing of 1.5 mm and it is therefore unlikely that we can identify small calcifications we missed on contrast enhanced scan. Besides, a cross sectional comparison of the IVUS images and the MSCT images as presented in this study would not have been possible since the registration procedure relies on identifying side branches, which are not visible on a non-contrast-enhanced scan.

For this study we choose patients who were have acute myocardial infarction or unstable angina. These patients tend to have more small spotty calcifications than stable patients [Ehara-04, Motoyama-07]. The percentage of missed calcifications in stable patients may therefore be lower.

The clinical consequence of missing calcifications on MSCT on e.g. a volumetric calcium score can be estimated by comparing the volume of the missed calcification to the volume of all calcifications. We miss half the calcifications and the missed calcifications are smaller. The length and the arc of the missed calcifications is ap-

proximately 60% of the average values (Table 5-3). Assuming that the thickness of the missed calcifications is also 60% of the average value, the average volume of the missed calcifications is approximately 20% of the average volume of all calcifications. Combined with the observation that half of the calcifications are not detected, this implies that approximately 10% of the total volume of the calcifications will be missed by MSCT. It is therefore unlikely that the missed small calcifications have a large effect on the calcium score, and thus on its use for the prediction for the risk of cardiac events. On the other hand, missing the small calcifications might be crucial in the local detection of vulnerable plaques, as small and spotty calcifications may be related to a vulnerable plaque phenotype [Ehara-04, Vengrenyuk-06]. Since calcifications smaller than approximately 2 mm cannot be seen on MSCT, improvements in the MSCT technology will be necessary to be able to differentiate plaque components and the vulnerable plaque on a local scale.

In summary, half of the calcifications seen on the IVUS images cannot be detected on 64-slice MSCT angiography images because of their size. The limited resolution of MSCT in combination with the obscuring effects of the contrast in the lumen hampers the identification of small calcifications.

Location of plaque rupture in human coronary arteries is related to shear stress

The combination of the reconstruction technique in Chapter 3 and computational fluid dynamics (CFD) allows us to determine the wall shear stress (WSS) distribution in vivo in patient specific geometries. We applied this method to investigate the relationship between the location of plaque rupture of non-culprit lesions and WSS in patients suffering from an acute myocardial infarction or unstable angina. From the 17 ruptures that were identified, 14 were found at the upstream side of the plaque. For 11 ruptures the WSS was higher than the average WSS on the plaque. Since the plaque composition plays a crucial role in the plaque rupture process, WSS might be a force that influence plaque composition over time.

6.1 INTRODUCTION

Vulnerable plaques are characterized by the presence of a large lipid pool, which is separated from the lumen by a thin fibrous cap, often infiltrated by macrophages [Schaar-04]. Rupture of this fibrous cap is generally regarded as one of the main underlying causes of cardiovascular events [Falk-95]. Rupture occurs when the stresses in the cap of the plaque exceed the strength of the cap [Lee-93]. The composition of the plaque plays a crucial role in the rupture process: it determines how blood pressure is translated into stresses in the wall, and composition also determines the strength of the tissue [Loree-94, Holzapfel-05].

Several studies showed that rupture occurs more frequently in the upstream region of the plaque than in the downstream region, indicating that the strength of the plaque is lower there [Maehara-02, Fujii-03, Lovett-03, de Weert-09]. In a recent case study, Groen et el. applied computational methods based on patient-derived geometries to determine the blood flow induced shear stress at the location of plaque rupture in a human carotid artery [Groen-07]. They found that the rupture location was exposed to elevated shear stress, indicating that the plaque was weakest there. This observation was confirmed in a larger study in human carotid arteries [Tang-09]. Plaque rupture of culprit lesions in relatively straight segments in coronary arteries was explored recently, and rupture location was associated with focal elevation of shear stress [Fukumoto-08].

We recently developed a reconstruction technique that combines multislice computer tomography (MSCT) and intravascular ultrasound (IVUS) to generate three dimensional (3D) reconstructions of human coronary arteries [van der Giessen-09]. The combination of this reconstruction technique and computational fluid dynamics (CFD) allows us to determine the shear stress distribution in vivo. We applied this method to investigate the relationship between the location of plaque rupture of non-culprit lesions and shear stress in coronary arteries of patients suffering from an acute myocardial infarction or unstable angina.

6.2 METHODS

6.2.1 PATIENT POPULATION

We investigated the main coronary arteries of patients who were treated in our hospital for an acute myocardial infarction or unstable angina. The patients underwent a percutaneous coronary intervention and were imaged just prior or after the intervention by means of contrast enhanced MSCT. After stenting of the culprit lesion, at least one of the main coronary arteries was interrogated by means of IVUS. In total, the IVUS images from 58 coronary arteries (25 left anterior descending (LAD), 19 left circumflex (LCX) and 14 right coronary arteries (RCA)) from 33 patients were investigated for the presence of plaque rupture. Our institutional review board approved the initial study protocols, and all patients gave written informed consent.

6.2.2 MSCT IMAGING

The patient preparation, scan protocol, and image reconstruction procedure for the MSCT imaging, have been previously described [Mollet-05]. Briefly, MSCT imaging was performed with a 64-slice scanner (Sensation64®, Siemens, Germany). A non-contrast-enhanced scan for calcium scoring was followed by a contrast-enhanced scan (Iomeron 400®, Bracco, Italy) according to a standardized optimized contrast-enhanced scanning protocol. A bolus tracking technique was used to synchronize the arrival of contrast in the coronary arteries with the initiation of the scan. Images were taken during the mid- to end-diastolic phase (350 ms before the R-wave) and reconstructed with a temporal window of 165 ms. The in-plane voxel size was approximately 0.3 mm and the slice thickness 0.4 mm.

6.2.3 IVUS IMAGING AND ANALYSIS

Patients received ≥ 200 µg of intracoronary nitroglycerin before the IVUS acquisition. IVUS images were acquired during a continuous motorized pullback (pullback speed of 0.5 mm/s) of the IVUS catheter (Atlantis SR Pro, Boston Scientific, Boston, USA or Eagle Eye, Volcano Therapeutics, San Diego, USA). R-top images from the IVUS pullback were selected in a post-processing step, using a validated image selection method [de Winter-04]. The resulting axial distance between the IVUS images was
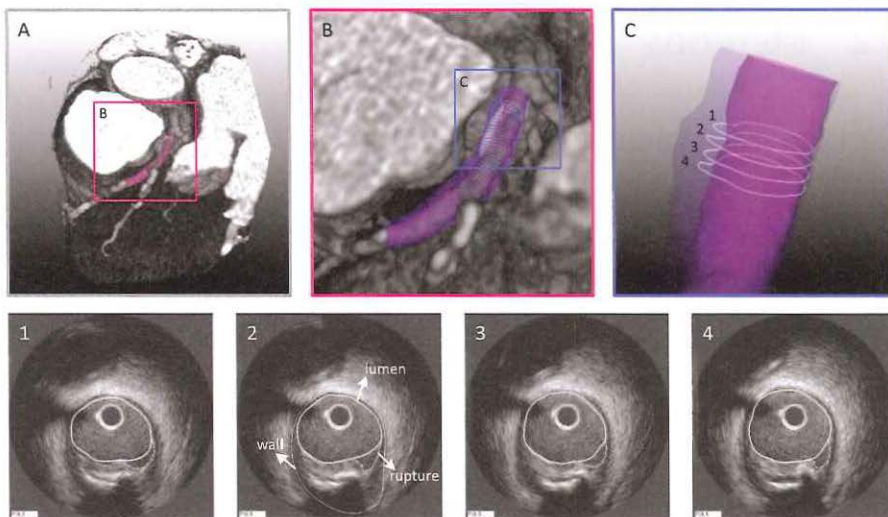
FIGURE 6-1: Example of the fusion procedure to combine IVUS with MSCT data. After matching the landmarks in the two data sets, the lumen and wall contours of the IVUS images can be positioned in 3D and combined with the MSCT data (panel A). A close up of the proximal part of the data set is shown in panel B, illustrating that the side branch data cannot be imaged with IVUS. In this example, a plaque rupture was observed in 4 consecutive IVUS slices (panels 1 to 4). In panel 2, it is illustrated how we annotated the lumen and the vessel wall, and how the lumen at the location of the rupture was reconstructed. Panel C shows 3D position of the contours from the panels 1 to 4.

approximately 0.5 mm, and the in-plane resolution was 0.15 mm. The gated IVUS images were analysed using semi-automatic segmentation software (QIVUS, Medis, Leiden, The Netherlands). The contours of the external elastic laminae as well as the lumen-wall interface were identified following previously published guidelines [Mintz-01]. All the IVUS images were scrutinized for the presence of cavities, indicating the presence of a plaque rupture [Maehara-02]. Once the cavities were identified, the animated IVUS images of the complete pullback were analysed to establish whether these cavities were filled with the speckling appearance of blood to ensure that they were in contact with the lumen. If this was the case, the cavities were labelled as a rupture. We only included plaque ruptures that were at least one diameter distal or proximal from a side branch. In the gated IVUS images that contained a rupture,

a third contour was drawn to represent the lumen as it was before the rupture occurred (Figure 6-1). In the subsequent analysis, these sets of contours were used to establish the following: 1) the 3D lumen surface to serve as an input for the CFD, 2) the wall thickness to identify plaques, and 3) location of the rupture.

6.2.4   3D RECONSTRUCTION PROCEDURE

The 3D geometry of the lumen and the vessel wall of the coronary artery were obtained by a previously described fusion procedure of the MSCT and the IVUS data [van der Giessen-09] for which we applied in house developed tools using MeVisLab (Mevis, Bremen, Germany). Briefly, the lumen centerline was tracked in the contrast-enhanced MSCT image following a manual tracking procedure. Subsequently, we extracted cross-sectional MSCT images that were perpendicular to this centerline to compare them to the IVUS images. In both image sets, we identified identical bifurcations as fiducial points. These landmarks were used to fuse the two data sets in order to identify the 3D position of each IVUS contour. This enabled us to determine the 3D position of each contour, and thus the location of the rupture. An example of the fusion procedure is illustrated in Figure 6-1.

6.2.5   SHEAR STRESS COMPUTATION

The 3D lumen contours were used to generate a surface which was further processed with VMTK (www.vmtk.org). The main processing step involved adding in- and outflow extensions to facilitate prescribing the appropriate boundary conditions. The surface was converted into a finite element mesh with the aid of the mesh generator GAMBIT (Ansys, Inc., Canonsberg , USA). A linear tetrahedral mesh was generated with mesh refinements near the wall to generate mesh-independent solutions. Since we did not obtain flow measurements in the patients, we had to assume a flow rate at the inlet. We used the in-vivo measurements from Doriot to obtain the relationship between diameter and flow in diseased human coronary arteries [Doriot-00]. Based on these data and the average diameter of the coronary artery under investigation, the average inflow for the coronary arteries was 42±27 ml/min. We imposed the flow at the inlet using a parabolic velocity profile. No-slip boundary conditions at the wall and traction-free outlet boundary conditions were used. A non-Newtonian viscosity model was applied to model the behaviour of blood [Gijsen-99]. The Navier-Stokes equations were solved with FIDAP (Ansys, Inc., Canonsberg , USA), using standard numerical techniques.

6.2.6 DATA ANALYSIS AND STATISTICS

A segment is defined as the part of the coronary artery between two side branches where the plaque rupture was found. A segment may contain more than one plaque: whenever we refer to plaque, we mean the plaque with the rupture. All values are reported as average value ± standard deviation.

Rupture location is qualitatively assessed by mapping the rupture location on a plaque template. In this template, we distinguish 5 different plaque regions: the upstream, mid-cap and downstream region, and the shoulder regions. For each rupture location, we visually assessed in which plaque region it occurred.

For the quantitative assessment, all the parameters that were determined were mapped on the luminal surface and subsequently analysed (Figure 6-2). The distance between lumen and vessel wall interface was used to determine wall thickness. At those locations where wall thickness was less than 0.5 mm, we labelled the arterial wall as healthy, and where wall thickness exceeded 0.5 mm we called it plaque [Clarijs-97]. We determined the average wall thickness and average shear stress for the complete segment, for the healthy part, for the plaque region and for the location of rupture.

At the minimal lumen area, we determined area stenosis (area stenosis = (lumen area at the reference cross section – lumen area)/lumen area at the reference cross section * 100%) and remodeling-index (remodeling-index = vessel area – vessel at the reference cross section)/vessel area at the reference cross section * 100%). The reference cross section was defined as the cross section with a maximum lumen area in the segment. Area stenosis and remodeling-index were determined for the complete segment, plaque region and rupture location.

Whether rupture occurred more frequently upstream than downstream of the minimal lumen area of the plaque was tested with a χ^2-test. To compare average values, a paired t-test was applied. To compare the shear stress in the healthy part of the segment to the shear stress over the plaque and the rupture location, ratios were determined. To obtain a normal distribution of the ratios, we applied a log transformation, and the differences between the ratios were tested with a paired t-test. P-values below 0.05 were considered statistically significant. All statistical analyses were carried out using Matlab (The MatWorks, Natick, USA).

wall thickness   wall shear stress
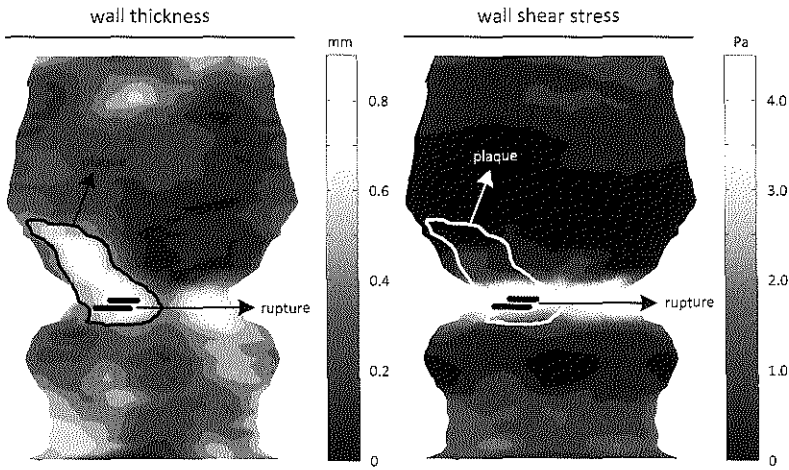
FIGURE 6-2: After the 3D reconstruction procedure and the computational fluid dynamics, we have wall thickness (left panel) and shear stress data (right panel) available for each point along the lumen-wall interface. Furthermore, from the wall thickness map, we can determine the plaque. The location of the rupture was derived from the IVUS contours.
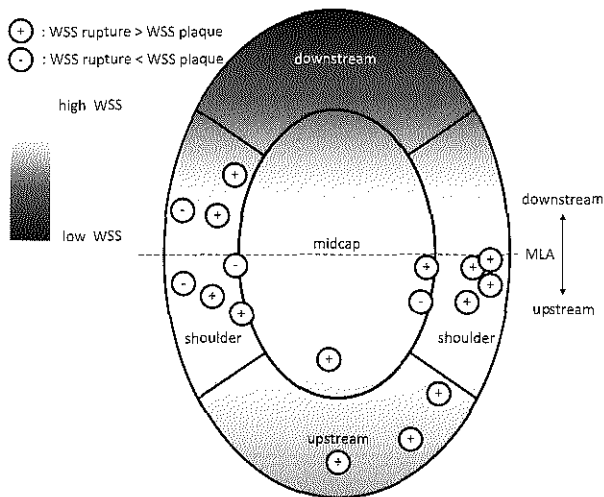
FIGURE 6-3: The location of each plaque rupture is mapped onto a plaque template. The plaque template was divided into the following regions: upstream, midcap, downstream and shoulder region. Furthermore, we determined whether the rupture location was proximal or distal from the minimum lumen area of the plaque. Each circle stands for one rupture, and the plus or minus indicates whether the wall shear stress (WSS) at the rupture location was higher (+) or lower (-) than the average WSS over the plaque.

6.3   RESULTS

6.3.1   GENERAL

In total, 17 ruptures were identified in 13 coronary arteries from 11 patients. The ruptures were found in the LAD (n=8), in the LCX (n=6) and in the RCA (n=3).

The segments were mildly to moderately diseased. The lumen area of the segments was 7.02 ± 3.00 mm^2, corresponding to a diameter of 2.99 mm. Some of the segments contained lumen narrowing plaques, resulting in an area stenosis of 49 ± 16 %. The vessel area of the segments was 13.2 ± 5.4 mm^2 and they did not show positive remodeling: the remodeling index was -9 ± 11 %. The wall thickness in the segments was slightly above the threshold value for the plaque: 0.57 ± 0.15 mm. The average shear stress in the segments was 0.96 ± 0.20 Pa.

In contrast to the segments, the plaques showed a positive remodeling-index (8 ± 8%, $p<0.05$). The area stenosis of the plaques was 41 ± 18 %. The wall thickness of the plaques was 0.88 ± 0.28 mm, which is significantly larger the average wall thickness in the segments. The average shear stress over the plaques was 1.01 ± 0.35 Pa.

6.3.2   RUPTURE LOCATION VERSUS PLAQUE GEOMETRY

The qualitative assessment of the rupture locations is shown in Figure 6-3. The ruptures were most frequently observed in upstream of the minimal lumen area of the plaque (n=14). In the shoulder region, 8 ruptures were found, 3 in the mid-cap region and 3 in the upstream region of the plaque. Only 3 ruptures were observed downstream of the minimal lumen area of the plaque, all of them in the shoulder region (upstream versus downstream, $p<0.01$). No plaque ruptures were present in the downstream region.

The quantitative data confirm these observations. The average distance from the rupture to the location of the minimal lumen area was 2.7 ± 3.7 mm proximal. The wall thickness at the location of the rupture was 0.76 ± 0.24 mm, which was significantly larger than the wall thickness of the healthy part of the segment (0.29 ± 0.05 mm, $p<0.01$) but also significantly lower than the wall thickness of the plaque
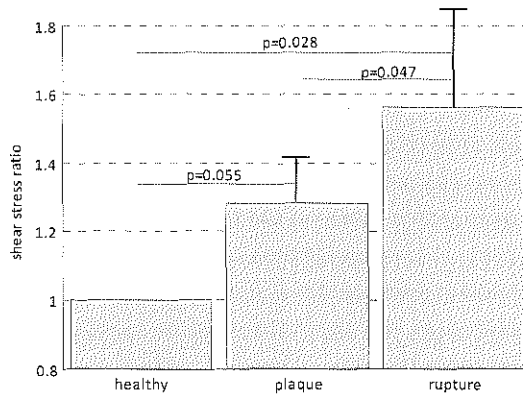
FIGURE 6-4: Ratio of shear stress in the healthy part of the segment, the plaque and the ulcer location.

(0.88±0.28 mm, p<0.05). The area stenosis at the rupture location was significantly lower than the area stenosis of the plaque (29±19% vs 41±18%, p<0.01). The average remodeling-index at the location of plaque rupture did not differ from the remodeling-index of the plaque (9±8%).

6.3.3   RUPTURE LOCATION VERSUS SHEAR STRESS

The shear stress over the plaque was higher than the shear stress in the healthy part in the segment for 11 out of 17 plaques. The rupture location was subjected to higher shear stress than the healthy part of the segment in 15 out of 17 cases. In total, 13 out of 17 rupture locations were subjected to shear stress levels that were higher than the shear stress over the plaque. The shear stress in the healthy part of the segment was 0.82±0.20 Pa, the shear stress over the plaque was 1.01±0.35 Pa and the shear stress at the rupture location was 1.19±0.60 Pa. The results are summarized in Figure 6-4, where the shear stress over the plaque and the rupture was divided by the shear stress in healthy part of the segment: shear stress at the rupture location is significantly higher compared to the shear stress in the healthy part of the segment (+56%, p<0.05) and significantly higher than the shear stress over the plaque (+14%, p<0.05).

6.4   DISCUSSION

The location of plaque rupture of non-culprit lesions in human coronary arteries was investigated with a recently developed 3D reconstruction technique based on the fusion of MSCT and IVUS. This technique was combined with computational fluid dynamics to study the relationship between the location of plaque rupture and blood flow induced shear stress. The main findings of this study are that plaque rupture was predominantly found in the shoulder region, upstream of the minimum luminal area of the plaque. Moreover, the shear stress at the rupture location was higher than the average shear stress the plaque was exposed to.

Other studies also observed that plaque rupture was more frequent in the proximal region of the plaque, both in carotid arteries [de Weert-09, Tang-09], and in coronary arteries [Maehara-02, Fujii-03, Fukumoto-08]. Rupture of a plaque is determined by local blood pressure and plaque composition. The plaques in our study are generally not severely lumen narrowing, implying that blood pressure in proximal region of the plaque will be almost equal to the blood pressure in the distal region. The prevalence of rupture in the proximal region of the plaque must therefore be a reflection of the difference in plaque composition. Several studies indicate that plaque composition indeed differs with respect to location. In human carotid arteries it was observed that macrophages dominate the upstream part of the plaque, while smooth muscle cells –which are generally considered to be a stiff wall component, are more predominant downstream [Dirksen-98]. In a previous study, we demonstrated that human coronary plaques are stiffer in the downstream region of a plaque [Gijsen-08]. The results of this study indicate that also for the non-culprit coronary plaques, composition upstream of the minimal lumen area is different from downstream.

We also showed that the shear stress at the rupture location is higher than the average shear stress the plaque is exposed to. This is in line with previous studies relating shear stress to rupture location in human carotid arteries [Groen-07, Tang-09]. The recent results from Fukumoto et al. qualitatively confirmed this in human coronary arteries [Fukumoto-08]. They showed that rupture location in culprit coronary lesions is associated with focal elevated shear stress. The culprit lesions had an average area stenosis of almost 79.9%, which is much higher than non-culprit lesions in our study (41%), indicating that the non-culprit plaques in our study represent an

earlier phase of atherosclerosis. Based on these observations, one might speculate that shear stress modulates plaque composition in various phases in atherosclerosis such that high shear stress enhances vulnerability of lumen intruding plaques in both carotid and coronary arteries.

The endothelium might be an important factor that regulates the influence of shear stress on plaque composition. The endothelium forms the inner lining of our cardiovascular system, and it is an important barrier between blood and the vessel wall. The endothelium regulates various transport processes; it expresses multiple signalling molecules at its surface and secretes signalling agents into the blood and the vessel wall, all depending on its function [Davies-95]. Blood flow induced shear stress strongly influences endothelial function [Malek-99], and it is well established that it is one of the key factors localizing early atherosclerosis [Slager-05]. Recently, it was hypothesized that shear stress might also be involved in modulating plaque composition in more advanced atherosclerosis [Slager-05, Chatzizisis-07]. In coronary plaques, we found evidence for this hypothesis: coronary plaque regions exposed to elevated shear stress levels were significantly softer than plaque regions exposed to lower shear stress [Gijsen-08].

The mechanisms through which shear stress might affect plaque composition in more advanced atherosclerosis are largely unknown. Various pathways were identified [Slager-05], including nitric oxide mediated smooth muscle cell apoptosis and plasmin induced metalloproteinase activity, along which high shear stress could influence plaque composition. To establish if these shear stress related pathways modulate plaque composition, animal experiments in which shear stress can be altered – e.g. in atherosclerotic mice models [Cheng-06]- are needed. The identification of these mechanisms is also important for the clinical implication of this study: if the dominant shear stress related mechanism that induces plaque vulnerability can be established, pharmaceutical intervention to block the responsible pathways could be explored.

We studied only a limited number of plaque ruptures from patients that suffered from an acute myocardial infarction or unstable angina. Although the results of this study support previously reported data on the location of plaque rupture with respect to location and shear stress [Groen-07, Fukumoto-08, Tang-09], additional in vivo studies in patients are required to firmly establish quantitative relationships. To compute the shear stress, the lumen area of the coronary artery had to be reconstructed manually to estimate its shape before rupture. Since the ruptures were rel-

atively small, the lumen contours could be extrapolated readily. In a previous study, it was demonstrated that the continuity of the lumen contour was not compromised [Groen-07], and we therefore expect that errors in reconstructing the lumen only marginally affects our shear stress computations.

In conclusion, evidence is mounting that plaque rupture is localized in the upstream region of the plaque. In non culprit lesions, the location of plaque rupture is predominantly present in the shoulder region of the plaque, and more specifically, in those regions that are exposed to elevated shear stress levels. This implies that shear stress might influence plaque composition, and the responsible shear stress related mechanisms might form an interesting target for therapeutic interventions.

3D distribution of lipid rich plaque as assessed by fusion of in-vivo NIR-IVUS and MSCT
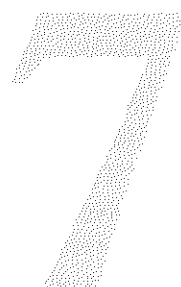
This chapter shows that not only lumen an wall contours from gray-scale intravascular ultrasound (IVUS) can be reconstructed into 3D with the aid of multi-slice computed tomography, but also wall information derived from other catheter-based imaging modalities. New IVUS-related technologies, such as virtual histology and palpography, add information about the components of the arterial wall. In this case-report a catheter with the combination of IVUS and near infrared spectroscopy (NIR) was used to image the coronary wall. NIR can give the probability of the presence of a lipid core in the wall. This wall information can be reconstructed into 3D and related to the wall shear stress.

7.1 INTRODUCTION

There is ample evidence that the development of acute coronary syndrome is linked to the presence of lipid-core containing, necrotic plaques. However, there is little information on the natural history of lipid-core plaques in humans. A close link between structural changes of atherosclerotic plaques over time to the local shear stress conditions in the arterial system has been reported [Slager-05]. The current paradigm postulates that low shear stress is a necessary condition for plaque accumulation. However, once lumen narrowing occurs because of plaque, local shear stress increases [Wentzel-03]. While low shear stress is recognized for its pro-atherogenic impact on the endothelium [Slager-05], the role of (low or high) shear stress in plaque composition, destabilization and rupture is less clear. We describe an approach that allows studying the interaction of lipid-core plaque accumulation and local shear stress in a correct anatomical 3-dimensional (3D) reconstruction of coronary arteries in living patients.

7.2 METHODS

A 61-year-old male with a history of myocardial infarction and stenting of the right coronary artery underwent coronary catheterization for recurrent angina. A prior 128-slice dual source computed tomography scan (MSCT, Somaton Definition Flash®, Siemens, Germany), had suggested a lumen narrowing in the anterior descending artery (LAD) (Figure 7-1A), which was subsequently proven to be physiologically significant by pressure wire studies. In order to identify the presence of lipid-core plaque, a pullback with a recently developed combination catheter with intravascular ultrasound (IVUS) and near infrared spectroscopy (NIR) (InfraReDx, Burlington, MA, USA) was performed (pullback speed 0.5 mm/s, acquiring 16 frames/s). NIR data were displayed as color maps indicating the probability of the presence of lipid-core by NIR as described previously [Gardner-08].

Although the combination catheter allows simultaneous display of the IVUS derived 2D geometry and presence of lipid-core plaque in vivo (Figure 7-1B), it was up till now not feasible to visualize that information in anatomically correct 3D space, which is crucial to understand the relationship with other pathophysiologic parameters, such as shear stress. Recently, we developed a technique to produce 3D coronary reconstructions by fusion of MSCT and IVUS information [van der Giessen-09].

We adapted this approach for the combined NIR-IVUS data to reconstruct the lipid core plaque distribution in three dimensions. Moreover, in the lumen of this 3D reconstruction the local shear stress were assessed by computational fluid dynamics [Wentzel-03].

7.3   RESULTS

In our patient, a complex plaque and shear stress distribution pattern is visible (Figure 7-1C, D). Confluent lipid-core plaques are exclusively located on the inner curvature of the artery towards the myocardium (Figure 7-1C), which are generally considered low shear stress regions. In the region of maximum lipid-core plaque accumulation, lipid core plaque extents over roughly 75% of the artery's circumference (Figure 7-1, asterix). At this site and at some other locations, the local shear stress as computed is relatively high (Figure 7-1D). This can be explained by the fact that there is advanced disease with marked thickening of the vessel wall, which resulted in lumen narrowing.

7.4   CONCLUSION

Our observation illustrates that the combination of NIR, IVUS and MSCT data can be used to study the relationship between shear stress and lipid core distribution in the arteries of patients undergoing catheterization, which is of high potential for longitudinal studies on plaque modulation. Moreover, hypotheses on the natural history of lipid core plaques can be tested in patients in-vivo.
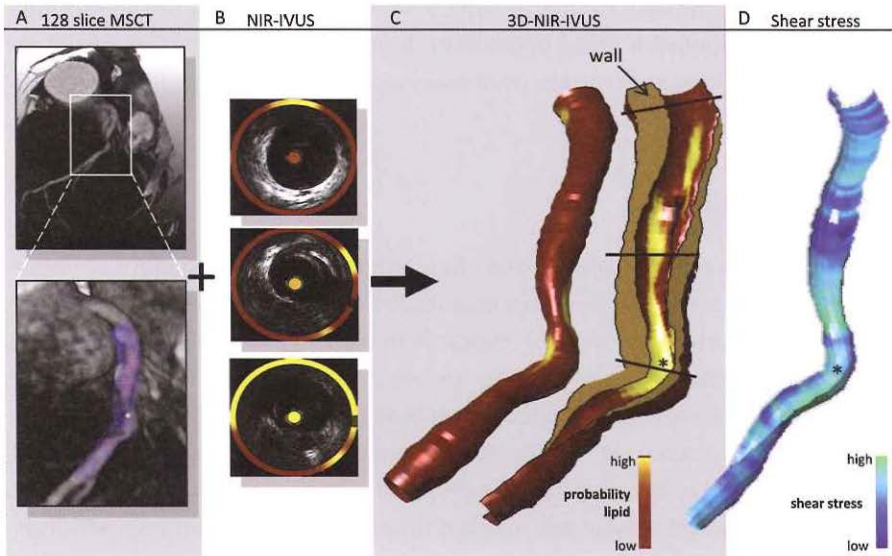
FIGURE 7-1: 3D reconstruction of the spatial, in-vivo distribution of lipid-core plaque and local shear stresses in the left anterior descending artery (LAD) obtained by fusion of multislice CT (MSCT) and cross sectional images as derived from a combination catheter visualizing near infra red (NIR) and intravascular ultrasound (IVUS) information simultaneously. A) 3D rendering of the MSCT, with a magnified image of the proximal part of the LAD. Overlaid on this magnified image (lower panel) are the contours of the lumen (pink) and media (blue) as derived by NIR-IVUS. B) Cross sectional coronary images obtained by the NIR-IVUS catheter. The NIR data for each cross-section are displayed in a circle (color map) around the IVUS image representing the probability for lipid core plaque in the vessel wall (yellow: high probability). C) 3D reconstruction of the coronary, on which the NIR lipid map is superimposed. The left panel shows the epicardial vessel surface, the right panel shows the endoluminal surface of the half of the artery closest to the myocardium in a cut-away view. Note that the vessel wall (brown) is markedly thickened. D) Corresponding shear stress distribution on the endoluminal vessel wall surface. The panel shows a cut-away view of the half of the artery closest to the myocardium. Dark blue indicates low shear stress and light blue high shear stress.

The influence of boundary conditions on simulated shear stress in coronary trees
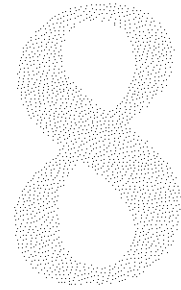
The side-branches are predilection sites of atherosclerosis and therefore interesting to study the relation between WSS and atherosclerosis. In contrast to IVUS, CT has the capability of imaging all the larger coronary arteries simultaneously, thus not only the main branch, but also the large side-branches. Calculating the WSS in geometries with side-branches requires prescription of boundary condition at the side-branch locations to divide the flow over the different branches. Since CT does not come with hemodynamic measures estimation have to be made for this outflow conditions. In this two models that estimate the flow division based on the available geometry are compared with respect to the influence on the WSS distribution. The choice of model influenced absolute WSS; however, relative WSS measures were hardly influenced by the choice of the model.

8.1   INTRODUCTION

Flow induced wall shear stress (WSS) is an important parameter in the localization of early atherosclerosis [Giddens-93, VanderLaan-04]. It has been demonstrated that sites with low WSS, such as the inner curve of arteries and regions close to bifurcations have a more atherogenic phenotype [Malek-99, Jeremias-00, Cunningham-05]. It is hypothesized that WSS also influences the development of atherosclerosis in the more advanced stages of the disease [Wentzel-03, Slager-05, Chatzizisis-08]. WSS is thus an important parameter to study atherosclerosis research.

Computational fluid dynamics (CFD) is a frequently applied technique to assess the local time-averaged WSS distribution in human coronary [Slager-00]. This technique requires information of the 3D lumen geometry of the vessel under study, preferably combined with hemodynamic data, such as pressure and flow. This data is necessary for the CFD simulations to prescribe appropriate boundary conditions at the inlet of the artery and at the outflow of the side-branches. To obtain 3D coronary geometries and hemodynamic data most studies rely on invasive catheter based imaging techniques, such as intravascular ultrasound (IVUS) [Krams-97, Wentzel-03]. These techniques have limited possibilities to assess the geometry in and around bifurcation regions [Gijsen-07] and are less suitable for repeated WSS assessment over time because of their invasive nature.

Multi-slice computed tomography (MSCT) coronary angiography is a very promising non-invasive imaging technique to visualize the coronary artery including the bifurcations. Spatial resolution is the best among non-invasive imaging techniques and the radiation dose is now within limits such that serial imaging over time is acceptable. Since MSCT is not limited to imaging the main arteries only, as IVUS is, it opens the possibility to simulate WSS near bifurcations. However MSCT cannot provide any flow or pressure information, which is needed for the CFD simulations.

Studies on WSS in human coronary arteries are regularly performed without patient-derived flow measurements [Krams-97, Soulis-06, Frauenfelder-07]. In these studies an average WSS at the inlet segment was assumed based on literature values and flow was then determined based on the diameter of the inlet segment. An other approach that is regularly applied is performing WSS simulations with a wide range of Reynolds numbers [Perktold-91, He-96, Joshi-04], leading to a wide variety of average WSS values at the inlet.

Studies that calculated time-averaged WSS in coronary geometries including side-branches prescribed stress-free outflow in the side-branches [Boutsianis-04] or applied Murray's Law [Farmakis-04, Joshi-04] to determine the flow ratio. According to Murray's Law the flow ratio over two branches equals the ratio over the diameters cubed [Murray-26]:

$$\frac{q_2}{q_1} = \left(\frac{d_2}{d_1}\right)^3$$

EQUATION 8-1

,with q the flow and d the diameter of the branches.

Murray's Law is based on the minimization of work, but only includes the work to overcome the resistance of viscous drag and the metabolic work to maintain blood volume and the vessel tissue. This law also relies on several assumptions with respect to geometry and flow profile [Sherman-81]. Under these assumptions not only the flow-diameter relation Equation 8-1 holds, but also the relationship that the diameter of the mother branch cubed is equal to the summation of the diameter of both daughter branches cubed:

$$d_M^3 = d_{D1}^3 + d_{D2}^3$$

EQUATION 8-2

,with d_M, d_{D1}, d_{D2} the diameters of the mother and the two daughter branches respectively. Although one can assume that Murray's Law is a better assumption than stress-free outlet conditions, it is debatable how well this law applies to healthy as well as to diseased coronary arteries. Studies that measured the diameters in the coronary tree [Kassab-95, Finet-08], but also studies that modeled the coronary tree geometry [VanBavel-92, Mittal-05, Huo-07] and related flow and diameter, report different, and constantly lower, power values than the cubed power derived by Murray's Law.

The relation between diameter and flow in human coronary arteries is not yet established based on in-vivo measurements. In-vivo experimental data of flow and diameter of the human coronary arteries is available, but to our best knowledge, the combination of diameter and flow in both mother and side-branches has only been reported once, by Doriot et al. [Doriot-00]. With these measurements the relationship between diameter and flow, and between diameter ratio and flow ratio in the coronary arteries can be established.

The aim of our study is twofold; In the first place we will establish the relation between flow and diameter, and diameter ratio and flow ratio in human coronary bifurcations by analyzing the in-vivo flow and diameter measurements performed by Doriot et al.; These relations will be used as inflow and outflow boundary conditions. Our second aim is to demonstrate the impact of prescribing these boundary conditions versus boundary conditions obtained from Murray's Law on the WSS distribution in patient-specific coronary bifurcations.

8.2 METHODS

8.2.1 DERIVATION OF FLOW-DIAMETER RELATION

MEASUREMENTS

In order to derive the flow-diameter relation Doriot et al. [Doriot-00] kindly provided us with the diameter and flow information of human coronary arteries. The measurements are in detail described by Doriot et al. We will give a summary: In 21 patients that were undergoing cardiac catheterization for various cardiac diseases, blood flow velocity measurements were performed in 36 angiographically normal bifurcations. In these bifurcations the peak velocity over 2 cardiac cycles was measured and averaged in the mother branch M, as well as in the larger daughter branch D1 and the smaller daughter branch D2. The corresponding cross-sectional areas were determined by 3D analysis of bi-plane angiography [Guggenheim-91]. From this data the flow and diameter for each branch was calculated assuming a parabolic flow profile and circular vessel area. The 18 bifurcations with the best imaging quality and flow measurements were selected for further analysis.

ANALYSIS

Based on the data provided by Doriot et al., two fits were performed. With the first fit the relationship between diameter and flow was obtained. If Murray's Law holds, or similarly if a Poiseuille flow is assumed with constant viscosity and equal WSS in all branches, then the flow is proportional to the cubed diameter. Therefore the flow q [m³/s] and diameter d [m] of the 54 (18 times 3) branches was fitted to the equation

$$q = k \cdot d^x \qquad \qquad \text{EQUATION 8-3}$$

by non-linear regression (Matlab 7.1, The MathWorks Inc.), with x [-] as the unknown power term and k [m³⁻ˣ/s] as constant.

A second fitting procedure was performed to obtain the relationship between the diameter ratio of the daughter branches and the flow ratio through these branches. The flow ratio and the diameter ratio of the 18 bifurcations were fitted to the equation:

$$\frac{q_{D2}}{q_{D1}} = \left(\frac{d_{D2}}{d_{D1}} \right)^x$$

EQUATION 8-4

with the x [-] as the unknown power term. This relation will be referred to as Doriot's Fit. Under the same assumptions as for the first fit, this relationship would result in equation 2, with 3 as the value for the unknown power term.

For both regressions the R^2, and the 95% confidence interval (CI) of the estimated parameters were determined.
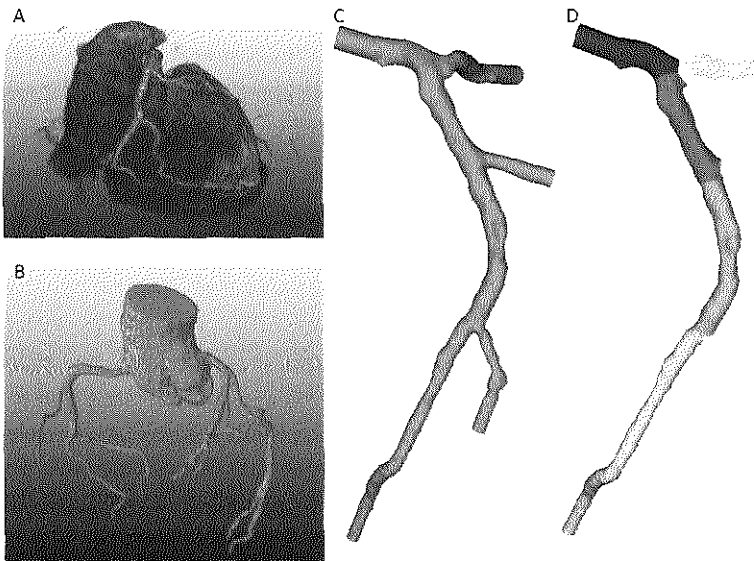
FIGURE 8-1: Panel A shows the segmentation of the coronary arteries in the original CT scan. The complete segmented tree can be seen in panel B. This geometry is clipped (panel C), and the in,- and outflow tracts are extended with circular tubes to aid the WSS calculations. The geometry is divided in segments (panel D).

8.2.2   WSS CALCULATIONS IN CORONARY BIFURCATIONS

IMAGE ACQUISITION

We retrospectively selected coronary CT angiography datasets of patients that were scanned with a 64-slice CT scanner (Sensation64®, Siemens, Germany) in our institution. A detailed description of the patient preparation, scan protocol and image reconstruction has previously been described [Mollet-05]. Briefly, a contrast enhanced scan (Iomeron 400®, Braco, Italy) was performed according to a standardized optimized contrast-enhanced scanning protocol. The initiation of the scan was synchronized to the arrival of contrast in the coronary arteries by a bolus-tracking technique. The images taken during the mid-to-end diastolic phase (350 ms prior to the R-wave) were reconstructed with a temporal window of 165 ms. This resulted in datasets with an almost uniformly sized voxelspace of 0.35 by 0.35 by 0.4 mm.

SEGMENTATION AND PREPROCESSING

We selected 10 coronary datasets that were judged as good quality CT scans (i.e. no moving artifacts, good contrast enhancement) by an experienced radiologist. The lumen of the coronary tree was segmented with dedicated CT image processing software (Leonardo, Siemens, Germany) Siemens. The segmentation was based on intensity thresholds resulting in a binary voxelspace (see Figure 8-1A and B). We selected the three best segmented right coronary artery trees and three left coronary artery trees, based on the completeness of the main artery and side branches. These binary coronary trees were converted into a surface and smoothed with the aid of imaging processing software (Mevislab, Mevis, Bremen, Germany). The surfaces were exported to the Vascular Modeling Toolkit (www.vmtk.org) to prepare the geometries for computational fluid dynamics (CFD). To reduce computational cost the coronary tree geometries were clipped at the side-branches such that only the main artery and a short part of the side-branches remained. To allow for prescription of in and outflow conditions, the inflow tract and all outflow tracts were extended with circular tubes in the direction of the centerline (Figure 8-1C). Subsequently the coronary tree geometry was divided into segments (see Figure 8-1D) [Antiga-04] and the average diameter of each segment and side-branch was calculated.
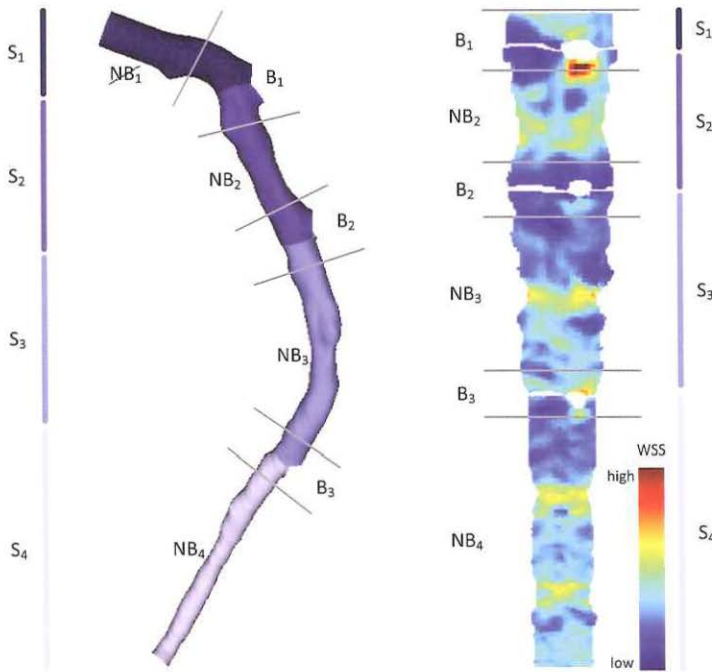
FIGURE 8-2: Left: For the analysis of the WSS the side-branches are removed from the geometry. Besides the segments (S_1-S_4), bifurcation regions (B_1-B_3) and non-bifurcation regions (NB_1-NB_4) are defined. Right: The same regions are now depicted in the 2D WSS map of the same artery. Non-bifurcation region NB_1 does not exist because the inlet was too short

COMPUTATIONAL FLUID DYNAMICS

A volume mesh was created from the geometries and discretized into linear tetra-hedral volume elements with Gambit 2.4.6 (Ansys, Inc., USA). The number of elements in the geometries varied between 0.6-2.5 million and the number of nodal points between 107-436 thousand. For the CFD calculations the blood was modeled as an incompressible non-Newtonian fluid with a density of 1050 kg·m^{-3} (Carreau model with time constant = 25 s, power law index = 0.25, zero-viscosity = 0.25 kg/m-s and infinity-viscosity=0.0035 kg/m-s) [Seo-05]. The arterial wall was assumed to be rigid and with no-slip conditions at the wall. At the inlet and all outlets except for

1, a parabolic velocity profile was prescribed. At the remaining, most distal, outflow tract, a traction free boundary condition was applied. The solution was considered converged when the relative error in both the pressure and the velocities in all directions were lower than 10^{-3} (FIDAP 8.7.4, Fluent Inc. Products, ANSYS,Inc. USA).

<u>INFLOW AND OUTFLOW CONDITIONS</u>

The maximum velocity in the parabolic inlet profile was computed from the averaged diameter of the inflow segment and Doriot's Fit (Equation 8-3). Two different models were applied to determine the flow ratio through the daughter branches: 1) Murray's Law (Equation 8-1) and 2) Doriot's Fit, the experimentally derived flow-diameter ratio (Equation 8-4) based on the data of Doriot et al. The averaged diameters of the two daughter branches at each bifurcation served as input for these equations. Once the flow ratio was known, the flow through the side-branch could be calculated and prescribed to the outflow tract by a parabolic velocity profile. Thus for each geometry two WSS distributions were obtained: one derived using Murray's Law (WSS_M) and one derived using Doriot's Fit as outflow condition model (WSS_D).

8.2.3   ANALYSIS

<u>NON-BIFURCATION REGIONS</u>

For the analysis different regions were defined (see Figure 8-2). We defined segments $S_{1,2...,n+1}$, with n number of side-branches. S_1 starts at the inflow, until the first side branch, $S_{2,3...,n}$ are between side-branches and segment S_{n+1} starts from the last side branch until the outflow tract. Non-bifurcation regions $NB_{1,2...,n+1}$ are that part of a segment $S_{1,2...,n+1}$ minus one time its diameter from the downstream part (for NB_1-NB_n) and minus one time its diameter from the upstream part (for NB_2-NB_{n+1}) (Figure 8-2). If the segment was too small for this operation, than this segment had no non-bifurcation region. We compared the WSS_M and WSS_D in the non-bifurcation regions and related this to the prescribed flow through these regions.

<u>BIFURCATION REGIONS</u>

The segment regions not included in the set of non-bifurcation regions were defined as the bifurcations regions $B_{1,2...,n}$ (Figure 8-2). We compared the size and location of the low WSS areas of WSS_M and WSS_D in the bifurcation regions. We defined two WSS cut-off values for each bifurcation region. The first cut-off value (CO_M) is

determined by taking the 25 percentile WSS value of the WSS_M. The second cut-off value (CO_D) the 25 percentile WSS value determined from the WSS_D. Areas with a WSS lower than the cut-off value are called the low WSS area (LWA). From the WSS_M we determined the location and area of the LWA's based on the CO_M (LWA_{MM}). For the WSS_D we determined the area and location of the LWA's both with CO_M (LWA_{DM}) and CO_D (LWA_{DD}). First we compared the LWA_{MM} versus the LWA_{DM} on area size and overlap. Next we investigated the same parameters for the LWA_{MM} versus the LWA_{DD}. Linear regression and Bland-Altman analysis and were used to compare the area size. The overlap of the areas was defined as:

$$overlap_{DM} = \frac{2 \cdot |LWA_{MM} \cap LWA_{DM}|}{LWA_{MM} \cdot LWA_{DM}} \cdot 100\% \qquad \text{EQUATION 8-5}$$

and similar for the $overlap_{DD}$ between LWA_{MM} and LWA_{DD}. The overlap percentages are compared with a Wilcoxon Rank test (p<0.05 was considered significant).

8.3   RESULTS

8.3.1   FLOW-DIAMETER RELATION

Based on the data provided by Doriot et al. [Doriot-00] we derived two relations; between the diameter of the coronary branch and the flow through it and between the diameter ratio of two daughter branches and the flow ratio through the branches.

The relation between flow and diameter fitted (Equation 8-3) very well (R^2=0.87), with the constant k of 1.43 $m^{0.45}$/s (95% CI: -0.81 to 3.69) and the power term x of 2.55 (95% CI: 2.27 to 2.83) resulting in Equation 8-6. Figure 8-3A shows the measured data with the fit.

$$q = 1.43 \cdot d^{2.55} \qquad \text{EQUATION 8-6}$$

The results of the non-linear regression for flow ratio and diameter ratio (Equation 8-4) are depicted in Figure 8-3B. The power term x was 2.27 (95% CI: 1.58 to 2.96) resulting in Equation 8-7. The fit produced an R^2 of 0.70.

$$\frac{q_{D2}}{q_{D1}} = \left(\frac{d_{D2}}{d_{D1}} \right)^{2.27} \qquad \text{EQUATION 8-7}$$
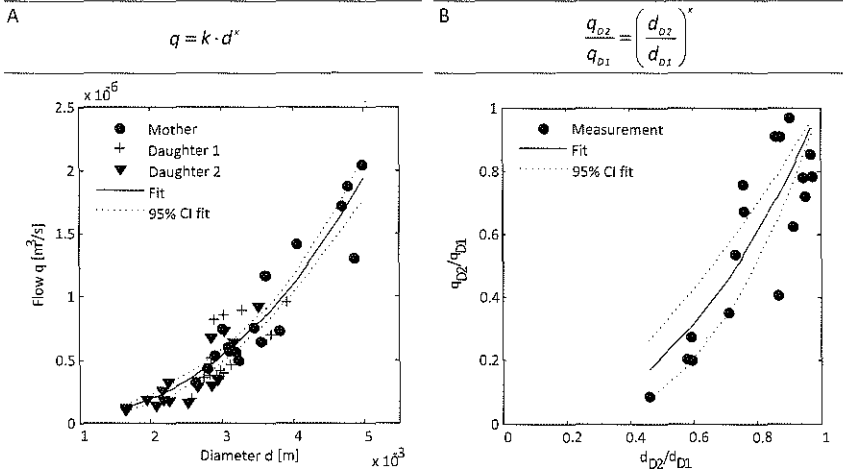
FIGURE 8-3: Results of the fitting procedures on data of Doriot et al. On the left (panel A) the relationship between the flow and the diameter of the artery is fitted (Equation 8-3). On the right (panel B) the relationship between the flow ratio and diameter ratio of the smaller daughter branch D2 and larger daughter branch D1 is fitted as described by Equation 8-4.
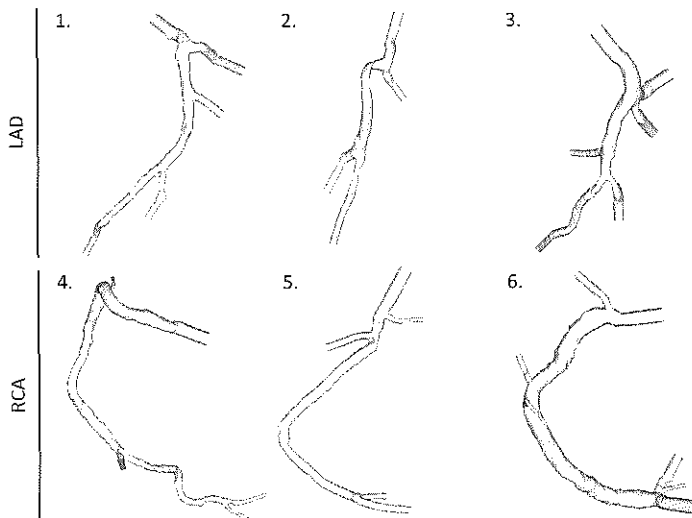
FIGURE 8-4: The six geometries in which the WSS for different outflow condition models are calculated. Geometry 1-3 are left anterior descending coronary arteries (LAD's) and 4-6 are right coronary arteries (RCA's).

8.3.2 WSS CALCULATIONS

For six coronary arteries from 5 patients , 3 left anterior descending arteries (LAD) and 3 right coronary arteries (RCA), we calculated the WSS with the two different outflow conditions models, one based on Murray's Law (Equation 8-2), WSS_M, and the other based on the derived flow-diameter ratio of Doriot (Equation 8-7), WSS_D. The geometries of these arteries are depicted in Figure 8-4. Of the 6 arteries, 4 had

TABLE 8-1: Geometry characteristics and boundary conditions

| | | Diameter (mm) | | | Flow (ml/min) | | | |
| | | | | | Murray's Law | | Doriot's Fit | |
Geometry	Bifurcation	M	D1	D2	M	D2	M	D2
1	1	3.45	3.77	3.30	45.0	18.0	45.0	19.1
	2	3.77	3.32	2.59	27.0	8.7	25.9	9.4
	3	3.32	2.37	2.09	18.3	7.5	16.5	7.1
2	1	2.81	2.83	2.11	26.7	7.8	26.7	9.0
	2	2.83	2.09	2.03	18.9	9.1	17.7	8.6
3	1	4.73	5.07	3.53	101.0	25.4	101.0	30.8
	1a	5.07	3.58	3.13	75.6	30.2	70.2	29.7
	2	3.58	2.44	2.36	45.4	21.5	40.5	19.4
	3	2.44	2.44	2.36	23.8	11.3	21.0	10.1
4	1	5.20	3.98	1.30	128.5	4.3	128.5	9.3
	2	3.98	2.90	2.50	124.2	48.3	119.2	49.5
	3	2.90	1.86	1.56	75.9	28.1	41.8	27.9
5	1	4.72	3.68	1.87	100.4	11.6	100.4	17.7
	2	3.68	3.37	2.58	88.8	27.5	82.7	29.1
	3	3.37	2.49	1.97	61.3	20.3	53.5	19.8
6	1	4.77	5.45	2.56	103.4	9.7	103.4	15.7
	2	5.45	4.85	2.52	93.8	11.5	87.7	16.2
	3	4.85	5.19	1.84	82.2	3.5	71.5	6.2
	4	5.19	4.67	3.35	78.7	21.2	65.3	20.9
	5	4.67	4.52	1.66	57.5	2.7	44.4	4.1

- M is the mother branch, D1 is daughter branch 1, D2 is daughter branch 2;
- Daughter 2 is always the smaller daughter branch;
- The prescribed flow in the CFD calculations are underlined;
- Geometry 3, Bifurcation 1.a is part of a trifurcation. For the analysis it is treated as 1 bifurcation region together with bifurcation 1.

3 side-branches, one artery had 4 and one artery had 5 side-branches. The LAD geometry with 4 side-branches had two side-branches so close to each other that they were considered as a single bifurcation region in the analysis. The averaged diameters and the prescribed flow through the segments and side-branches are summarized in Table 8-1. As can be expected based on the results of the Doriot's Fit, the total flow through the side-branches was higher when prescribing outflow conditions according to Doriot's Fit versus Murray's Law, resulting in a lower flow through the main branch. The resulting WSS distribution and analysis are illustrated in detail for geometry 1 (an LAD with 3 side-branches) and summarized for the other geometries.

8.3.3   EFFECT OF OUTFLOW MODELS IN NON-BIFURCATING REGIONS

For geometry 1 the WSS_M is shown in Figure 8-5. The first side branch is the LCX, which has a large diameter. As a consequence, we see a low wall shear stress region opposite of the flow divider. Further downstream, the local lumen narrowing results in increased WSS values. Since this is a relatively straight segment, no pronounced effect of the curvature is observed. The WSS slightly increases from proximal to distal. Based on Doriot's Fit a higher percentage of the flow is directed through the side-branches. This results in a lower flow and thus lower WSS_D than WSS_M in the main branch. For geometry 1 the average WSS_M was 0.26 Pa (95% CI: 0.08-0.51 Pa) and 0.25 Pa (95% CI: 0.07-0.48 Pa) for WSS_D, with maxima of 1.02 Pa and 0.98 Pa, respectively, downstream of the most proximal bifurcation. Figure 8-5B depicts the difference in WSS_M and WSS_D relative to WSS_M. The relative difference between the two models ranged from -14.4% to 17.1% and is most pronounced near the bifurcation regions. In between the bifurcation regions this relative difference is fairly constant and scales very well with the difference in flow through the segment. In Figure 8-5D the relative difference in WSS averaged along the length of the artery and the relative difference in flow are depicted; they correspond well. Figure 8-5C shows the relative differences in WSS from which the relative difference in flow is subtracted in the 2D map of the artery. This illustrates that the WSS scales with the flow in the non-bifurcation regions, but not near the bifurcations.

In the 6 arteries, 25 segments were defined. Five segments were too short to define a non-bifurcation region. The WSS_M and WSS_D are presented in Table 8-2 as well as the differences and relative differences in WSS and flow through these non-bifurcation regions. The averaged relative difference between WSS_M and WSS_D in the

non-bifurcation regions can be fairly large and ranges from -5.1% to 27.4%. The relative difference in WSS (column 5) and flow (column 6) were in each non-bifurcation region equal to each other (paired t-test, p>0.05). Linear regression supported that the relative differences in flow and WSS in the non-bifurcation regions were equal (R^2= 0.96, slope=1.08 and offset = 0.01).
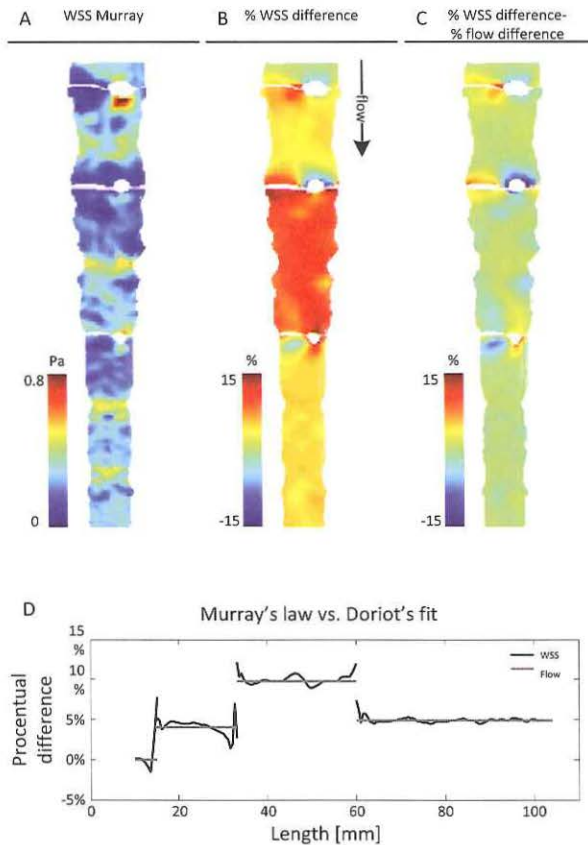
FIGURE 8-5: Panel A shows the WSS_M mapped into 2D. In panel B the relative difference between the WSS_M and WSS_D is depicted. It shows that the relative difference is very constant outside of the bifurcation regions. Panel C and D demonstrate that the relative difference in WSS is close to the relative difference in flow through the branch. In Panel C the relative difference in flow is subtracted from the relative difference in WSS. Between the bifurcation this results in values close to 0%. In Panel D the relative difference in WSS is averaged over the circumference and plotted against the length of the artery.

8.3.4 EFFECT OF OUTFLOW MODELS NEAR BIFURCATIONS

Figure 8-6 shows the WSS_M and WSS_D in the three bifurcations regions for geometry 1. Bifurcation 1 and 2 both have a high WSS region at the carina of the bifurcation. Bifurcation 3 also has a high WSS region, but at the proximal side of the side-branch. The low WSS area's are found at the opposite site of the side-branch in bifurcations 1 and 3. In bifurcation 2 several low WSS regions are found. Qualitatively the WSS_M and WSS_D look similar. The LWA_{MM} is depicted in the WSS_M distribution, the LWA_{DM} and LWA_{DD} are depicted in the WSS_D. The difference in LWA is most prominent in
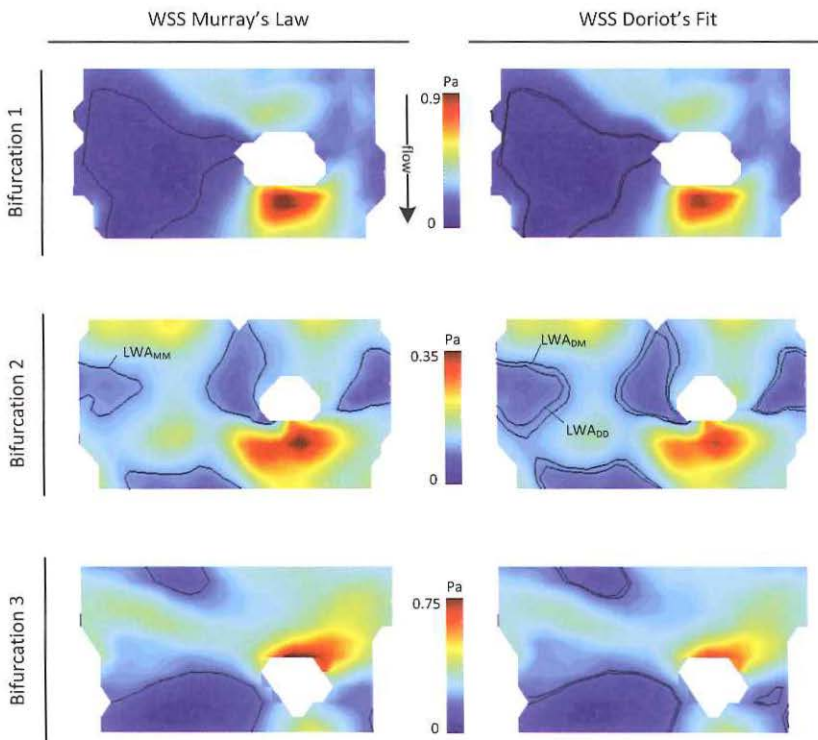
FIGURE 8-6: On the left side the WSS distribution is depicted as calculated with Murray's Law as outflow model for the 3 bifurcations regions of geometry 1 (WSS_M). On the right the same bifurcation regions but now depicted with the WSS as calculated with Doriot's Fit (WSS_D). Note that the WSS color bars are different for the different bifurcations. For each bifurcation in the left panel, LWA is delineated as determined based on the cut-off value calculated from the Murray's WSS distribution, LWA_{MM}. In the right panels the area is depicted in the Doriot's WSS distribution with the same cut-off value (LWA_{DM}) and with the cut-off value determined by Doriot's WSS distribution LWA_{DD}

bifurcation 2, and especially the LWA opposite of the side-branch differs in size and shape. The CO_M is 0.10 Pa and if we compare the LWA for both models than the LWA_{MM} is 23 mm² and the LWA_{DM} and 29 mm² with an overlap of 70.3%. It is to be expected that if you take the same CO_M for both WSS distributions that the LWA_{DM} is larger than the LWA_{MM}, since Doriot's Fit defined more flow through the side-branches. However if we base the cut-off value on the local WSS than the CO_D is 0.09 Pa, and we find a better agreement since the LWA_{DM} is almost equal to the LWA_{MM} with 23 mm² and an overlap of 92.6%. Thus, if the cut-off value is relative to the local WSS values, than the LWA's hardly differ.

TABLE 8-2: Results WSS and flow difference at the non-bifurcation regions

Geometry	NB Region	WSS [Pa]				Flow
		WSS_M	WSS_D	Difference	% Difference	% Difference
1	2	0.29	0.28	0.01	4.3%	4.0%
	3	0.23	0.21	0.02	9.6%	9.8%
	4	0.29	0.28	0.01	4.8%	4.9%
2	1	0.37	0.39	-0.02	-5.1%	0.0%
	2	0.38	0.34	0.04	9.4%	6.6%
	3	0.53	0.50	0.03	6.0%	5.7%
3	1	0.48	0.48	0.00	-0.1%	0.0%
	2	0.38	0.33	0.05	12.4%	10.8%
	3	0.59	0.51	0.08	13.1%	11.9%
	4	0.40	0.36	0.04	10.2%	12.9%
4	1	0.60	0.60	0.00	0.1%	0.0%
	2	1.19	1.14	0.06	4.4%	4.1%
	3	1.97	1.79	0.19	8.9%	8.2%
	4	2.10	2.09	0.01	-1.6%	0.6%
5	2	0.75	0.68	0.07	8.0%	6.9%
	3	0.86	0.74	0.12	13.8%	12.7%
	4	1.36	1.11	0.25	18.2%	17.8%
6	2	0.31	0.30	0.02	4.8%	6.5%
	4	0.29	0.23	0.06	18.1%	17.0%
	6	0.29	0.21	0.08	27.4%	26.5%

That this holds for all bifurcation regions is depicted in Table 8-3 and Figure 8-7. In Table 8-3 the LWA_{MM}, LWA_{DM} and LWA_{DD} and $overlap_{DM}$ and $overlap_{DD}$ are summarized for all bifurcation regions. The linear regression between LWA_{MM} versus LWA_{DM} was not as good as for LWA_{MM} versus LWA_{DD} ($R^2=0.87$ versus $R^2=1.00$). The Bland-Altman analysis showed that the LWA_{DM} was on average 4.7 mm² larger than the LWA_{MM}, but that the LWA_{DD} and LWA_{MM} were equal in size (paired-t-test, p=0.89). The overlap between LWA_{MM} and LWA_{DD} (94 ± 5%) was also significantly larger than the overlap between LWA_{MM} and LWA_{MD} (74% ± 15%) (Wilcoxon rank test, p<0.05). The high overlap in LWA shows that the location of the LWA does hardly differ between the 2 outflow condition models.

TABLE 8-3: Results of the low WSS area's (LWA) at the bifurcations regions

Geometry	Bifurcation	Total area [mm²]	LWA [mm²] LWA_{MM}	LWA [mm²] LWA_{MD}	LWA [mm²] LWA_{DD}	Overlap$_{MD}$	Overlap$_{DD}$
1	1	101	24	26	24	89.5%	98.2%
	2	92	23	29	23	70.3%	92.6%
	3	54	14	16	14	87.4%	97.2%
2	1	58	13	13	12	81.1%	82.6%
	2	51	11	14	11	68.5%	92.4%
3	1	121	30	35	30	77.9%	94.3%
	2	86	20	26	20	70.1%	98.4%
	3	47	12	18	12	54.1%	97.3%
4	1	141	35	34	32	93.7%	91.8%
	2	71	17	18	17	91.9%	99.1%
	3	35	8	9	9	82.1%	92.7%
5	1	90	22	34	21	48.9%	82.0%
	2	79	20	26	21	66.2%	92.8%
	3	54	12	15	12	73.4%	96.0%
6	1	162	41	37	42	99.1%	89.0%
	2	174	43	51	43	78.4%	95.0%
	3	180	45	56	45	71.3%	97.2%
	4	110	29	44	29	51.8%	94.8%
	5	83	22	32	22	57.2%	98.5%

LWA_{MM}: Low wall shear stress area calculated with Murray's Law and the cut-off (CO) value calculated on this Murray's distribution.
LWA_{MD}: LWA calculated with Doriot's Fit and the CO calculated on Murray's distribution.
LWA_{DD}: LWA calculated with Doriot's Fit and the CO value calculated on Doriot's distribution.
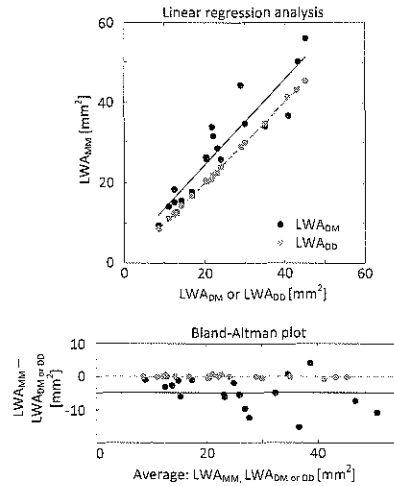
FIGURE 8-7: Comparison of the low wall shear stress areas in the bifurcation regions as calculated for Murray's Law as outflow condition model (LWA_{MM}) versus the low WSS areas based on the WSS distribution calculated by Doriot's Fit with cut-off value based on Murray's distribution (LWA_{DM}) or based on Doriot's distribution (LWA_{DD}). The linear regression is shown with the original data points and the Blant-Altman analysis. It shows that the LWA_{MM} and LWA_{DD} are not different.

8.4 DISCUSSION AND CONCLUSIONS

MSCT is a promising non-invasive imaging technique that can provide the geometry of the coronary arteries to calculate WSS with computational fluid dynamics in the bifurcation regions. However, MSCT angiography does not provide any hemodynamic information that can be used to prescribe the in,- and outflow boundary conditions. We provide a model to estimate these boundary conditions based on the local geometry. The inflow into the artery was estimated based on a relationship that was derived from the measured flow and diameter data of Doriot et al. This allows thus to prescribe the flow through the artery based on the inlet diameter of geometry. To estimate the outflow at the side-branches it is common to use Murray's Law, which states that the flow division over two branches equals the ratio of the diameters to the power 3. However, this cubed power might be too large since lower values are found in literature and also in this study we found a value of 2.27. We studied the effect of different outflow conditions (Murray's Law and Doriot's Fit) on the WSS distribution and showed, although the differences were sometimes large, that the WSS scales outside the bifurcation regions with the prescribed flow through the branch. In the bifurcation regions the LWA's differed in size between

the two outflow condition models when an absolute cut-off value was chosen to determine LWA, however, when the cut-off value was chosen relative to the WSS distribution of each of the models, the LWA's were equal in size and location for both outflow condition models.

To estimate the inlet flow for our 6 vessel geometries based on the inlet diameter we used the relation we found between diameter and flow based on the data of Doriot et al. On average the estimated flow was 84 ml/min. This value is within the range reported in literature (88 -141 ml/min [Aarnoudse-07, Bloch-09, Wellnhofer-09]). However, the mean WSS found in our study is 0.68 Pa, in which is lower than the wide range of values that are generally used in studies which the inlet flow is estimated (1.4 Pa – 17.7 Pa [Wentzel-05, Saihara-06, Soulis-06, Gijsen-07]). Our mean WSS value is within the range WSS values calculated from measured flow data (0.46 – 1.24 Pa [Gijsen-03, Gijsen-08]). Therefore it seems to be appropriate to use our proposed fit in future studies when flow data is lacking.

Aside from the inflow, also boundary conditions need to be prescribed to regulate the outflow through the side-branches of the coronary artery to calculate accurate WSS. Murray's Law is most often applied to determine the flow ratio over the daughter branches [Joshi-04, Soulis-06, Gijsen-07]. However, reports on the geometry of human coronary arteries find a lower power value than the third power of Murray's Law [VanBavel-92, Finet-08]. To our knowledge we are the first that determined in humans the relationship between diameter ratio and flow ratio of the daughter branches. We found also a lower power value of 2.27. Since both literature based on geometry and our data come up with a lower power value, it is more appropriate to prescribe higher flow rates through the side-branches than those derived from Murray's Law, for instance using Doriot's Fit. This will result in lower flows through the main-branches, and thus lower Reynolds numbers.

The choice of different outflow boundary condition models results in different time-averaged WSS values. Between side-branches the averaged WSS can differ up to 20% and local differences are even higher depending whether you prescribe Murray's Law or Doriot's Fit. So, for studies interested in absolute WSS, Doriot's Fit is preferable over Murray's Law. However, we showed that outside of the bifurcations regions the relative difference between the two models scales with the flow. In the bifurcations regions the WSS does not scale with the flow. However, the low WSS

regions are equal in size and position when the cut-off value is based on the local WSS values. Thus if no flow measurements are present, different outflow condition models will result in different absolute WSS values, but when relating normalized WSS to atherosclerosis, comparable results can be obtained.

When studying atherosclerosis in the coronary arteries, a wide variety of disease can be present, from early atherosclerosis with no flow limiting effect to the more advanced phases of the disease with highly stenotic plaques. The data we used for the fitting of the flow diameter relations is obtained in patients with coronary artery disease, but in angiographically normal segments. Therefore, the boundary condition models presented in this paper might not be applicable for more diseased arteries. More volumetric flow measurements in different parts of the coronary tree in different patients groups and also including the severity of the disease into the model, might improve the proposed models. Unfortunately, when intravascular Doppler measurements of coronary flow are performed, often only maximum velocity is reported without the corresponding diameter at the measured location. Instead of Doppler measurements, for future research the choice for intravascular thermodilution [Aarnoudse-07] might be better, since it provides the volumetric flow without necessary estimations of the coronary size and velocity profile.

In this study we prescribed flow at the outflow tracts as estimated based on geometry. However, the flow through the side-branches is physiologically determined by the resistance of the vascular bed distal to the side-branch. Based on mathematical generation of coronary tree models the resistance and flow through the arteries can be modeled [VanBavel-92, Kaimovitz-05, Huo-07, Molloi-07]. These models can increase the insight into the flow division over the bifurcations. In contrast to these geometrical models, also lumped parameters models can be modeled to represent the vascular bed. Recently, methods are developed to mathematically couple these lumped parameter models to the outflow tracts of the side-branches of a 3D modeled aorta [Olufsen-99, Mittal-05, Huo-07]. In the coronary arteries, however, not only the properties of the vascular bed but also the contraction of the heart muscle will influence the flow. More complex models of coronary flow exist [Bovendeerd-06], but these are not yet coupled to 3D models for CFD calculations. These models of increasing complexity have great potential to mimic the time-dependent flow and thus time-dependent WSS in the coronary arteries with increasing physiological reality. However, also patient specific measurements at several locations in the coronary arteries and in different stages of disease will be necessary to determine the parameters in such models.

Besides increasing complexity in prescribing the boundary conditions, also the complexity of the 3D model can be increased. In this study we choose a static, non compliant 3D model of the coronary arteries in which we calculated time-averaged WSS. Several papers have investigated the effect of these simplifications in a numerical way [Prosi-04, Ramaswamy-04, Pivkin-05, Zeng-08]. These studies show that simplifications of the 3D model do influence the WSS values; however, how the simplification will influence the findings on the relation between WSS and atherosclerosis is still unknown, since in most clinical studies that relate WSS to atherosclerosis the WSS values are normalized or averaged in the spatial domain.

The complexity of models to calculate WSS should also be considered in light of the accuracy of the current imaging techniques. Assessing the geometry non-invasively by accurate segmentation of the coronary lumen from CT angiography is still a challenge, but accurate wall assessment is even more complex. It would be interesting to study how accurate the generated geometry and model assumptions have to be for different type of studies on WSS and atherosclerosis.

Apart from MSCT the coronary arteries can also be non-invasively assessed by MRI. Although the acquisition times of cardiac MRI are long and the spatial resolution is still limited, MRI might be a future competitor to MSCT for WSS analysis since the acquisition is without radiation and progress is being made in contrast enhanced plaque imaging and in coronary flow measurements [Bloch-09].

In conclusion, when patient specific boundary conditions for WSS computations in coronary trees are lacking, an estimation of the flow rates is necessary. Based on patients-specific flow data, we proposed an empirical relationship that relates the local geometry to flow rates through the main and side-branches. When applied as boundary conditions, the proposed relationship reveals lower flow rates through the main branch than based on the common applied Murray's Law. As a consequence the absolute WSS values are lower in the main branch. However, the choice of boundary condition has limited influence when studying normalized WSS as is common in atherosclerosis research.

General discussion

This last chapter starts with a summary of the previous chapters, which is followed by the discussion of this thesis. First the current and future role of computer tomography (CT) in clinical practice, and in the assessment of wall shear stress and atherosclerosis is addressed. Next the, in this thesis frequently applied, fusion technique of CT and intravascular ultrasound (IVUS) is discussed for its application in the validation of CT versus IVUS, on the one hand, and, on the other hand, to study the relation between wall shear stress (WSS) and atherosclerosis. In the last part the potential of WSS as clinical parameter is discussed; what is possible at this moment, what are the challenges and what steps have to be taken before WSS can become a clinical important parameter? This last chapter ends with the conclusions of this thesis.

.
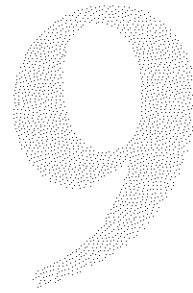
9.1 SUMMARY

Wall shear stress (WSS), the drag force induced by the blood flow on the vascular wall, is an important factor in the localization of atherosclerosis [Caro-71, VanderLaan-04]. Despite its small value in comparison to the blood pressure, WSS influences many biological responses, which are triggered by the endothelial cells [Malek-99]. As WSS changes due to plaque growth, different biological responses kick in and as a consequence influence plaque composition and progression [Slager-05]. More insight in the development of atherosclerosis can contribute to the prevention and treatment of coronary atherosclerosis disease, which is still the number one cause of death in the developed countries. Because of the importance of WSS in atherosclerosis processes, this biomechanical parameter is extensively studied in vitro and in vivo in animals and patients. To assess WSS in patients the 3D geometry of the coronary lumen is needed [von Birgelen-95, van der Giessen-09]. Information about the atherosclerotic plaques have to be assessed in-vivo to relate the WSS to the extent of atherosclerosis. Intravascular ultrasound (IVUS) is the gold standard imaging technique to determine lumen and plaque information. Unfortunately IVUS is an invasive imaging technique, which limits wide application in patients. Thus, there is a need for a non-invasive alternative to study WSS and atherosclerosis in patients.

In the last decade the temporal and spatial resolution of computed tomography (CT) angiography have greatly improved. CT is a non-invasive 3D imaging technique and might therefore be a good alternative for IVUS to assess the 3D geometry of the coronary lumen. Also the coronary wall can be visualized by CT, thus the relation between coronary WSS and atherosclerosis might be assessable with CT. The aim of this thesis was to explore how coronary CT angiography can be applied to study the relation between WSS and atherosclerosis as stand-alone non-invasive imaging technique or in combination with invasive imaging techniques.

In Chapter 2 we related the presence of atherosclerosis to WSS in coronary bifurcations with CT as stand-alone imaging technique. Regions of high and low WSS were discriminated based on the geometry of the bifurcation and these regions were inspected on the presence of atherosclerosis. This study confirmed that atherosclerosis was mainly localized in the low WSS regions, i.e. the outer wall of the bifurcation. We also showed that plaque was found in the high WSS sensing carina when the atherosclerosis was more progressed. Thus, WSS and atherosclerosis can be studied in a qualitative way with CT angiography.

To quantitatively study WSS and atherosclerosis in the coronary arteries with the aid of CT, a reconstruction technique to generate patient specific 3D geometries of the lumen and wall by aligning 2D IVUS derived lumen and wall contours on a 3D CT derived centerline is presented in Chapter 3. We demonstrated the possibilities and robustness of this technique to correlate WSS and atherosclerosis quantitatively. Since this technique establishes the registration between CT and IVUS, cross-sectional CT images can be compared to IVUS images as well as CT derived contours versus IVUS contours to validate CT against the gold-standard IVUS. This validation is important since the possibilities of CT in WSS and atherosclerosis research depends on the accuracy of CT.

In Chapter 4 the reconstruction technique is used to compare CT against IVUS. The accuracy to detect and classify plaques with CT in ex-vivo imaged human coronary arteries was assessed. This study demonstrated that plaque detection and classification is hard. The inter-observer variabilities were large, calcifications hindered the assessment of the non-calcified part of a plaque, and non-calcified plaques could only reliably be detected if the wall was thicker than 1 mm. Also calcifications were not always detectable with CT. In-vivo comparison of CT and IVUS in Chapter 5 demonstrated that only larger calcifications in the coronary wall can be detected with CT, but that the smaller ones are missed. The detection and classifications of different plaque types and components with CT thus remains a challenge.

Chapter 6 and 7 show the possibilities of CT in combination with an invasive imaging modality to study WSS and atherosclerosis quantitatively. The reconstruction technique is applied in Chapter 6 to relate WSS and plaque rupture location. Small ruptures were mainly found upstream at the shoulders of the plaque and the WSS at the rupture location was on average higher than the WSS over the plaque. The association between elevated WSS and plaque rupture supports the hypothesis that high WSS in advanced atherosclerosis, destabilizes the plaque. A case report in Chapter 7 illustrates that the 3D reconstruction technique is not limited to IVUS contours alone, but that any invasive 2D imaging technique can be placed into 3D with the aid of CT as long as side branches can be identified. In this case report the lipid content in the coronary wall as derived by near-infrared IVUS was placed into 3D together with the IVUS wall and lumen contours, such that WSS could be shown in relation to the lipid content in the wall.

In the main coronary arteries side-branch locations are predilection sites of atherosclerosis and therefore interesting regions to study the relation between WSS and atherosclerosis. In contrast to IVUS, CT has the capability of imaging all the larger coronary arteries simultaneously, thus not only the main branch, but also the large side-branches. Calculating the WSS in geometries with side-branches requires prescription of boundary conditions at the side-branch locations in order to divide the flow over the different branches. Since CT does not come with hemodynamic measures, estimations have to be made for this outflow conditions. In Chapter 8 two models that estimate the flow division based on the available geometry are compared with respect to the influence on the WSS distribution. One model was based on an energy balance and one model was derived from data in the literature. The choice of model influenced absolute WSS; however relative WSS measures were hardly influenced by the choice of the model. These insight are useful once coronary artery geometries with side-branches will be available either from CT as stand-alone imaging technique or from the combination of IVUS and CT.

9.2   CORONARY CT ANGIOGRAPHY

First, the current and future clinical role of CT to assess the extent of coronary artery disease will be discussed. Next, we will discuss the potentials of coronary CT angiography as stand alone imaging technique to provide and relate WSS and atherosclerosis.

9.2.1   CLINICAL APPLICATION

Significant lumen stenosis in human coronary arteries can reliably and non-invasively be assessed with coronary CT angiography [Bastarrika-09]. However CT can be used in more ways to determine the extent of coronary artery disease. Initial observations demonstrate good accuracies to determine myocardial perfusion defects [Ruzsics-08], and studies are currently executed to evaluate CT stress testing [George-09] and the determination of myocardial viability [Nikolaou-05]. However, it is still unclear how CT as a technique that can assess coronary anatomy, function, perfusion and viability, should become clinically incorporated with nuclear imaging, stress testing and traditional angiography. Yet, from a patient perspective a technique that can do all-in-one with less radiation dose than two or more separate techniques would be very favorable.

CT angiography has to prove its benefits against other diagnostic modalities, in terms of patient outcome [Min-08, Pundziute-07] and cost-effectiveness [Dewey-07, Stillman-07]. At this moment the most promising role of CT angiography is seen as a frontline test in the diagnostic path of coronary artery disease, because high predictive values are obtained to rule out coronary disease [Lesser-07, Min-08]. Since a trend is noticeable towards medical treatment, instead of invasive interventional procedures as the core of coronary artery disease management [Tommaso-08], CT might develop into a screening tool for asymptomatic patients with increased risk for coronary artery disease. In addition, research on risk-stratification of different patients groups based on CT angiography findings in combination with the technical refinements of CT (lower radiation dose, higher resolution) also suggest that high-risk patients could benefit of CT angiography to determine the level of medical risk management and its success [Shaw-08].

9.2.2 WALL SHEAR STRESS ASSESSMENT

The clinical success of CT for the assessment of coronary artery disease was the reason to investigate the possibilities of CT angiography to provide the 3D lumen geometry for patient specific coronary WSS analysis. The accuracy of WSS simulations depends on, among other factors, the quality of the CT-derived lumen geometry, since WSS is very sensitive to the local lumen geometry. For example, assuming Poiseuille flow in two circular tubes with a diameter of 1.5 mm and 1.6 mm under equal flow, the WSS is more than 20% higher in the only 7% smaller tube. Accurate assessment and validation of manual annotated or automatically segmented coronary lumen is therefore necessary to achieve accurate 3D lumen geometry for WSS simulations.

Lumen volumes per artery or segment as assessed by CT show good correlation with IVUS [Otsuka-08]. The assessment of clinical significant stenosis is possible with high accuracies, but stenosis quantification is still hard [Leber-05, Caussin-06]. Manual delineation of the lumen is challenging because the contrast intensity varies per patient and scan. In addition large calcifications in the wall hinder proper assessment of the lumen and at these locations the lumen size often not adequately assessed [Cademartiri-05]. Quantitative assessment of the local lumen area is thus still a challenge by CT.

Apart from the lumen geometry, flow and/or pressure measurements are neces-
sary to compute patient-specific WSS profiles. These hemodynamic input param-
eters for the CFD calculations cannot be provided by CT at this moment. Although
true WSS values cannot be derived, the differentiation of relative high and low WSS
has also proven to be valuable in atherosclerosis research [Wentzel-03, Gijsen-08]. In
Chapter 8, we propose to estimate the flow through the arteries based on the lu-
men diameters. From measured data the relationship was obtained between the
diameter of an artery and the flow, which can aid the WSS simulation when no flow
or pressure information is available.

9.2.3 ATHEROSCLEROSIS ASSESSMENT

One advantage of CT over conventional angiography is that it is a non-invasive imag-
ing modality, and in addition CT can not only image the coronary lumen, but also
the vessel wall. This opens the road for coronary plaque detection, characterization
and quantification. In general three plaque types are discriminated with CT; non-
calcified plaques, calcified plaques and mixed plaques. Several efforts have been
undertaken to subdivide the non-calcified plaques in plaques mainly consisting of
fibrous tissue (hyperdense) and plaques with lipid content (hypodense plaques)
based on CT intensity values. Good discrimination of these two types has turned out
to be hard since the intensity values of both types overlap [Schroeder-04, Leber-04] and
are also influenced by the contrast enhanced lumen [Cademartiri-05].

The detection of plaque is mainly dependent on the type of plaque type and its
size. Calcified plaques can be detected with high sensitivity, but half of the non-
calcified plaques is missed by CT [Achenbach-04, Leber-04]. These results were confirmed
in Chapter 4. In this chapter it is also shown that in particular the small non-calcified
plaques (<1 mm plaque thickness) are missed with CT. These small plaques have a
much higher prevalence than the larger plaques, which highly decreases the overall
sensitivity of CT to detect plaques. Nevertheless large plaques, which are clinical
important, can be detected with acceptable sensitivity. Since these plaques have
a higher prevalence in the proximal parts of the coronary tree, it is also generally
noticed that plaque detection is better in these parts [Mollet-05].

Ask one observer twice or two different observers to judge the same CT scan on
plaque presence and plaque classification and the results may differ considerably
(Chapter 4), depending on, amongst other things, the experience of the observ-
ers, the quality of the CT scan and the part of the coronary tree that is assessed.

When comparing to IVUS, non-calcified plaques are often not detected and calcified plaques are easily considered as mixed plaque. Mixed plaques with a small calcification can easily be classified as non-calcified plaques as small calcification cannot be detected by CT (Chapter 5).

Detecting plaques and differentiating between plaque types with CT is thus not an easy task. It is even harder to quantify the size of plaque by CT. Volumetric measurements tend to underestimate the plaque volume especially of non-calcified plaques whereas the volume of plaques with calcifications is overestimated [Achenbach-04, Otsuka-08, Schepis-09]. For risk stratification it is in the first place important that the volumetric plaque assessment is consistent among patients and within a patient over time. When this can be guaranteed and the plaque burden can be related to increased cardiovascular risk than it is not a problem when small plaques are not incorporated into this volumetric measure, since the measured volumetric plaque burden is than only a reflection of the true plaque burden.

9.2.4 FUTURE PERSPECTIVES

Coronary CT angiography will undoubtedly consolidate and extend its position in clinical practice. Progression in the clinical field will be preceded by technical advances in the CT scanner's hardware as well as in the reconstruction and post-processing software. New scanners aim at both higher temporal and spatial resolution. Dual-source CT scanners have halved the temporal resolution and the recent 320-detector row scanners allow to "snapshot" the heart within one rotation. Thanks to these improvements patients with high or irregular heart rates can now be imaged, which greatly increases the number of patients eligible for CT angiography. Upcoming are the flat-panel CT scanners, which can be thought of as a conventional multi-detector CT scanners in which the detector rows have been replaced by an area detector [Gupta-08]. Software developments aim to minimize imaging artifacts and to improve the image quality by incorporating new reconstruction algorithms and filters. In addition segmentation algorithms are developed and incorporated to facilitate the user by (semi)-automatically derivation of clinical relevant measures, which will increase the reproducibility of the results

At this moment qualitative assessment of WSS and atherosclerosis is possible (see Chapter 2) in human coronary arteries. However to obtain more quantitative values and measures for WSS and atherosclerosis with CT as stand-alone imaging modality, the technical advances mentioned above are undoubtedly necessary. Due to the

limited spatial resolution and the almost similar attenuation of the coronary wall and surrounding tissue, coronary CT as stand-alone imaging modality is not capable for this type of research. The inter,- and intra-observer variability's when assessing the diameter of the lumen or the size and components of the atherosclerotic wall are at this moment too large. For better atherosclerosis assessment contrast agents can be developed that target the plaque or a specific plaque component and increase in this way the plaque detection by CT. Until quantitative assessment of WSS and atherosclerosis is possible with CT as stand-alone imaging modality, the fusion technique of IVUS and CT as presented in Chapter 3 can be an intermediate solution.

9.3   FUSION OF IVUS AND CT

In Chapter 3 a technique is presented that determines the 3D position of the IVUS images in the 3D CT images. On the one hand this technique allows for validation of CT derived parameters by comparison to IVUS (Chapter 4 and 5) and on the other hand 3D IVUS contours can serve as the input for WSS simulations and atherosclerosis assessment (Chapter 6 and 7).

9.3.1   VALIDATION OF CT VERSUS IVUS

To validate CT derived lumen and/or wall segmentations, lumen and wall parameters have to be compared to the same parameters as derived with IVUS, the gold standard for coronary artery imaging. Whereas in clinical studies comparison of both imaging modalities is carried out on a segment base or at landmarks such as the minimum lumen diameter, the technique in Chapter 3 registers larger parts of the coronary artery as imaged by IVUS. This opens the possibility to validate CT derived information against IVUS in several ways.

In chapter 4 and 5 lumen and wall were not segmented in CT, but the presence of plaque, the presence of calcifications and the plaque type was determined. In chapter 4 it was shown that the accuracy to detect and classify calcified plaque by CT was much higher than for non-calcified plaque. In combination with geometrical information derived from IVUS, the detection of plaque (components) can be determined in relation to the size of the plaque(component) as is demonstrated in Chapter 4 for non-calcified plaque and in Chapter 5 for calcifications.

When CT lumen and wall contours are obtained either by manually annotation or semi-(automatically) segmentation they can be validated against the contours derived from IVUS images. Areas can be compared at a local scale, but also volumetric measures per segment, artery or tree, can be compared for example to validate plaque burden assessment. Also the influence of, for example, lumen contrast intensity and the presence of calcifications on the accuracy of the CT contours can be investigated. In addition derived parameters such as the percentage of area stenosis or the remodeling index can be validated over the complete extent of the registered part of the artery.

Aside from validation it is it is possible to position the IVUS contours over the CT dataset. Without assessing the contours in CT, the intensity of lumen and plaque can be determined. This information could serve as input for segmentation algorithms. Furthermore, projecting IVUS images next to CT cross-sectional images overlaid with IVUS contours can be a valuable tool to increase the CT reading skills of observers.

The presented technique to combine IVUS and CT information also has some drawbacks and limitations. Unfortunately only a limited number of patients and thus data is available for comparison since only patients included in research protocols will be imaged by both modalities because of the invasive nature of IVUS and the radiation dose of CT. For optimal validation ideally IVUS and CT should be obtained simultaneously, however this is not possible. If patients are imaged within a short time-span plaque characteristics and size will not change, however lumen dimensions can vary a lot due to, among others, stress and medication. The presented technique compares IVUS and CT on a very local scale. Since for clinical applications this might be too local, simpler techniques might be more appropriate for validation of volumetric parameters such as plaque burden.

9.3.2 SHEAR STRESS AND ATHEROSCLEROSIS

The initial goal of the reconstruction technique in Chapter 3 was to create 3D patients-specific coronary geometry suitable for WSS simulations by placing the IVUS derived lumen and wall contours onto the 3D CT-derived centerline. In Chapter 6 and 7, the 3D reconstructed arteries are successfully used in WSS simulations.

In Chapter 6 for the first time several 3D coronary artery geometries are created by combination of IVUS lumen and wall contours and coronary CT angiography. WSS was simulated in these geometries and related to the location of plaque ruptures as were identified on IVUS. The plaque ruptures were found most often upstream at the shoulders of the plaque and at higher WSS locations than on average over the plaque. This is in consensus with the hypothesis that high WSS by influencing the plaque components, destabilizes the plaque and what is previously reported [Groen-07, Fukumoto-08].

Previous reconstruction techniques positioned IVUS into 3D by placing the contours onto the 3D derived catheter path, which was imaged by bi-plane angiography (ANGUS). The advantage of the IVUS-CT combination is that it is not dependent on bi-plane acquisition, and no additional actions by the cardiologist during the intervention are required (i.e. diluted contrast injection and special angiography positions). Also the reconstruction technique is easier and faster. As mentioned before, a drawback of the technique is that, although CT is widely available, only few patients will be imaged by both CT and IVUS. On the other hand, the availability of data to perform the ANGUS technique is at least equally sparse. An advantage of the ANGUS technique is that both biplane angiography and IVUS are acquired at the same time, which is not possible for IVUS and CT. The ANGUS technique is also extensively validated and already widely applied by several research groups.

9.3.3 FUTURE PERSPECTIVES

As indicated above, many studies to validate CT more extensively are possible with this technique and some are currently in progress. The CT technology is still evolving and with every improvement, there is need for exploration of the capabilities of the new systems. As this moment no standardized method to validate CT is available. The proposed reconstruction technique might be a start to compare IVUS and CT for each new scanner in a similar way. Knowledge about the accuracy of CT is necessary to derive feasible relations between WSS and atherosclerosis. As the CT scanners become better, also more extensive and more quantitative relations can be obtained with CT as stand-alone imaging technique.

As shown in Chapter 7, the reconstruction technique is not limited to grey-scale IVUS alone. CT can serve as backbone for all invasive tomographic imaging techniques in which landmarks can be distinguished that are also visible in CT. This opens doors to study in-vivo plaque components in 3D as assessed with virtual histology, optical coherence tomography or NIR-IVUS in relation to WSS. On the other hand, also other 3D imaging techniques than CT can serve as backbone, such as MRI angiography and rotational angiography.

IVUS acquisition is often limited to one of the main coronary branches. The WSS cannot reliable be simulated near side-branches since the disturbed flow in the bifurcations regions will not be correctly simulated if the side branches are not incorporated into the geometry. The reconstruction technique can be extended by incorporating side-branches derived from the CT dataset into the 3D geometry derived from the IVUS contours. Of course the accuracy of the WSS will not be optimal in the side-branches since the geometry is obtained from CT instead of from IVUS, but by simulating flow through the branches, the WSS patterns near the side-branches in the main branch will improve. Since atherosclerosis is often located near the side-branches, incorporating side-branches to the geometry has additional value. However adding side-branches to the geometry comes with choosing appropriate boundary conditions for the CFD simulations, which by itself is not straightforward when hemodynamic measurements are not available (Chapter 8).

9.4   CLINICAL APPLICATION OF SHEAR STRESS: QUO VADIT?

WSS is a proven factor in the localization of atherosclerosis and might have role in the progression and destabilization of atherosclerosis [Slager-05]. WSS has been suggested as additional local risk-factor to the known systemic risk factors. Deviating WSS patterns in the coronary arteries might even indicate regions vulnerable for rupture, however these relations are not yet established in large patients groups. Reason for this is that WSS assessment comes at this moment with invasive imaging and complex reconstruction techniques that are not widely available. CT angiography could fill-in this gap as soon as the geometries of CT have proven to be good enough for coronary WSS assessment.

The current methods to assess WSS and atherosclerosis in the coronary arteries are not optimal to study WSS and atherosclerosis over time. Whether IVUS and/or CT is used to assess the geometry for WSS simulations, the invasiveness of IVUS and the radiation dose of CT limit imaging over time. The assessment of atherosclerosis is generally only possible at one time point, often just after the first manifestation of the atherosclerotic disease. The consequence of this limitation is that the influence of WSS on atherosclerosis cannot be assessed over time and is thus limited to observational studies. In chapter 6 for example it is demonstrated that the WSS is generally higher at the location of ruptures than on average over the complete plaque. However from this study cannot be concluded that high WSS is induces changes in the composition of the plaque.

For the same reasons that WSS is not obtained over time, WSS is not assessed in high-risk patients without symptoms. This limits the possibilities to study WSS as risk-predictor for coronary artery event. A lot can be learned from ongoing research in the carotid arteries on the relation between WSS and atherosclerosis. The carotid arteries can already be imaged non-invasively and databases are build with patient information, with imaging information of the carotid arteries at several time-points and with event information. By adding WSS computations to this information more can be learned about WSS as predictor for cerebral vascular events. These results might steer the research of WSS as risk parameter in the coronary arteries.

As soon as patients are diagnosed with coronary artery disease, they get medication such statins. These medicines have proven to be very effective. However they overshadow the natural influence of parameters such as WSS on the development of plaques. In addition the event rates in large patient studies are nowadays very low, such that it is hard to find additional risk-factors. Therefore, animal studies are inevitable to study these types of relations since WSS can artificially be adapted, relations can be obtained at different time points and plaque composition can extensively studied by histological analysis. The large disadvantage of animal studies is that the pathophysiology of atherosclerosis is not comparable in the full extent to that of humans and thus findings in animals cannot always translated to humans.

Before WSS can be a clinical parameter, it is also necessary to investigate how accurate WSS simulations have to be. WSS simulations can be carried out in a wide range of complexity, where models with increased complexity try to mimic the real physiology more and more. Models in these thesis could for example be extended by including the movement of the artery during contraction of the heart, adding

the movement of the wall due to the pressure waves and by using patients-specific blood viscosity. However, increasing complexity of the models comes along with an increasing number of input parameters for the simulation that have to be determined or estimated from the patient. Aside from the scientific value and the evolvement of mathematical modeling techniques, it is uncertain how much additional value they will have in studying patient specific WSS in relation to atherosclerosis. Absolute WSS values change over time, within minutes, during the day, but also during one's life. More interesting is to study the relative difference in WSS between those regions that are affected with atherosclerosis and those not. The complexity of the WSS simulations and the accuracy of the geometrical description of the artery should be investigated in that light instead of focusing on "true, absolute" WSS values. In addition to the complexity of the models it should also be investigated how accurate the geometry of the coronary artery should be derived for different type of studies. For example a less accurate WSS pattern might be necessary to study WSS for risk stratification in a large patient groups than to determine WSS in relation to local plaque components.

9.5   GENERAL CONCLUSION

Coronary CT angiography can have a promising role as a stand-alone imaging modality to study WSS versus atherosclerosis in the coronary arteries, since it is widely available and can acquire fast and non-invasively images of the lumen and wall of the main and side branches of the coronary arteries. However, at this moment CT cannot provide the information that is necessary to quantitatively determine WSS values and relate this to plaque parameters. Lumen and wall segmentation and classification are still challenging both in case of manual annotation by clinical observers as well as for (semi-) automated segmentation algorithms. CT in combination with IVUS can provide accurate 3D information about lumen and wall, which is suitable to relate for WSS and atherosclerosis in a quantitative way. Unfortunately this technique will be limited to research applications since patients will not be imaged by both IVUS and CT because of the invasiveness of the IVUS procedure and the radiation exposure during CT acquisition. Until further improvements in CT, especially in spatial resolution, coronary CT angiography can only be used to relate WSS and atherosclerosis in a qualitative way. The value of quantitative and qualitative WSS and plaque assessment for risk-prediction, treatment or prevention of coronary atherosclerosis should be part of future studies.

REFERENTIES

References

Aarnoudse, van't Veer, Pijls, ter Woorst, Vercauteren, Tonino, Geven, Rutten, van Hagen, de Bruyne and van de Vosse **(2007)**. "Direct volumetric blood flow measurement in coronary arteries by thermodilution." J Am Coll Cardiol 50(24): 2294-2304.

Achenbach, Ropers, Holle, Muschiol, Daniel and Moshage **(2000)**. "In-plane coronary arterial motion velocity: measurement with electron-beam CT." Radiology 216(2): 457-463.

Achenbach, Moselewski, Ropers, Ferencik, Hoffmann, MacNeill, Pohle, Baum, Anders, Jang, Daniel and Brady **(2004)**. "Detection of calcified and noncalcified coronary atherosclerotic plaque by contrast-enhanced, submillimeter multidetector spiral computed tomography: a segment-based comparison with intravascular ultrasound." Circulation 109(1): 14-17.

Achenbach, Ropers, Hoffmann, MacNeill, Baum, Pohle, Brady, Pomerantsev, Ludwig, Flachskampf, Wicky, Jang and Daniel **(2004)**. "Assessment of coronary remodeling in stenotic and nonstenotic coronary atherosclerotic lesions by multidetector spiral computed tomography." J Am Coll of Cardiol 43(5): 842-847.

Agatston, Janowitz, Hildner, Zusmer, Viamonte and Detrano **(1990)**. "Quantification of coronary artery calcium using ultrafast computed tomography." J Am Coll Cardiol 15(4): 827-832.

Antiga and Steinman **(2004)**. "Robust and objective decomposition and mapping of bifurcating vessels." IEEE Transactions on Medical Imaging 23(6): 704-713.

Asakura and Karino **(1990)**. "Flow patterns and spatial distribution of atherosclerotic lesions in human coronary arteries." Circ Res 66(4): 1045-1066.

Badak, Schoenhagen, Tsunoda, Magyar, Coughlin, Kapadia, Nissen and Tuzcu **(2003)**. "Characteristics of atherosclerotic plaque distribution in coronary artery bifurcations: an intravascular ultrasound analysis." Coron Artery Dis 14(4): 309-316.

Bastarrika, Lee, Huda, Ruzsics, Costello and Schoepf **(2009)**. "CT of coronary artery diease." Radiology 253(2): 317-338.

Becker, Knez, Ohnesorge, Schoepf and Reiser **(2000)**. "Imaging of noncalcified coronary plaques using helical CT with retrospective ECG gating." AJR Am J Roentgenol 175(2): 423-424.

Becker, Nikolaou, Muders, Babaryka, Crispin, Schoepf, Loehrs and Reiser **(2003)**. "Ex-vivo coronary atherosclerotic plaque characterization with multi-detector-row CT." Eur Radiol 13: 2094-2098.

Bhatia, Bhatia, Dhindsa and Dhindsa **(2003)**. "Imaging of the vulnerable plaque: new modalities." South Med J 96(11): 1142-1147.

Bhullar, Li, Miao, Zandi, Kim, Shyy and Chien **(1998)**. "Fluid shear stress activation of IkappaB kinase is integrin-dependent." J Biol Chem 273(46): 30544-30549.

Blackmon, Streck, Thilo, Bastarrika, Costello and Schoepf **(2009)**. "Reproducibility of automated noncalcified coronary artery plaque burden assessment at coronary CT angiography." J Thorac Imaging 24(2): 96-102.

Bloch, Carlsson, Arheden and Stahlberg **(2009)**. "Quantifying coronary sinus flow and global LV perfusion at 3T." BMC Med Imaging 9: 9.

Boskamp, Rinck, Link, Kummerlen, Stamm and Mildenberger **(2004)**. "New vessel analysis tool for morphometric quantification and visualization of vessels in CT and MR imaging data sets." Radiographics 24(1): 287-297.

Bourantas, Kourtis, Plissiti, Fotiadis, Katsouras, Papafaklis and Michalis **(2005)**. "A method for 3D reconstruction of coronary arteries using biplane angiography and intravascular ultrasound images." Comput Med Imaging Graph 29(8): 597-606.

Boutsianis, Dave, Frauenfelder, Poulikakos, Wildermuth, Turina, Ventikos and Zund **(2004)**. "Computational simulation of intracoronary flow based on real coronary geometry." Eur J Cardiothorac Surg 26(2): 248-256.

Bovendeerd, Borsje, Arts and van de Vosse **(2006)**. "Dependence of intramyocardial pressure and coronary flow on ventricular loading and contractility: a model study." Ann Biomed Eng 34(12): 1833-1845.

Burke, Farb, Malcom, Liang, Smialek and Virmani **(1997)**. "Coronary risk factors and plaque morphology in men with coronary disease who died suddenly." N Engl J Med 336(18): 1276-1282.

Burke, Kolodgie, Farb, Weber, Malcom, Smialek and Virmani **(2001)**. "Healed plaque ruptures and sudden coronary death: evidence that subclinical rupture has a role in plaque progression." Circulation 103(7): 934-940.

Cademartiri, Mollet, Runza, Bruining, Hamers, Somers, Knaapen, Verheye, Midiri, Krestin and de Feyter **(2005)**. "Influence of intracoronary attenuation on coronary plaque measurements using multislice computed tomography: Observations in an ex-vivo model of coronary computed tomography angiography." Eur Radiol 15: 1426-1431.

Caro, Fitz-Gerald and Schroter **(1971)**. "Atheroma and arterial wall shear. Observation, correlation and proposal of a shear dependent mass transfer mechanism for atherogenesis." Proc R Soc Lond B Biol Sci 177(46): 109-159.

Caussin, Larchez, Ghostine, Pesenti-Rossi, Daoud, Habis, Sigal-Cinqualbre, Perrier, Angel, Lancelin and Paul **(2006)**. "Comparison of coronary minimal lumen area quantification by sixty-four-slice computed tomography versus intravascular ultrasound for intermediate stenosis." Am J Cardiol 98(7): 871-876.

Chatzizisis, Coskun, Jonas, Edelman, Feldman and Stone **(2007)**. "Role of endothelial shear stress in the natural history of coronary atherosclerosis and vascular remodeling: molecular, cellular, and vascular behavior." J Am Coll Cardiol 49(25): 2379-2393.

Chatzizisis, Jonas, Coskun, Beigel, Stone, Maynard, Gerrity, Daley, Rogers, Edelman, Feldman and Stone **(2008)**. "Prediction of the localization of high-risk coronary atherosclerotic plaques on the basis of low endothelial shear stress: an intravascular ultrasound and histopathology natural history study." Circulation 117(8): 993-1002.

Cheng, Tempel, van Haperen, van der Baan, Grosveld, Daemen, Krams and de Crom **(2006)**. "Atherosclerotic lesion size and vulnerability are determined by patterns of fluid shear stress." Circulation 113(23): 2744-2753.

Clarijs, Pasterkamp, Schoneveld, van Leeuwen, Hillen and Borst **(1997)**. "Compensatory enlargement in coronary and femoral arteries is related to neither the extent of plaque-free vessel wall nor lesion eccentricity. A postmortem study." Arterioscler Thromb Vasc Biol 17(11): 2617-2621.

Cunningham and Gotlieb **(2005)**. "The role of shear stress in the pathogenesis of atherosclerosis." Lab Invest 85(1): 9-23.

Dammers, Stifft, Tordoir, Hameleers, Hoeks and Kitslaar **(2003)**. "Shear stress depends on vascular territory: comparison between common carotid and brachial artery." J Appl Physiol 94(2): 485-489.

Davies, Barbee, Lal, Robotewskyj and Griem **(1995)**. "Hemodynamics and atherogenesis. Endothelial surface dynamics in flow signal transduction." Ann N Y Acad Sci 748: 86-102;

de Feyter, Mollet, Nieman, Arampatzis, Cademartiri, Pattynama and Serruys **(2004)**. "Noninvasive visualisation of coronary atherosclerosis with multislice computed tomography." Cardiovasc Radiat Med 5(1): 49-56.

de Feyter (2008). "Multislice ct coronary angiography: A new gold-standard for the diagnosis of coronary artery disease?" Nat Clin Pract Cardiovasc Med 5(3): 132-3.

de Weert, Cretier, Groen, Homburg, Cakir, Wentzel, Dippel and van der Lugt **(2009)**. "Atherosclerotic plaque surface morphology in the carotid bifurcation assessed with multidetector computed tomography angiography." Stroke 40(4): 1334-1340.

de Winter, Hamers, Degertekin, Tanabe, Lemos, Serruys, Roelandt and Bruining **(2004)**. "Retrospective image-based gating of intracoronary ultrasound images for improved quantitative analysis: the intelligate method." Catheter Cardiovasc Interv 61(1): 84-94.

Dewey and Hamm **(2007)**. "Cost effectiveness of coronary angiography and calcium scoring using CT and stress MRI for diagnosis of coronary artery disease." Eur Radiol 17(5): 1301-1309.

Dewey, Teige, Laule and Hamm **(2007)**. "Influence of heart rate on diagnostic accuracy and image quality of 16-slice CT coronary angiography: comparison of multisegment and halfscan reconstruction approaches." Eur Radiol 17(11): 2829-2837.

Dirksen, van der Wal, van den Berg, van der Loos and Becker **(1998)**. "Distribution of inflammatory cells in atherosclerotic plaques relates to the direction of flow." Circulation 98(19): 2000-2003.

Doriot, Dorsaz, Dorsaz, De Benedetti, Chatelain and Delafontaine **(2000)**. "In-vivo measurements of wall shear stress in human coronary arteries." Coron Artery Dis 11(6): 495-502.

Ehara, Kobayashi, Yoshiyama, Shimada, Shimada, Fukuda, Nakamura, Yamashita, Yamagishi, Takeuchi, Naruko, Haze, Becker, Yoshikawa and Ueda **(2004)**. "Spotty calcification typifies the culprit plaque in patients with acute myocardial infarction: an intravascular ultrasound study." Circulation 110(22): 3424-3429.

Falk, Shah and Fuster **(1995)**. "Coronary plaque disruption." Circulation 92(3): 657-671.

Farmakis, Soulis, Giannoglou, Zioupos and Louridas **(2004)**. "Wall shear stress gradient topography in the normal left coronary arterial tree: possible implications for atherogenesis." Curr Med Res Opin 20(5): 587-596.

Ferencik, Nieman and Achenbach **(2006)**. " Noncalcified and calcified coronary plaque detection by contrast-enhanced multi-detector computed tomography: a study of interobserver agreement." J Am Coll Cardiol 47(1):207-209.

Feskens, J.W. and A.H.H. **(2006)**. Coronaire hartziekten samengevat. Volksgezondheid Toekomst Verkenning, Nationaal Kompas Volksgezondheid. Bilthoven, RIVM.

Finet, Gilard, Perrenot, Rioufol, Motreff, Gavit and Prost **(2008)**. "Fractal geometry of arterial coronary bifurcations: a quantitative coronary angiography and intravascular ultrasound analysis." EuroIntervention 3(4): 490-498.

Flohr, McCollough, Bruder, Petersilka, Gruber, Suss, Grasruck, Stierstorfer, Krauss, Raupach, Primak, Kuttner, Achenbach, Becker, Kopp and Ohnesorge **(2006)**. "First performance evaluation of a dual-source CT (DSCT) system." Eur Radiol 16(2): 256-268.

Frauenfelder, Boutsianis, Schertler, Husmann, Leschka, Poulikakos, Marincek and Alkadhi **(2007)**. "In-vivo flow simulation in coronary arteries based on computed tomography datasets: feasibility and initial results." Eur Radiol 17(5): 1291-1300.

Friedman, Brinkman, Qin and Seed **(1993)**. "Relation between coronary artery geometry and the distribution of early sudanophilic lesions." Atherosclerosis 98(2): 193-199.

Fujii, Kobayashi, Mintz, Takebayashi, Dangas, Moussa, Mehran, Lansky, Kreps, Collins, Colombo, Stone, Leon and Moses **(2003)**. "Intravascular ultrasound assessment of ulcerated ruptured plaques: a comparison of culprit and nonculprit lesions of patients with acute coronary syndromes and lesions in patients without acute coronary syndromes." Circulation 108(20): 2473-2478.

Fukumoto, Hiro, Fujii, Hashimoto, Fujimura, Yamada, Okamura and Matsuzaki **(2008)**. "Localized elevation of shear stress is related to coronary plaque rupture: a 3-dimensional intravascular ultrasound study with in-vivo color mapping of shear stress distribution." J Am Coll Cardiol 51(6): 645-650.

Furchgott and Zawadzki **(1980)**. "The obligatory role of endothelial cells in the relaxation of arterial smooth muscle by acetylcholine." Nature 288**(5789)**: 373-6.

Gardner, Tan, Hull, Lisauskas, Sum, Meese, Jiang, Madden, Caplan, Burke, Virmani, Goldstein and Muller **(2008)**. "Detection of lipid core coronary plaques in autopsy specimens with a novel catheter-based near-infrared spectroscopy system." JACC Cardiovasc Imaging 1(5): 638-648.

George, Arbab-Zadeh, Miller, Kitagawa, Chang, Bluemke, Becker, Yousuf, Texter, Lardo and Lima **(2009)**. "Adenosine stress 64- and 256-row detector computed tomography angiography and perfusion imaging: a pilot study evaluating the transmural extent of perfusion abnormalities to predict atherosclerosis causing myocardial ischemia." Circ Cardiovasc Imaging 2(3): 174-182.

Giddens, Zarins and Glagov **(1993)**. "The role of fluid mechanics in the localization and detection of atherosclerosis." J Biomech Eng 115(4B): 588-594.

Gijsen, Allanic, van de Vosse and Janssen **(1999)**. "The influence of the non-Newtonian properties of blood on the flow in large arteries: unsteady flow in a 90 degrees curved tube." J Biomech 32(7): 705-713.

Gijsen, Oortman, Wentzel, Schuurbiers, Tanabe, Degertekin, Ligthart, Thury, de Feyter, Serruys and Slager **(2003)**. "Usefulness of shear stress pattern in predicting neointima distribution in sirolimus-eluting stents in coronary arteries." Am J Cardiol 92(11): 1325-1328.

Gijsen, Wentzel, Thury, Lamers, Schuurbiers, Serruys and van der Steen **(2007)**. "A new imaging technique to study 3-D plaque and shear stress distribution in human coronary artery bifurcations in vivo." J Biomech 40(11): 2349-2357.

Gijsen, Wentzel, Thury, Mastik, Schaar, Schuurbiers, Slager, van der Giessen, de Feyter, van der Steen and Serruys **(2008)**. "Strain distribution over plaques in human coronary arteries relates to shear stress." Am J Physiol Heart Circ Physiol 295(4): H1608-1614.

Glagov, Weisenberg, Zarins, Stakunavicius and Kolettis **(1987)**. "Compensatory enlargement of human atherosclerotic coronary arteries." N Engl J Med 316(22): 1371-1375.

Greenland, Bonow, Brundage, Budoff, Eisenberg, Grundy, Lauer, Post, Raggi, Redberg, Rodgers, Shaw, Taylor, Weintraub, Harrington, Abrams, Anderson, Bates, Grines, Hlatky, Lichtenberg, Lindner, Pohost, Schofield, Shubrooks, Stein, Tracy, Vogel and Wesley **(2007)**. "ACCF/AHA 2007 clinical expert consensus document on coronary artery calcium scoring by computed tomography in global cardiovascular risk assessment and in evaluation of patients with chest pain: a report of the American College of Cardiology Foundation Clinical Expert Consensus Task Force (ACCF/AHA Writing Committee to Update the 2000 Expert Consensus Document on Electron Beam Computed Tomography)." Circulation 115(3): 402-426.

Groen, Gijsen, van der Lugt, Ferguson, Hatsukami, van der Steen, Yuan and Wentzel **(2007)**. "Plaque rupture in the carotid artery is localized at the high shear stress region: a case report." Stroke 38(8): 2379-2381.

Groen, Gijsen, van der Lugt, Ferguson, Hatsukami, Yuan, van der Steen and Wentzel **(2008)**. "High shear stress influences plaque vulnerability." Neth Heart J 16(7-8): 280-283.

Grøttum, Svindland and Walloe **(1983)**. "Localization of atherosclerotic lesions in the bifurcation of the main left coronary artery." Atherosclerosis 47(1): 55-62.

Guggenheim, Doriot, Dorsaz, Descouts and Rutishauser **(1991)**. "Spatial reconstruction of coronary arteries from angiographic images." Phys Med Biol 36(1): 99-110.

Gupta, Cheung, Bartling, Lisauskas, Grasruck, Leidecker, Schmidt, Flohr and Brady **(2008)**. "Flat-panel volume CT: fundamental principles, technology, and applications." Radiographics 28(7): 2009-2022.

Hagenaars, Gussenhoven, van der Linden and Bom **(2000)**. "Reproducibility of calcified lesion quantification: a longitudinal intravascular ultrasound study." Ultrasound Med Biol 26(7): 1075-1079.

He and Ku **(1996)**. "Pulsatile flow in the human left coronary artery bifurcation: average conditions." J Biomech Eng 118(1): 74-82.

Hoffmann, Moselewski, Nieman, Jang, Ferencik, Rahman, Cury, Abbara, Joneidi-Jafari, Achenbach and Brady **(2006)**. "Noninvasive assessment of plaque morphology and composition in culprit and stable lesions in acute coronary syndrome and stable lesions in stable angina by multidetector computed tomography." J Am Coll Cardiol 47(8): 1655-1662.

Hoffmann, Nagurney, Moselewski, Pena, Ferencik, Chae, Cury, Butler, Abbara, Brown, Manini, Nichols, Achenbach and Brady **(2006)**. "Coronary multidetector computed tomography in the assessment of patients with acute chest pain." Circulation 114(21): 2251-2260.

Hoffmann, Kwait, Handwerker, Chan, Lamuraglia and Brady **(2003)**. " Vascular calcification in ex vivo carotid specimens: precision and accuracy of measurements with multi-detector row CT." Radiology 229(2): 375-381.

Holzapfel, Sommer, Gasser and Regitnig **(2005)**. "Determination of layer-specific mechanical properties of human coronary arteries with nonatherosclerotic intimal thickening and related constitutive modeling." Am J Physiol Heart Circ Physiol 289(5): H2048-2058.

Huo and Kassab **(2007)**. "A hybrid one-dimensional/Womersley model of pulsatile blood flow in the entire coronary arterial tree." Am J Physiol Heart Circ Physiol 292(6): H2623-2633.

Husmann, Herzog, Gaemperli, Tatsugami, Burkhard, Valenta, Veit-Haibach, Wyss, Landmesser and Kaufmann **(2009)**. "Diagnostic accuracy of computed tomography coronary angiography and evaluation of stress-only single-photon emission computed tomography/computed tomography hybrid imaging: comparison of prospective electrocardiogram-triggering vs. retrospective gating." Eur Heart J 30(5): 600-607.

Iriart, Brunot, Coste, Montaudon, Dos-Santos, Leroux, Labeque, Jais and Laurent **(2007)**. "Early characterization of atherosclerotic coronary plaques with multidetector computed tomography in patients with acute coronary syndrome: a comparative study with intravascular ultrasound." Eur Radiol 17(10): 2581-2588.

Iwami, Fujii, Miura, Otani, Iida, Kawamura, Yoshitake, Kohno, Hisamatsu, Iwamoto and Matsuzaki (1998). "Importance of left anterior descending coronary artery curvature in determining cross-sectional plaque distribution assessed by intravascular ultrasound." Am J Cardiol 82(3): 381-384.

Jeremias, Huegel, Lee, Hassan, Wolf, Yeung, Yock and Fitzgerald (2000). "Spatial orientation of atherosclerotic plaque in non-branching coronary artery segments." Atherosclerosis 152(1): 209-215.

Joshi, Leask, Myers, Ojha, Butany and Ethier (2004). "Intimal thickness is not associated with wall shear stress patterns in the human right coronary artery." Arterioscler Thromb Vasc Biol 24(12): 2408-2413.

Kaimovitz, Lanir and Kassab (2005). "Large-scale 3-D geometric reconstruction of the porcine coronary arterial vasculature based on detailed anatomical data." Ann Biomed Eng 33(11): 1517-1535.

Kassab and Fung (1995). "The pattern of coronary arteriolar bifurcations and the uniform shear hypothesis." Ann Biomed Eng 23(1): 13-20.

Kirpalani, Park, Butany, Johnston and Ojha (1999). "Velocity and wall shear stress patterns in the human right coronary artery." J Biomech Eng 121(4): 370-375.

Knez, Becker, Becker, Leber, White, Reiser and Steinbeck (2002). "Determination of coronary calcium with multi-slice spiral computed tomography: a comparative study with electron-beam CT." Int J Cardiovasc Imaging 18(4): 295-303.

Kopp, Schroeder, Baumbach, Kuettner, Georg, Ohnesorge, Heuschmid, Kuzo and Claussen (2001). "Non-invasive characterization of coronary lesion morphology and composition by multislice CT: first results in comparison with intracoronary ultrasound." Eur Radiol 11: 1607-1611.

Kostamaa, Donovan, Kasaoka, Tobis and Fitzpatrick (1999). "Calcified plaque cross-sectional area in human arteries: correlation between intravascular ultrasound and undecalcified histology." Am Heart J 137(3): 482-488.

Krams, Wentzel, Oomen, Vinke, Schuurbiers, de Feyter, Serruys and Slager (1997). "Evaluation of endothelial shear stress and 3D geometry as factors determining the development of atherosclerosis and remodeling in human coronary arteries in vivo. Combining 3D reconstruction from angiography and IVUS (ANGUS) with computational fluid dynamics." Arterioscler Thromb Vasc Biol 17(10): 2061-2065.

Krams, Wentzel, Cespedes, Vinke, Carlier, van der Steen, Lancee and Slager (1999). "Effect of catheter placement on 3-D velocity profiles in curved tubes resembling the human coronary system." Ultrasound Med Biol 25(5): 803-810.

Krams, Cheng, Helderman, Verheye, van Damme, Mousavi Gourabi, Tempel, Segers, de Feyter, Pasterkamp, De Klein, de Crom, van der Steen and Serruys (2006). "Shear stress is associated with markers of plaque vulnerability and MMP-9 activity." EuroIntervention 2(2): 250-256.

Leber, Knez, Becker, Becker, Ziegler, Nikolaou, Rist, Reiser, Carl White, Steinbeck and Boekstegers (2003). "Accuracy of multidetector spiral computed tomography in identifying and differentiating the composition of coronary atherosclerotic plaques. A comparative study with intracoronary ultrasound." J Am Coll Cardiol 43(7): 1241-1247.

Leber, Knez, White, Becker, von Ziegler, Muehling, Becker, Reiser, Steinbeck and Boekstegers (2003). "Composition of coronary atherosclerotic plaques in patients with acute myocardial infarction and stable angina pectoris determined by contrast-enhanced multislice computed tomography." Am J Cardiol 91(6): 714-718.

Leber, Knez, Becker, Becker, von Ziegler, Nikolaou, Rist, Reiser, White, Steinbeck and Boekstegers (2004). "Accuracy of multidetector spiral computed tomography in identifying and differentiating the composition of coronary atherosclerotic plaques: a comparative study with intracoronary ultrasound." J Am Coll Cardiol 43(7): 1241-1247.

Leber, Knez, Becker, Becker, Reiser, Steinbeck and Boekstegers (2005). "Visualising noncalcified coronary plaques by CT." Int J Cardiovasc Imaging 21: 55-61.

Leber, Knez, Ziegler, Becker, Nikolaou, Paul, Wintersperger, Reiser, Becker, Steinbeck and Boekstegers (2005). "Quantification of obstructive and nonobstructive coronary lesions by 64-slice computed tomography - A comparative study with quantification coronary angiography and intravascular ultrasound." J Am Coll Cardiol 26(1): 147-154.

Leber, Johnson, Becker, von Ziegler, Tittus, Nikolaou, Reiser, Steinbeck, Becker and Knez (2007). "Diagnostic accuracy of dual-source multi-slice CT-coronary angiography in patients with an intermediate pretest likelihood for coronary artery disease." Eur Heart J 28(19): 2354-2360.

Lee, Loree, Cheng, Lieberman, Jaramillo and Schoen (1993). "Computational structural analysis based on intravascular ultrasound imaging before in vitro angioplasty: prediction of plaque fracture locations." J Am Coll Cardiol 21(3): 777-782.

Lefèvre, Louvard, Morice, Pierre Dumas, Loubeyre, Benslimane, Premchand, Guillard and Piéchaud **(2000)**. "Stenting of bifurcation lesions: Classification, treatments, and results." Catheter Cardiovasc Interv 49: 274-283.

Lesser, Flygenring, Knickelbine, Hara, Henry, Kalil, Pelak, Lindberg, Pelzel and Schwartz **(2007)**. "Clinical utility of coronary CT angiography: coronary stenosis detection and prognosis in ambulatory patients." Catheter Cardiovasc Interv 69(1): 64-72.

Libby **(2002)**. "Inflammation in atherosclerosis." Nature 420: 868-875.

Libby **(2002)**. "Atherosclerosis: the new view." Sci Am 286(5): 46-55.

Loree, Grodzinsky, Park, Gibson and Lee **(1994)**. "Static circumferential tangential modulus of human atherosclerotic tissue." J Biomech 27(2): 195-204.

Lovett and Rothwell **(2003)**. "Site of carotid plaque ulceration in relation to direction of blood flow: an angiographic and pathological study." Cerebrovasc Dis 16(4): 369-375.

Mackay and Mensah **(2004)**. "The atlas of heart disease and stroke." Geneva: World Health Organization.

Maehara, Mintz, Bui, Walter, Castagna, Canos, Pichard, Satler, Waksman, Suddath, Laird, Kent and Weissman **(2002)**. "Morphologic and angiographic features of coronary plaque rupture detected by intravascular ultrasound." J Am Coll Cardiol 40(5): 904-910.

Malek and Izumo **(1995)**. "Control of endothelial cell gene expression by flow." J Biomech 28(12): 1515-1528.

Malek, Alper and Izumo **(1999)**. "Hemodynamic shear stress and its role in atherosclerosis." JAMA 282(21): 2035-2042.

Marquering, Dijkstra, Besnehard, Duth, Schuijf, J.J. and Reiber **(2008)**. "Coronary CT angiography: IVUS image fusion for quantitative plaque and stenosis analyses. " Medical Imaging 2008: Visualization, Image-Guided Procedures, and Modeling, Proceedings of the SPIE.

Meijboom, Mollet, van Mieghem, Kluin, Weustink, Pugliese, Vourvouri, Cademartiri, Bogers, Krestin and de Feyter **(2006)**. "Pre-operative computed tomography coronary angiography to detect significant coronary artery disease in patients referred for cardiac valve surgery." J Am Coll Cardiol 48(8): 1658-1665.

Metz, Schaap, Van Walsum and Niessen **(2007)**. "Semi-automatic coronary artery centerline extraction in computed tomography angiography data.' IEEE International Symposium on Biomedical Imaging: Macro to Nano.

Min, Kang, Shaw, Devereux, Robinson, Lin, Legorreta and Gilmore **(2008)**. "Costs and clinical outcomes after coronary multidetector CT angiography in patients without known coronary artery disease: comparison to myocardial perfusion SPECT." Radiology 249(1): 62-70.

Min and Lin **(2008)**. "What makes a coronary CT angiogram nondiagnostic?" J Cardiovasc Comput Tomogr 2(6): 351-359.

Mintz, Nissen, Anderson, Bailey, Erbel, Fitzgerald, Pinto, Rosenfield, Siegel, Tuzcu and Yock **(2001)**. "American College of Cardiology Clinical Expert Consensus Document on Standards for Acquisition, Measurement and Reporting of Intravascular Ultrasound Studies (IVUS). A report of the American College of Cardiology Task Force on Clinical Expert Consensus Documents." J Am Coll Cardiol 37(5): 1478-1492.

Mittal, Zhou, Linares, Ung, Kaimovitz, Molloi and Kassab **(2005)**. "Analysis of blood flow in the entire coronary arterial tree." Am J Physiol Heart Circ Physiol 289(1): H439-446.

Mohan, Mohan, Valente and Sprague **(1999)**. "Regulation of low shear flow-induced HAEC VCAM-1 expression and monocyte adhesion." Am J Physiol 276(5 Pt 1): C1100-7.

Mollet, Cademartiri and de Feyter **(2005)**. "Non-invasive multislice CT coronary imaging." Heart 91(3): 401-407.

Mollet, Cademartiri, Nieman, Saia, Lemos, MD, Serruys, Krestin and de Feyter **(2005)**. "Noninvasive assessment of coronary plaque burden using multislice computed tomography." Am J Cardiol 95: 1165-1169.

Mollet, Cademartiri, van Mieghem, Runza, McFadden, Baks, Serruys, Krestin and de Feyter **(2005)**. "High-resolution spiral computed tomography coronary angiography in patients referred for diagnostic conventional coronary angiography." Circulation 112(15): 2318-2323.

Molloi and Wong **(2007)**. "Regional blood flow analysis and its relationship with arterial branch lengths and lumen volume in the coronary arterial tree." Phys Med Biol 52(5): 1495-1503.

Motomiya and Karino **(1984)**. "Flow patterns in the human carotid artery bifurcation." Stroke 15(1): 50-56.

Motoyama, Kondo, Anno, Sugiura, Ito, Mori, Ishii, Sato, Inoue, Sarai, Hishida and Narula **(2007)**. "Atherosclerotic plaque characterization by 0.5-mm-slice multislice computed tomographic imaging." Circ J 71(3): 363-366.

Motoyama, Kondo, Sarai, Sugiura, Harigaya, Sato, Inoue, Okumura, Ishii, Anno, Virmani, Ozaki, Hishida and Narula **(2007)**. "Multislice computed tomographic characteristics of coronary lesions in acute coronary syndromes." J Am Coll Cardiol 50(4): 319-326.

Mowatt, Cook, Hillis, Walker, Fraser, Jia and Waugh **(2008)**. "64-Slice computed tomography angiography in the diagnosis and assessment of coronary artery disease: systematic review and meta-analysis." Heart 94(11): 1386-1393.

Murase, Kume, Korenaga, Ando, Sawamura, Masaki and Kita **(1998)**. "Fluid shear stress transcriptionally induces lectin-like oxidized LDL receptor-1 in vascular endothelial cells." Circ Res 83(3): 328-333.

Murray (1926). "The physiological principle of minimum work: I. The vascular system and the cost of blood volume." Proc Natl Acad Sci U S A 12(3): 207-214.

Nair, Kuban, Tuzcu, Schoenhagen, Nissen and Vince **(2002)**. "Coronary plaque classification with intravascular ultrasound radiofrequency data analysis." Circulation 106(17): 2200-2206.

Nikolaou, Becker, Flohr, Huber, Scheidler, Fayad and Reiser **(2004)**. "Optimization of ex vivo CT- and MR- imaging of atherosclerotic vessel wall changes." Int J Cardiovasc Imaging 20(4): 327-334.

Nikolaou, Sanz, Poon, Wintersperger, Ohnesorge, Rius, Fayad, Reiser and Becker **(2005)**. "Assessment of myocardial perfusion and viability from routine contrast-enhanced 16-detector-row computed tomography of the heart: preliminary results." Eur Radiol 15(5): 864-871.

Olufsen (1999). "Structured tree outflow condition for blood flow in larger systemic arteries." Am J Physiol 276(1 Pt 2): H257-268.

Otsuka, Bruining, van Pelt, Mollet, Ligthart, Vourvouri, Hamers, de Jaegere, Wijns, van Domburg, Stone, Veldhof, Verheye, Dudek, Serruys, Krestin and de Feyter **(2008)**. "Quantification of coronary plaque by 64-slice computed tomography: a comparison with quantitative intracoronary ultrasound." Invest Radiol 43(5): 314-321.

Perktold, Nerem and Peter **(1991)**. "A numerical calculation of flow in a curved tube model of the left main coronary artery." J Biomech 24(3-4): 175-189.

Pivkin, Richardson, Laidlaw and Karniadakis **(2005)**. "Combined effects of pulsatile flow and dynamic curvature on wall shear stress in a coronary artery bifurcation model." J Biomech 38: 1283-1290.

Pohle, Achenbach, Macneill, Ropers, Ferencik, Moselewski, Hoffmann, Brady, Jang and Daniel **(2007)**. "Characterization of non-calcified coronary atherosclerotic plaque by multi-detector row CT: comparison to IVUS." Atherosclerosis 190(1): 174-180.

Poos (2008). "Waaraan overlijden mensen in Nederland?" Volksgezondheid Toekomst Verkenning, Nationaal Kompas Volksgezondheid. Bilthoven, RIVM.

Prosi, Perktold, Ding and Friedman **(2004)**. "Influence of curvature dynamics on pulsatile coronary artery flow in a realistic bifurcation model." J Biomech 37(11): 1767-1775.

Pugliese, Mollet, Runza, van Mieghem, Meijboom, Malagutti, Baks, Krestin, de Feyter and Cademartiri **(2006)**. "Diagnostic accuracy of non-invasive 64-slice CT coronary angiography in patients with stable angina pectoris." Eur Radiol 16(3): 575-582.

Pundziute, Schuijf, Jukema, Boersma, de Roos, van der Wall and Bax **(2007)**. "Prognostic value of multislice computed tomography coronary angiography in patients with known or suspected coronary artery disease." J Am Coll Cardiol 49(1): 62-70.

Ramaswamy, Vigmostad, Wahle, Lai, Olszewski, Braddy, Brennan, Rossen, Sonka and Chandran **(2004)**. "Fluid dynamic analysis in a human left anterior descending coronary artery with arterial motion." Ann Biomed Eng 32(12): 1628-1641.

Reimann, Rinck, Birinci-Aydogan, Scheuering, Burgstahler, Schroeder, Brodoefel, Tsiflikas, Herberts, Flohr, Claussen, Kopp and Heuschmid **(2007)**. "Dual-source computed tomography: advances of improved temporal resolution in coronary plaque imaging." Invest Radiol 42(3): 196-203.

Ropers, Ropers, Pflederer, Anders, Kuettner, Stilianakis, Komatsu, Kalender, Bautz, Daniel and Achenbach **(2007)**. "Influence of heart rate on the diagnostic accuracy of dual-source computed tomography coronary angiography." J Am Coll Cardiol 50(25): 2393-2398.

Ruzsics, Lee, Zwerner, Gebregziabher, Costello and Schoepf **(2008)**. "Dual-energy CT of the heart for diagnosing coronary artery stenosis and myocardial ischemia-initial experience." Eur Radiol 18(11): 2414-2424.

Rybicki, Otero, Steigner, Vorobiof, Nallamshetty, Mitsouras, Ersoy, Mather, Judy, Cai, Coyner, Schultz, Whitmore and Di Carli **(2008)**. "Initial evaluation of coronary images from 320-detector row computed tomography." Int J Cardiovasc Imaging 24(5): 535-546.

Rybicki, Melchionna, Mitsouras, Coskun, Whitmore, Steigner, Nallamshetty, Welt, Bernaschi, Borkin, Sircar, Kaxiras, Succi, Stone and Feldman **(2009)**. "Prediction of coronary artery plaque progression and potential rupture from 320-detector row prospectively ECG-gated single heart beat CT angiography: Lattice Boltzmann evaluation of endothelial shear stress." Int J Cardiovasc Imaging.

Saihara, Hamasaki, Okui, Biro, Ishida, Yoshikawa, Kataoka, Ninomiya, Mizoguchi, Ichiki, Otsuji and Tei **(2006)**. "Association of coronary shear stress with endothelial function and vascular remodeling in patients with normal or mildly diseased coronary arteries." Coron Artery Dis 17(5): 401-407.

Samijo, Willigers, Barkhuysen, Kitslaar, Reneman, Brands and Hoeks **(1998)**. "Wall shear stress in the human common carotid artery as function of age and gender." Cardiovasc Res 39(2): 515-522.

Sangiorgi, Rumberger, Severson, Edwards, Gregoire, Fitzpatrick and Schwartz **(1998)**. "Arterial calcification and not lumen stenosis is highly correlated with atherosclerotic plaque burden in humans: a histologic study of 723 coronary artery segments using nondecalcifying methodology." J Am Coll Cardiol 31(1): 126-133.

Sarwar, Rieber, Mooyaart, Seneviratne, Houser, Bamberg, Raffel, Gupta, Kalra, Pien, Lee, Brady and Hoffmann **(2008)**. "Calcified plaque: measurement of area at thin-section flat-panel CT and 64-section multidetector CT and comparison with histopathologic findings." Radiology 249(1): 301-306.

Schaap, Metz, Van Walsum, Van Der Giessen, Weustink, Mollet, Bauer, Bogunovic, Castro, Deng, Dikici, O'donnell, Frenay, Friman, Hernandez Hoyos, Kitslaar, Krissian, Kuhnel, Luengo-Oroz, Orkisz, Smedby, Styner, Szymczak, Tek, Wang, Warfield, Zambal, Zhang, Krestin and Niessen **(2009)**. "Standardized evaluation methodology and reference database for evaluating coronary artery centerline extraction algorithms." Med Image Anal 13(5): 701-14.

Schaar, Muller, Falk, Virmani, Fuster, Serruys, Colombo, Stefanadis, Ward Casscells, Moreno, Maseri and van der Steen **(2004)**. "Terminology for high-risk and vulnerable coronary artery plaques. Report of a meeting on the vulnerable plaque, June 17 and 18, 2003, Santorini, Greece." Eur Heart J 25(12): 1077-1082.

Schaar, de Korte, Mastik, van Damme, Krams, Serruys and van der Steen **(2005)**. "Three-dimensional palpography of human coronary arteries. Ex vivo validation and in-patient evaluation." Herz 30(2): 125-133.

Schepis, Marwan, Pflederer, Seltmann, Ropers, Daniel and Achenbach **(2009)**. "Quantification of noncalcified coronary atherosclerotic plaques with Dual Source Computed Tomography: comparison to intravascular ultrasound." Heart.

Schiemann, Bakhtiary, Hietschold, Koch, Esmaeili, Ackermann, Moritz, Vogl and Abolmaali **(2006)**. "MR-based coronary artery blood velocity measurements in patients without coronary artery disease." Eur Radiol 16(5): 1124-1130.

Schmermund, Baumgart, Gorge, Seibel, Gronemeyer, Ge, Haude, Rumberger and Erbel **(1997)**. "Coronary artery calcium in acute coronary syndromes: a comparative study of electron-beam computed tomography, coronary angiography, and intracoronary ultrasound in survivors of acute myocardial infarction and unstable angina." Circulation 96(5): 1461-1469.

Schoenhagen, Tuzcu, Stillman, Moliterno, Halliburton, Kuzmiak, Kasper, Magyar, Lieber, Nissen and White **(2003)**. "Non-invasive assessment of plaque morphology and remodeling in mildly stenotic coronary segments: comparison of 16-slice computed tomography and intravascular ultrasound." Coron Artery Dis 14(6): 459-462.

Schroeder, Kuettner, Leitritz, Janzen, Kopp, Herdeg, Heuschmid, Burgstahler, Baumbach, Wehrmann and Claussen **(2004)**. "Reliability of differentiating human coronary plaque morphology using contrast-enhanced multislice spiral computed tomography: a comparison with histology." J Comput Assist Tomogr 28(4): 449-454.

Scott, Arora, Farb, Virmani and Weissman **(2000)**. "Pathologic validation of a new method to quantify coronary calcific deposits in vivo using intravascular ultrasound." Am J Cardiol 85(1): 37-40.

Seo, Schachter and Barakat **(2005)**. "Computational study of fluid mechanical disturbance induced by endovascular stents." Ann Biomed Eng 33(4): 444-456.

Shaw, Berman, Hendel, Borges Neto, Min and Callister **(2008)**. "Prognosis by coronary computed tomographic angiography: matched comparison with myocardial perfusion single-photon emission computed tomography." J Cardiovasc Comput Tomogr 2(2): 93-101.

Sherman (1981). "On connecting large vessels to small. The meaning of Murray's law." J Gen Physiol 78(4): 431-453.

Shimada, Courtney, Nakamura, Hongo, Sonoda, Hassan, Yock, Honda and Fitzgerald **(2006)**. "Intravascular ultrasonic analysis of atherosclerotic vessel remodeling and plaque distribution of stenotic left anterior descending coronary arterial bifurcation lesions upstream and downstream of the side branch." Am J Cardiol 98(2): 193-196.

Sianos, Morel, Kappetein, Morice, Colombo, Dawkins, Brand, Dyck, Russel and Serruys **(2005)**. "The SYNTAX Score: an angiographic tool grading the complexity of coronary artery disease." EuroIntervention 2: 219-227.

Slager, Wentzel, Schuurbiers, Oomen, Kloet, Krams, von Birgelen, van der Giessen, Serruys and de Feyter **(2000)**. "True 3-dimensional reconstruction of coronary arteries in patients by fusion of angiography and IVUS (ANGUS) and its quantitative validation." Circulation 102(5): 511-516.

Slager, Wentzel, Gijsen, Schuurbiers, van der Wal, van der Steen and Serruys **(2005)**. "The role of shear stress in the generation of rupture-prone vulnerable plaques." Nat Clin Pract Cardiovasc Med 2(8): 401-407.

Slager, Wentzel, Gijsen, Thury, van der Wal, Schaar and Serruys **(2005)**. "The role of shear stress in the destabilization of vulnerable plaques and related therapeutic implications." Nat Clin Pract Cardiovasc Med 2(9): 456-464.

Soulis, Farmakis, Giannoglou and Louridas **(2006)**. "Wall shear stress in normal left coronary artery tree." J Biomech 39(4): 742-749.

Stary (1987). "Macrophages, macrophage foam cells, and eccentric intimal thickening in the coronary arteries of young children." Atherosclerosis 64: 91-108.

Stary, Blankenhorn, Chandler, Glagov, Insull, Richardson, Rosenfeld, Schaffer, Schwartz, Wagner and Wissler **(1992)**. "A definition of the intima of human arteries and of its atherosclerosis-prone regions. A report from the committe on vascular lesions of the council on arteriosclerosis, American Heart Association." Circulation 85: 391-405.

Stary, Chandler, Glagov, Guyton, Insull, Rosenfeld, Schaffer, Schwartz, Wagner and Wissler **(1994)**. "A definition of initial, fatty streak, and intermediate lesions of atherosclerosis. A report from the Committee on Vascular Lesions of the Council on Arteriosclerosis, American Heart Association." Circulation 89(5): 2462-2478.

Stary, Chandler, Dinsmore, Fuster, Glagov, Insull, Rosenfeld, Schwartz, Wagner and Wissler **(1995)**. "A definition of advanced types of atherosclerotic lesions and a histological classification of atherosclerosis. A report from the Committee on Vascular Lesions of the Council on Arteriosclerosis, American Heart Association." Circulation 92(5): 1355-1374.

Stary (2000). "Natural history and histological classification of atherosclerotic lesions: an update." Arterioscler Thromb Vasc Biol 20(5): 1177-1178.

Stillman, Oudkerk, Ackerman, Becker, Buszman, de Feyter, Hoffmann, Keadey, Marano, Lipton, Raff, Reddy, Rees, Rubin, Schoepf, Tarulli, van Beek, Wexler and White **(2007)**. "Use of multidetector computed tomography for the assessment of acute chest pain: a consensus statement of the North American Society of Cardiac Imaging and the European Society of Cardiac Radiology." Int J Cardiovasc Imaging 23(4): 415-427.

Stone, Coskun, Kinlay, Clark, Sonka, Wahle, Ilegbusi, Yeghiazarians, Popma, Orav, Kuntz and Feldman **(2003)**. "Effect of endothelial shear stress on the progression of coronary artery disease, vascular remodeling, and in-stent restenosis in humans: in vivo 6-month follow-up study." Circulation 108(4): 438-444.

Sun, Zhang, Lu, Yu, Yang, Zhou, Wang and Fan **(2008)**. "Identification and quantification of coronary atherosclerotic plaques: a comparison of 64-MDCT and intravascular ultrasound." AJR Am J Roentgenol 190(3): 748-754.

Suo, Oshinski and Giddens **(2008)**. "Blood flow patterns in the proximal human coronary arteries: relationship to atherosclerotic plaque occurrence." Mol Cell Biomech 5(1): 9-18.

Svindland (1983). "The localization of sudanophilic and fibrous plaques in the main left coronary bifurcation." Atherosclerosis 48(2): 139-145.

Tadjfar (2004). "Branch angle and flow into a symmetric bifurcation." J Biomech 126(4): 517-518.

Tang, Teng, Canton, Yang, Ferguson, Huang, Zheng, Woodard and Yuan **(2009)**. "Sites of rupture in human atherosclerotic carotid plaques are associated with high structural stresses: an in vivo MRI-based 3D fluid-structure interaction study." Stroke 40(10): 3258-3263.

Tommaso (2008). "One year perspective on COURAGE." Catheter Cardiovasc Interv 72(3): 426-429.

Tsutsui, Yamagishi, Uematsu, Suyama, Nakatani, Yasumura, Asanuma and Miyatake **(1998)**. "Intravascular ultrasound evaluation of plaque distribution at curved coronary segments." Am J Cardiol 81(8): 977-981.

Tuzcu, Kapadia, Tutar, Ziada, Hobbs, McCarthy, Young and Nissen **(2001)**. "High prevalence of coronary atherosclerosis in asymptomatic teenagers and young adults: evidence from intravascular ultrasound." Circulation 103(22): 2705-2710.

van der Giessen, Schaap, Gijsen, Groen, van Walsum, Mollet, Dijkstra, van de Vosse, Niessen, de Feyter, van der Steen and Wentzel **(2009)**. "3D fusion of intravascular ultrasound and coronary computed tomography for in-vivo wall shear stress analysis: a feasibility study." Int J Cardiovasc Imaging.

van der Steen, Cespedes, Carlier, Mastik, Lupotti, Borsboom, Li, Serruys and Bom **(2000)**. "Flow estimation using an intravascular imaging catheter." Ultrasonics 38(1-8): 363-368.

van Mieghem, McFadden, de Feyter, Bruining, Schaar, Mollet, Cademartiri, Goedhart, de Winter, Granillo, Valgimigli, Mastik, van der Steen, van der Giessen, Sianos, Backx, Morel, van Es, Zalewski and Serruys **(2006)**. "Noninvasive detection of subclinical coronary atherosclerosis coupled with assessment of changes in plaque characteristics using novel invasive imaging modalities: the Integrated Biomarker and Imaging Study (IBIS)." J Am Coll Cardiol 47(6): 1134-1142.

VanBavel and Spaan **(1992)**. "Branching patterns in the porcine coronary arterial tree. Estimation of flow heterogeneity." Circ Res 71(5): 1200-1212.

VanderLaan, Reardon and Getz **(2004)**. "Site specificity of atherosclerosis. Site-selective responses to atherosclerotic modulators." Arterioscler, Thromb Vasc Biol 24(1): 12-22.

Vattikuti and Towler **(2004)**. "Osteogenic regulation of vascular calcification: an early perspective." Am J Physiol Endocrinol Metab 286(5): E686-696.

Vengrenyuk, Carlier, Xanthos, Cardoso, Ganatos, Virmani, Einav, Gilchrist and Weinbaum **(2006)**. "A hypothesis for vulnerable plaque rupture due to stress-induced debonding around cellular microcalcifications in thin fibrous caps." Proc Natl Acad Sci U S A 103(40): 14678-14683.

Virmani, Kolodgie, Burke, Farb and Schwartz **(2000)**. "Lessons from sudden coronary death: a comprehensive morphological classification scheme for atherosclerotic lesions." Arterioscler Thromb Vasc Biol 20(5): 1262-1275.

Virmani, Burke, Kolodgie and Farb **(2002)**. "Vulnerable plaque: the pathology of unstable coronary lesions." J Interv Cardiol 15(6): 439-446.

Virmani, Kolodgie, Burke, Finn, Gold, Tulenko, Wrenn and Narula **(2005)**. "Atherosclerotic plaque progression and vulnerability to rupture: angiogenesis as a source of intraplaque hemorrhage." Arterioscler Thromb Vasc Biol 25(10): 2054-61.

Virmani, Burke, Farb and Kolodgie **(2006)**. "Pathology of the vulnerable plaque." J Am Coll Cardiol 47(8 Suppl): C13-18.

von Birgelen, Erbel, Di Mario, Li, Prati, Ge, Bruining, Gorge, Slager, Serruys and et al. **(1995)**. "Three-dimensional reconstruction of coronary arteries with intravascular ultrasound." Herz 20(4): 277-289.

Wahle, Lopez, Olszewski, Vigmostad, Chandran, Rossen and Sonka **(2006)**. "Plaque development, vessel curvature, and wall shear stress in coronary arteries assessed by X-ray angiography and intravascular ultrasound." Med Image Anal 10(4): 615-631.

Wellnhofer, Goubergrits, Kertzscher, Affeld and Fleck **(2009)**. "Novel non-dimensional approach to comparison of wall shear stress distributions in coronary arteries of different groups of patients." Atherosclerosis 202(2): 483-490.

Wentzel, Gijsen, Schuurbiers, Groen, van der Giessen, van der Steen and Serruys **(2001)**. "Why do we need flow measurements? Role of flow and shear stress in atherosclerotic disease. Handbook of Optical Coherence Tomography." Bouma and Tearney.

Wentzel, Krams, Schuurbiers, Oomen, Kloet, van der Giessen, Serruys and Slager **(2001)**. "Relationship between neointimal thickness and shear stress after Wallstent implantation in human coronary arteries." Circulation 103(13): 1740-1745.

Wentzel, Janssen, Vos, Schuurbiers, Krams, Serruys, de Feyter and Slager **(2003)**. "Extension of increased atherosclerotic wall thickness into high shear stress regions is associated with loss of compensatory remodeling." Circulation 108(1): 17-23.

Wentzel, Gijsen, Schuurbiers, Krams, Serruys, de Feyter and Slager **(2005)**. "Geometry guided data averaging enables the interpretation of shear stress related plaque development in human coronary arteries." J Biomech 38(7): 1551-1555.

WHO (2003). Global Health: today's challenges. The World Health Report 2002-Shaping the future. Geneva, World Health Organization.

Zarins, Giddens, Bharadvaj, Sottiurai, Mabon and Glagov **(1983)**. "Carotid bifurcation atherosclerosis. Quantitative correlation of plaque localization with flow velocity profiles and wall shear stress." Circ Res 53(4): 502-514.

Zeng, Boutsianis, Ammann, Boomsma, Wildermuth and Poulikakos **(2008)**. "A study on the compliance of a right coronary artery and its impact on wall shear stress." J Biomech Eng 130(4): 041014.

THANKS

Dankwoord

Dit is dan het eindstation van vier en half jaar werk. Hoewel de reis soms meer op een rit in de achtbaan leek, sta ik nu vol trots op het perron. Sommigen van jullie hebben de trein voorbij zien komen, anderen zijn in- en/of uitgestapt, en enkelen hebben plaatsgenomen in dezelfde coupé of zelfs in de stoel naast me om mijn reis te vergezellen. De trein is op zijn eindbestemming, tijd om uit te zwaaien en op de volgende trein te springen. Hopelijk kom ik jullie daar weer tegen.

Frank, Jolanda, ik wil jullie als eerste bedanken, natuurlijk voor de wetenschappelijke input en alle leermomenten, maar in het bijzonder omdat jullie lab de stabiele en rustige werkwagon was, waar de deur altijd openstond, waar er altijd iemand was met een luisterend oor, en waar niet gecontroleerd werd op treinkaartjes. Jullie hebben me op het promotiespoor gehouden. Jolanda, ik heb warme herinneringen aan de momenten buiten werk (Boston, Florida, Barcelona). Frank, je bent een rots in de branding, jouw optimisme en vertrouwen zijn in staat om tegenslagen te transformeren tot nieuwe uitdagingen.

Zonder promotoren geen promotiespoor. Het is lang onduidelijk geweest wie de rollen zouden gaan vervullen, dus ik wil jullie alle drie, Ton, Pim, Frans, in één adem bedanken voor de mogelijkheid die jullie hebben gecreëerd om aan het ErasmusMC te promoveren. Ton, je hebt mij vertrouwen gegeven in mijn werk en ik waardeer je interesse in mij als persoon. Juist omdat mijn werk verder weg staat van de klinische praktijk dan dat je gewend bent Pim, heb ik jouw klinische input altijd zeer op prijs gesteld. Frans, ik hoop dat ik in je vizier blijf en dat we de samenwerking kunnen onderhouden, de TU/e voelt nog steeds als een leerzame thuisbasis.

Ook de andere leden van promotie- en leescommissie wil ik op deze plaats bedanken. Wouter Jukema, Wim van der Giessen, bedankt dat jullie vanuit een

cardiologisch perspectief interesse in mijn werk hebben getoond. Udo, I feel honoured that you will join my thesis defense as an expert in the field of cardiac CT. In the first instance you had some doubts about my request to join your research group for only three months. Nevertheless, with the effort of all the other people working at your lab during my stay, in special Michael, Patrick, Fabian, and Pal, we were able to produce a nice piece of scientific work. I learned a lot, thank you for that. Wiro, de komst van de BIGR onder jouw leiding, met jullie kennis en ondersteuning, heeft mede de richting van dit proefschrift bepaald.

Ook alle collega's van het lab ben ik dank verschuldigd voor de fijne werksfeer, alle steun en gezellige activiteiten buiten het werk. Harald, ik had me geen fijnere mede-aio kunnen wensen. Ik krijg het nog warm bij de gedachte aan onze fietstocht in Florida. Nog even en dan ga ook jij je proefschrift verdedigen. Ik kijk er naar uit. Hans, ook jij weet het belang van lekker eten en een goed glas wijn. We toosten er nog één. Kim, ik mis nu al onze 10 minuten dames praat aan het begin van de ochtend. Ali, ik bewonder je lef om in Nederland te gaan promoveren. Heel veel succes met je onderzoek. Alle studenten die het lab hebben aangedaan, bedankt voor jullie inbreng op welke wijze ook. Naast het biomechanica lab, is er nog het groter geheel, de afdeling biomedische technologie. Collega's bedankt voor de goede sfeer, het jaarlijkse labuitje was telkens een feest. Mieke, bedankt voor je warme wijze waarop je ondersteuning geeft aan de afdeling.

Een multidisciplinair project doe je niet alleen. Veel mensen van verschillende afdelingen hebben dit proefschrift mogelijk gemaakt. Van de BIGR wil ik Theo, Michiel en Coert bedanken voor jullie inbreng en oplossingen als ik zelf op het wiskundig- en programmeervlak vastliep. Ik heb veel van jullie geleerd. Nico, Lisan, Kei, jullie representeren voor mij de cardiac CT poot binnen het ErasmusMC, zonder wie er geen data geweest zou zijn voor dit proefschrift. Bedankt voor jullie samenwerking. Een even belangrijk deel van de data is afkomstig van de interventiecardiologie. Het werken in een instituut met een hoog aangeschreven team aan interventiecardiologen en cathlabtechnici, heeft toegang gegeven tot uitzonderlijke data. Bedankt dat jullie dit wilden delen.

Het is soms lastig om naast de verdieping van je promotie, je ook te blijven ontwikkelen op persoonlijk vlak en je te verbreden binnen je vakgebied. Hoewel het regelmatig als spagaat voelde, heeft de opleiding Qualified Medical Engineer van de SMPE/e zeker bijgedragen aan mijn vorming. Herman, Ineke en alle anderen,

bedankt voor jullie ondersteuning, persoonlijk, inhoudelijk, organisatorisch en financieel.

Familie, vrienden, bedankt voor de steun de afgelopen jaren en het begrip wanneer ik te druk was met mijn proefschrift of even tijd voor mezelf nodig had. Niels, we hebben samen fijne jaren beleefd en lief en leed gedeeld. Bedankt voor je geduld, steun en de vele preken op ICT gebied. Ik ga er nog wat aan hebben in mijn nieuwe baan.

Studiegenootjes, squashmaatjes, vrienden, Inge, Lambert, Marcel, Homme-Auke, jullie begrijpen als geen ander de frusten van het biomedisch technologisch onderzoek. Dank jullie wel dat ik die met jullie mocht weg meppen tijdens het squashen, en mocht weg borrelen in de weekendjes. Inge, dankjewel voor je steun, met weinig woorden begrijpen wij elkaar. Bedankt dat je met mijn zus paranimf wilt zijn. Het wordt een mooi plaatje met drie vrouwen op een rij. Lambert, even zijn we collega's geweest en zelfs een moment stadsgenoten. Het schept een band die hopelijk nog lang blijft. Marcel, Homme-Auke, we zullen elkaar nog regelmatig tegenkomen op werkgebied, laten we niet vergeten zo nu en dan ook een avondje of weekendje te prikken.

Lieve meiden, jullie weten dat ik jullie bedoel, domweg bedankt dat jullie mijn vriendinnen zijn. Ik hoop dat we in de toekomst nog heel veel mooie momenten mogen delen. Het is met jullie altijd fijn, één op één, met of zonder partner of met zijn allen bij elkaar. En die boom op de omslag, tja… don't ask.

Lieve Martin, al jaren ken ik je als goede vriend, maar sinds een jaar is je rol in mijn leven drastisch veranderd. Samen maken we nu voorzichtig toekomstplannen, maar laten we eerst van het nu genieten.

Lieve zus, Jessica, straks sta je als paranimf naast me, maar ik weet dat je altijd naast me staat om me te steunen. Ik zal er ook altijd voor jou en Niels zijn, door dik en dun.

Lieve pap, mam, het afronden van je promotieonderzoek is een feest, toch is er een traan omdat jij, mam, niet in de zaal zal zitten. 'Doe maar normaal, dan doe je al gek genoeg', heb je me geleerd, toch weet ik dat mijn ouders beiden buiten hun schoenen lopen van trots. Zonder jullie onvoorwaardelijke steun in alle keuzes die ik door de jaren heen heb gemaakt en jullie onuitputtelijke liefde, was me dit niet gelukt. Pap, ik weet dat je voor twee zal genieten.

Curriculum vitae

Alina Gerarda van der Giessen was born in Tiel on November 29th 1980. In 1993 she started pre-university education at the Lingecollege in Tiel, The Netherlands, from which she graduated in 1999. In the same year she started her study on Biomedical Engineering at the Eindhoven University of Technology and obtained her Master's degree in Medical Engineering in 2005.

Her Master's project was carried out at the department of cardiothoracic surgery of the University Medical Center of Maastricht and involved studying the cardiac function during extracorporeal life support.

After her Master's project she went more downstream of the Maas and exchanged Maastricht for Rotterdam to start as a PhD student at the Biomedical Engineering department of the Thorax Center of the ErasmusMC, resulting in this thesis. During her PhD period she spent three and a half months at the department of Radiology of the Massachusetts General Hospital in Boston, MA, USA. In parallel to her PhD, she started a post-graduate training to obtain the European degree of Qualified Medical Engineering at the School of Medical Physics and Engineering Eindhoven.

From March 2010 Alina will be employed as a clinical physicist trainee at the Jeroen Bosch Hospital in 's-Hertogenbosch.

PUBLICATIES

Scientific output

JOURNAL PAPERS

AG van der Giessen, M Schaap, FJH Gijsen, HC Groen, T van Walsum, NR Mollet, J Dijkstra, FN van de Vosse, WJ Niessen, PJ de Feyter, AFW van der Steen, JJ Wentzel, "3D fusion of intravascular ultrasound and coronary computed tomography for in-vivo wall shear stress analysis- A feasability study", In press, International Journal of Cardiovascular Imaging

AG van der Giessen, MH Toepker, PM Donelly, F Bamberg, C Raffle, T Irlbeck, CL Schlett, H Lee, T van Walsum, P Maurovich Horvat, FJH Gijsen, JJ Wentzel, U Hoffmann, "Reproducibility, accuracy, and predictors of accuracy for the detection of coronary atherosclerotic plaque composition by dual-source computed tomography- An ex-vivo comparison to IVUS", In press, Investigative Radiology

AG van der Giessen, JJ Wentzel, WB Meijboom, NR Mollet, AFW van der Steen, FN van de Vosse, PJ de Feyter and FJH Gijsen, "Plaque and shear stress distribution in human coronary bifurcations: A multi-slice computed tomography study", EuroIntervention, 2009 Mar;4(5):654-61

AG van der Giessen, FJH Gijsen, JJ Wentzel, PM Jairam, T van Walsum, LAE Neefjes, NR Mollet, WJ Niessen, FN van de Vosse, PJ de Feyter, AFW van der Steen, "Small coronary calcifications are not detectable by 64-slice computed tomography", submitted

AG van der Giessen, JJ Wentzel, H Li, T van Walsum, NR Mollet, J Dijkstra, WJ Niessen, FN van de Vosse, PJ de Feyter, AFW van der Steen and FJH Gijsen, "Location of plaque rupture in human coronary arteries is related to shear stress", submitted

JJ Wentzel, AG van der Giessen, S Garg, C Schultz, F Mastik, FJH Gijsen, PW Serruys, AFW van der Steen, E Regar, "In-vivo 3D distribution of lipid-core plaque in human coronary artery as assessed by fusion of NIR-IVUS and MSCT", submitted

M Schaap, CT Metz, T van Walsum, AG van der Giessen, AC Weustink, NRA. Mollet, C Bauer, H Bogunović, C Castro, X Deng, E Dikici, T O'Donnell, M Frenay, O Friman, M Hernández Hoyos, PH Kitslaar, K Krissian, C Kühnel, MA Luengo-Oroz, M Orkisz, Ö Smedby, M Styner, A Szymczak, H Tek, C Wang, SK Warfield, S Zambal, Y Zhang, GP Krestin and W Niessen, "Standardized Evaluation Methodology and Reference Database for Evaluating Coronary Artery Centerline Extraction Algorithms", Medical Image Analysis, 2009

JJ Wentzel, HC Groen, AG van der Giessen, R van der Giessen, G Rodriguez -Granillo, FJH Gijsen, JCH Schuurbiers, AFW van der Steen, PJ de Feyter, "Plaque free wall determines positive remodeling at 3 year follow up: a serial IVUS study", submitted

HC Groen, L Simons, QJA van den Bouwhuijsen, EMH Bosboom, FJH Gijsen, AG van der Giessen, FN van de Vosse, AFW van der Streen, JCM Witteman, A van der Lugt JJ Wentzel, "MRI based quantification of outflow boundary conditions for computational fluid dynamics of stenosed human carotid arteries", accepted for Journal of Biomechanics

CONFERENCE PAPERS

AG van der Giessen, FJH Gijsen, JJ Wentzel, HC Groen, AFW van der Steen and FN van de Vosse, "Comparison of outflow condition models on the effect of wall shear stress distribution in patient specific coronary trees", Proceedings of the ASME 2008 Summer Bioengineering Conference (SBC2008), June 25-29, Marriott Resort, Marco Island, Florida, USA

M Schaap, L Neefjes, CT Metz, AG van der Giessen, AC Weustink, NRA. Mollet, JJ Wentzel, T van Walsum, WJ Niessen, "Coronary Lumen Segmentation using Graph Cuts and Robust Kernel Regression", Information Processing in Medical Imaging 2009 , 2009

M Schaap, CT Metz, T van Walsum, AG van der Giessen, AC Weustink, NRA. Mollet, GP Krestin, WJ Niessen, "On the evaluation of coronary artery centerline extraction algorithms - A standardized methodology and reference database", Invited paper. World Congress 2009 - Medical Physics and Biomedical Engineering, 2009

T van Walsum, M Schaap, CT Metz, AG van der Giessen, "Averaging centerlines: mean shift on paths", Medical Image Computing and Computer-Assisted Intervention - MICCAI 2008

CT Metz, M Schaap, AG van der Giessen, T van Walsum and WJ Niessen, "Semi-automatic coronary artery centerline extraction in computed tomography angiography data", Proceedings of IEEE International Symposium on Biomedical Imaging: Macro to Nano, 2007
Conference proceedings

CT Metz, M Schaap, T van Walsum, AG van der Giessen, AC Weustink, NRA. Mollet, GP Krestin and WJ Niessen, "Editorial: 3D Segmentation in the Clinic: A Grand Challenge II", - Coronary Artery Tracking, MICCAI 2008 workshop proceedings, 2008

CONFERENCE ABSTRACTS

AG van der Giessen, FJ Gijsen, JJ Wentzel, WB Meijboom, NR Mollet, FN van de Vosse and AF van der Steen and PJ de Feyter, "The influence of shear stress on plaque distribution in human coronary artery bifurcations assessed with multi-slice computed tomography", Circulation 2007,Volume 116, Issue 16 Supplement 1

AG van der Giessen, FJ Gijsen, JJ Wentzel, WB Meijboom, NR Mollet, FN van de Vosse, AF van der Steen and PJ de Feyter, "The influence of shear stress on plaque distribution in human coronary artery bifurcations assessed with multi-slice computed tomography", European Radiology 2007, Volume 17, Supplement 1, B029

AG van der Giessen, JJ Wentzel, CAM van Mieghem, N Mollet, AFW van de Steen, PJ de Feyter, FN van de Vosse and FJH Gijsen, "Non-invasive assessment of flow-related geometrical risk factors for atherosclerosis in human coronary bifurcations by MSCTA", Journal of Biomechanics 2006, Volume 39, Supplement 1, page S298

BOOK CHAPTERS

JJ Wentzel, FJH Gijsen, JCH Schuurbiers, HC Groen, AG van der Giessen and PW Serruys, "Why do we need flow measurements? - Role of flow and shear stress in atherosclerotic disease", Handbook of Optical Coherence Tomography in Cardiovascular Research, Eds E. Regar, T.G. van Leeuwen and P.W. Serruys, Informa Healthcare, 2007, ISBN: 978-1-84184-611-8

JJ Wentzel, FJH Gijsen, R Krams, R de Crom, C Cheng, HC Groen, AG van der Giessen, AFW van der Steen and PW Serruys, "Vulnerable plaque and shear stress", Handbook of the Vulnerable Plaque (2nd ed], Eds. R. Waksman, P.W. Serruys and J. Schaar, Informa Healthcare, 2007, ISBN: 978-1-841-84-621-7

Portfolio

COURSES

	Year	ECTS
Safety and risk analysis (TU/e, SMPE/e)	2009	6.0
Biostatistics (TU/e, CeMas)	2008	6.0
Cardiovascular fluid mechanics (TU/e)	2007	3.0
Knowledge based image segmentation (ASCI)	2007	1.5
Science philosophy (Coeur)	2007	1.5
Project management (TU/e, SMPE/e, Company Coaching)	2007	2.0
Atherosclerosis research (Coeur)	2006	1.5
Molecular biology in cardiovascular research (Coeur)	2006	1.5
Cardiovascular imaging and diagnostics (Coeur)	2005	1.5
Computational fluid dynamics 2 (J.M.Burgerscentrum)	2006	1.5
Scientific english (ErasmusMC)	2006	4.0
Vascular biology (NHS, Papendal course)	2006	2.0

SYMPOSIA

	Year	ECTS
5th Symposium on Biomechanics in Vascular Biology and Cardiovascular Disease (Rotterdam)	2010	0.6
Dutch Atherosclerosis Society Days (Ede)	2010	0.6
European Society of Cardiology Congress (Barcelona)	2009	1.5
Dutch Conference of Biomedical Engineering (Egmond aan Zee)	2009	0.6
4th Symposium on Biomechanics in Vascular Biology and Cardiovascular Disease (Rotterdam)	2009	0.6
Post-doc retreat of the PCDI (Heeze)	2009	0.9
ASME 2008 Summer BioEngineering Conference (Marco Island, FL)	2008	1.5
3rd Symposium on Biomechanics in Vascular Biology and Cardiovascular Disease (Rotterdam)	2008	0.6
American Heart Association Scietific Sessions (Orlando, FL)	2007	1.5
European Society of Radiology Congress (Vienna)	2006	1.2
Dutch Conference of Biomedical Engineering (Egmond aan Zee)	2006	0.6
2nd Symposium on Biomechanics in Cardiovascular disease: Shear stress in vascular biology (Rotterdam)	2006	0.6
World Congress of Biomechanics (Munich)	2006	0.6
Dutch Atherosclerosis Society Days (Ermelo)	2006	0.9

SUPERVISING

	Year	ECTS
Supervising internschip medical student from ErasmusMC (6 months)	2007	2.0
Supervising graduation project BSc student from InHolland (6 months)	2007	2.0
Supervising internschip BSc student from TU/e (4 months)	2006	1.5
Supervision practical assignments BSc students at TU/e (20 days)	2006	1.0
Study advice presentations for MSc student at TU/e (2 times)	2005	0.5

PODIUM PRESENTATIONS

Symposium of the Dutch Atherosclerosis Society (Ede)	2010
Dutch Conference of Bio-Medical Engineering (Egmond aan Zee)	2009
Algemeen Klinische Fysica nascholingsdag ('s-Hertogenbosch)	2009
ASME 2008 Summer Bioengineering Conference (Marco Island, Florida)	2008
American Heart Association Scientific Sessions (Orlando, Florida)	2007
European Congress of Radiology (Vienna)	2007
Dutch Conference of Bio-Medical Engineering (Egmond aan Zee)	2007
World Congress of Biomechanics (Munich)	2006

POSTER PRESENTATIONS

5th International Symposium on Biomechanics in Vascular Biology and Cardiovascular Disease (Rotterdam)	2010
European Congress of Cardiology (Barcelona)	2009
Dutch Conference of Bio-Medical Engineering (Egmond aan Zee)	2009
3rd International Symposium on Biomechanics in Vascular Biology and Cardiovascular Disease (Rotterdam)	2008
2nd Symposium in Biomechanics in Cardiovascular Disease: Shear Stress in Vascular Biology (Rotterdam)	2007
Dutch Atherosclerosis Society (Ermelo)	2006